Table of contents   **Page**

1. General experimental procedures

General Procedures. All synthetic manipulations were carried out under air unless noted otherwise. All alcoholamines and solvents were purchased from commercial sources and used as received. The ligand H_4(dobpdc) was purchased from Hangzhou Trylead Chemical Technology Co. The frameworks M_2(dobpdc) (M = Mg, Mn, Co, Ni, Zn), Mg_2(dotpdc), and Mg_2(pc-dobpdc) were prepared according to modified literature procedures. Powder X-ray diffraction patterns and 77 K N_2 adsorption isotherms for these materials were consistent with those from the literature. ^{1}H NMR spectra for digestion experiments were collected on either a Bruker AMX 300 MHz or Bruker AVQ 400 MHz NMR spectrometer and referenced to residual DMSO (δ 2.50 ppm). Attenuated total reflectance (ATR) infrared (IR) spectra were collected on a PerkinElmer Spectrum 400 Fourier transform (FT) IR spectrometer. Differential scanning calorimetry (DSC) measurements were carried out using a TA Instruments Q200 differential scanning calorimeter. Laboratory powder X-ray diffraction patterns were collected using a Bruker AXS D8 Advance diffractometer using Cu Kα radiation (λ = 1.5418 Å).

Thermogravimetric Analysis (TGA) and Differential Scanning Calorimetry Measurements. Dry TGA experiments were conducted using a TA Instruments TGA Q5000. Humid TGA experiments were conducted using a TA Instruments TGA Q50. The incident gas stream was humidified by passing it through two water bubblers in series, leading to an estimated water content of 1.3% at 25 °C (as determined by comparison to water isotherms). Isobars were measured using a ramp rate of 2 °C/min. Samples were activated at temperatures as described below under flowing N_2 for 20–30 min (until the mass stabilized) prior to switching the gas stream to pure CO_2. Masses are uncorrected for buoyancy effects. Decomposition experiments were carried out under dry N_2 using a temperature ramp rate of 1.5 °C/min. Differential scanning calorimetry measurements were taken similarly, wherein the sample was activated under flowing He for 20–30 min (until the mass stabilized) prior to switching the gas stream to pure CO_2 and cooling to −70 °C, while measuring the heat flow from the sample.

Gas Adsorption Measurements. Surface area measurements were conducted at 77 K under flowing N_2. Adsorption isotherms for O_2, H_2, CH_4, and CO_2 were obtained by volumetric methods using a Micromeritics 3Flex gas adsorption analyzer. All gases were 99.998% pure or higher. Isotherms collected at 30, 35, 50 or 75 °C were measured using a temperature controlled, well-stirred oil bath. Samples were regenerated at either 95 or 110 °C, depending on the N_2 activation temperature, under dynamic vacuum for 2–4 h between isotherms until the offgasing pressure reached <10 μbar. Isotherm data points were considered equilibrated after <0.01% pressure change occurred over a 30 s interval.

High Pressure Gas Adsorption Measurements. Measurements were conducted from 0–50 bar using a HPVA-II-100 from Particulate Systems, a subsidiary of Micromeritics. In a N_2-filled glovebox, a tared, stainless steel sample holder was loaded with 0.24 g of activated e-2-OH–Mg_2(dobpdc). After weighing the sample, the holder was sealed with VCR fittings and an airtight valve and connected to the analysis port of the instrument via an OCR fitting. The sample holder was placed inside an aluminum dewar connected to a Julabo FP89-HL circulator filled with Syltherm XLT fluid (temperature stability: ±0.02 °C) and evacuated for 2 h prior to measurement. Methods for determination of the sample freespace were described previously.[22] The NIST REFPROP[23] database was used to perform non-ideality corrections at each measured temperature and pressure. Prior to measurement, an empty sample holder was used to collect background CO_2 adsorption isotherms at the analysis temperatures and target pressure points. A small negative background was observed at

high pressures and can likely be attributed to volume or temperature calibration errors or errors in the equation of state used to correct for non-ideality. The background adsorption was found to be consistent over several measurements, and polynomial fits of replicate data sets at the analysis temperatures were used to perform background subtraction on the experimental data sets.

Synthesis of Alcoholamine-Appended and Alkoxyalkylamine-Appended M_2(dobpdc) (M = Mg, Ni), Mg_2(dotpdc), and Mg_2(pc-dobpdc) Compounds. A 20 mL scintillation vial was charged with 8 mL of either toluene, tetrahydrofuran, or chloroform, depending on the solubility with the alcoholamine, and 2 mL of the alcoholamine (for solids at room temperature, the alcoholamine was melted prior to addition). Methanol-solvated M_2(dobpdc) (~20 mg, M = Mg, Co, Ni), Mg_2(dotpdc), or Mg_2(pc-dobpdc) was filtered and washed with successive aliquots of solvent (2 × 10 mL). [**Note:** M_2(dobpdc) should not be allowed to dry completely as this can in some cases lead to decomposition of the framework.] Next, M_2(dobpdc) was added to the alcoholamine solution, and the vial was swirled several times and allowed to stand at room temperature for 24 h. The mixture was then filtered, and the resulting powder was thoroughly washed with solvent (2 × 20 mL) and allowed to dry for 2 min, yielding ~30 mg of the alcoholamine-appended framework. ^{1}H NMR digestion experiments indicated relative loadings. Activation of the samples for 20−30 min under flowing N_2 was sufficient to remove the excess solvent and alcoholamine from the pores to provide activated frameworks.

A modified procedure was used to prepare samples of alcoholamine-appended M_2(dobpdc) (M = Mn and Zn) (see Section 2) for the alcoholamines that exhibited step-shaped adsorption. A 25 mL Schlenk flask equipped with a stir bar was brought into an N_2-filled glovebox, filled with molecular sieves, brought out and placed under vacuum. Approximately 6 mL of alcoholamine was then added via syringe to the Schlenk flask, kept under flowing N_2, and allowed to dry under molecular sieves for 24-48 h. 25 mL of dry toluene or tetrahydrofuran, depending on the alcoholamine, was then added via syringe into the vial under flowing N_2, and the mixture was allowed to stir for an additional 30 minutes. Additionally, a 20 mL scintillation vial equipped with a Teflon screw thread closure cap was charged with the activated framework material, kept in an N_2-filled glovebox. PTFE Thread was taped to the top of the vial before placing the cap, and electrical tape was then placed over the cap to ensure an air-tight seal. The vial was removed from the glovebox and the dried alcoholamine solution was added via syringe. The vial was then left to stand in an N_2-filled glovebag for 24–48 h. [Note: for alcoholamines that were melted prior to use, the dry solvent was first added to the molecular sieves. The melted alcoholamine was then added, and the mixture was allowed to stand for 24–48 h.] The mixture was then filtered in a N_2-filled glovebag equipped with a vacuum hose, and the resulting powder was thoroughly washed with dry solvent (20 mL) and allowed to dry for 2 min, yielding ~30 mg of the alcoholamine-appended metal–organic framework. Activation of the samples for 20−30 min under flowing N_2 was sufficient to remove excess solvent and alcoholamine from the pores. These frameworks were kept under an active N_2 environment when not in use to minimize any possible degradation of the host framework. Analogous procedures were followed for the synthesis of the alkoxyalkylamine-appended metal–organic frameworks.

2. Large-scale preparation of M_2(dobpdc), Mg_2(pc-dobpdc), and Mg_2(dotpdc)

These procedures are adapted from the literature.[1,2]

Mg₂(dobpdc). An Erlenmeyer flask was charged with Mg(NO$_3$)$_2$·6H$_2$O (11.5 g, 45.0 mmol, 1.24 eq.), 4,4′-dihydroxy-[1,1′-biphenyl]-3,3′-dicarboxylic acid (9.90 g, 36.0 mmol, 1.00 eq.), *N,N*-dimethylformamide (DMF, 90 mL), and methanol (110 mL). The mixture was sonicated until the solids dissolved and then filtered through filter paper into a 350 mL screw-cap high pressure reaction vessel equipped with a stir bar. The mixture was sparged with N$_2$ for 1 h. The reaction vessel was sealed, and the reaction mixture was allowed to stir slowly at 120 °C for 14 h, resulting in precipitation of a white solid. The mixture was filtered, and the solid was quickly transferred to a Pyrex jar filled with DMF (500 mL). The jar was placed in an oven heated to 60 °C and allowed to stand for at least 3 h. At this time, the mixture was filtered and the solid was returned to the jar with fresh DMF (500 mL) and placed in an oven heated to 60 °C. This washing process was repeated a total of three times. The DMF was replaced with methanol (500 mL), and the washing process was repeated a further three times with methanol. A small portion of the solid was removed for activation, and placed in a vial under flowing N$_2$ at 180 °C for 24 h, transferred to a glass adsorption tube equipped with a Micromeritics *TransSeal*, and activated for an additional 24 h under reduced pressure (<10 μbar) at 180 °C. Activated Mg$_2$(dobpdc) (9.20 g) was obtained as a white solid. Langmuir surface area: 3896 m^2/g.

Mn₂(dobpdc). An Erlenmeyer flask was charged with MnCl$_2$·4H$_2$O (990 mg, 5.0 mmol, 2.5 eq.), 4,4′-dihydroxy-[1,1′-biphenyl]-3,3′-dicarboxylic acid (548 mg, 2.00 mmol, 1.00 eq.), DMF (100 mL), and ethanol (100 mL). The same synthesis and activation procedures were followed as above. Activated Mn$_2$(dobpdc) (0.56 g) was obtained as an off-white solid. Langmuir surface area: 3408 m^2/g. **Methanol-solvated Mn₂(dobpdc) slowly degrades and turns brown in the presence of air, and should be stored activated in a N₂-filled glovebox when not in use.**

Co₂(dobpdc). An Erlenmeyer flask was charged with Co(NO$_3$)$_2$·6H$_2$O (1.09 g, 3.75 mmol, 2.50 eq.), 4,4′-dihydroxy-[1,1′-biphenyl]-3,3′-dicarboxylic acid (411 mg, 1.50 mmol, 1.00 eq.), deionized (DI) water (50 mL), DMF (50 mL), and ethanol (50 mL). The mixture was sonicated until all of the solids dissolved and filtered through filter paper into a 350 mL screw-cap high pressure reaction vessel equipped with a stir bar. Afterwards, the same synthesis and activation procedures were followed as above for Mg$_2$(dobpdc). Activated Co$_2$(dobpdc) (0.56 g) was obtained as a pink solid. Langmuir surface area: 3665 m^2/g. **Methanol-solvated Co₂(dobpdc) slowly degrades and turns brown in the presence of air, and should be stored activated in a N₂-filled glovebox when not in use.**

Ni₂(dobpdc). An Erlenmeyer flask was charged with Ni(NO$_3$)$_2$·6H$_2$O (1.09 g, 3.75 mmol, 2.50 eq.), 4,4′-dihydroxy-[1,1′-biphenyl]-3,3′-dicarboxylic acid (411 mg, 1.50 mmol, 1.00 eq.), DI water (50 mL), DMF (50 mL), and ethanol (50 mL). The same synthesis and activation procedures were followed as for Mg$_2$(dobpdc). Activated Ni$_2$(dobpdc) (0.78 g) was obtained as a brown solid. Langmuir surface area: 3439 m^2/g.

Zn₂(dobpdc An Erlenmeyer flask was charged with Zn(NO$_3$)$_2$•6H$_2$O (3.72 g, 12.5 mmol, 2.50 eq.), 4,4′-dihydroxy-[1,1′-biphenyl]-3,3′-dicarboxylic acid (1.37 g, 5.00 mmol, 1.00 eq.), DMF (250 mL), and methanol (250 mL). The same synthesis and activation procedures were followed as above for Mg$_2$(dobpdc). Activated Zn$_2$(dobpdc) (1.89 g) was obtained as an off-white solid. Langmuir surface area: 3129 m^2/g. **Methanol-solvated Zn₂(dobpdc) slowly degrades in the presence of air (with no apparent change in color or powder X-ray diffraction pattern) and should be stored, activated, in a N₂-filled glovebox when not in use.**

Mg₂(pc-dobpdc) (Mg-IRMOF-74-II). The ligand 3,3′-dihydroxy-[1,1′-biphenyl]-4,4′-dicarboxylic acid was prepared according to the literature procedure.[16] A 20 mL scintillation vial was charged with 3,3′-dihydroxy-[1,1′-biphenyl]-4,4′-dicarboxylic acid (26.0 mg, 95.0 μmol, 1.00 eq.) and Mg(NO₃)₂·6H₂O (80.0 mg, 0.310 mmol, 3.10 eq.). Fresh DMF (7.5 mL) was added, and the solution was sonicated until the solids dissolved. Ethanol (0.5 mL) and DI water (0.5 mL) were then added. The vial was sealed with Teflon tape and heated at 120 °C in a heating block for 24 h, during which time an off-white solid precipitated from solution. The solution was filtered while still hot, and the solid was washed with fresh DMF (15 mL). The solid was transferred to a vial and soaked in fresh DMF (10 mL) at 60 °C for 3 h. The supernatant was decanted and replaced with fresh DMF (10 mL), and the vial was reheated to 60 °C. This washing process was repeated a total of three times. The DMF was replaced with methanol (10 mL), and the off-white solid was soaked in methanol at 60 °C for 3 h. The supernatant was decanted and replaced with fresh methanol (10 mL), and the vial was reheated to 60 °C. This washing process was repeated a total of three times. Activation of the resulting powder at 180 °C under flowing N₂ for 14 h and then under reduced pressure at 180 °C for 24 h afforded Mg₂(pc-dobpdc) as a pale yellow powder. Large scale batches were prepared by combining the products from multiple 20 mL scintillation vials prior to washing. Langmuir surface area: 2506 m^2/g.

Mg₂(dotpdc). A 20 mL scintillation vial was charged H₄(dotpdc) (35.0 mg, 0.100 mmol, 1.00 eq., see Section 3). Mg(NO₃)₂·6H₂O (64.0 mg, 0.250 mmol, 2.50 eq.). Methanol (5.5 mL) and fresh DMF (4.5 mL) were added, and the solution was sonicated until the solids dissolved. The vial was sealed with Teflon tape and heated at 120 °C in a dry bath for 14 h, during which time a white solid precipitated from solution. The solid was washed using the procedure for Mg₂(pc-dobpdc). Heating of the resulting powder at 250 °C under flowing N₂ for 14 h, followed by heating under reduced pressure at 250 °C for 14 h, afforded activated Mg₂(dotpdc) as a fine, pale yellow powder. Langmuir surface area: 5771 m^2/g.
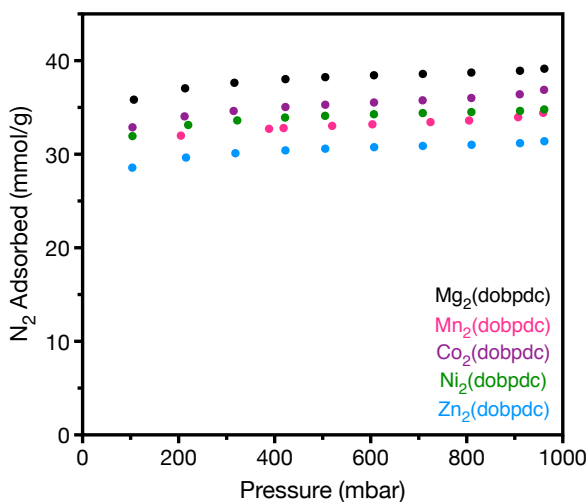
Figure S1. 77 K N₂ adsorption isotherms for activated Mg₂(dobpdc), Mn₂(dobpdc), Co₂(dobpdc), Ni₂(dobpdc), and Zn₂(dobpdc). The Langmuir surface areas calculated from these isotherms are indicated in the experimental procedures above.
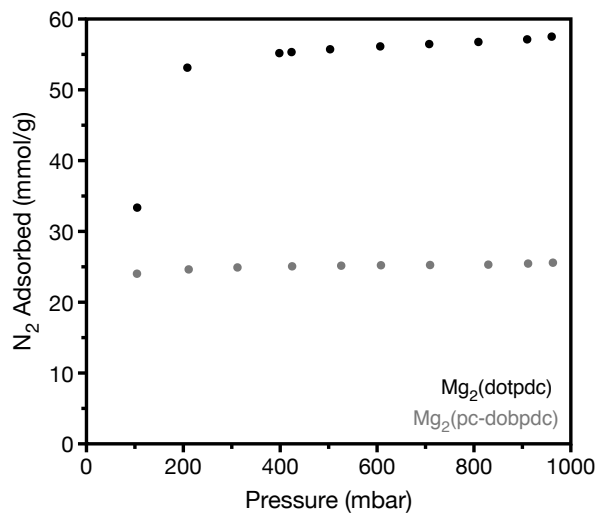
Figure S2. 77 K N_2 adsorption isotherms of activated Mg_2(dotpdc) and Mg_2(pc-dobpdc).

3. Characterization and surface area measurements for M_2(dobpdc) (M = Mg, Mn, Co, Ni, Zn), Mg_2(pc-dobpdc), and Mg_2(dotpdc)
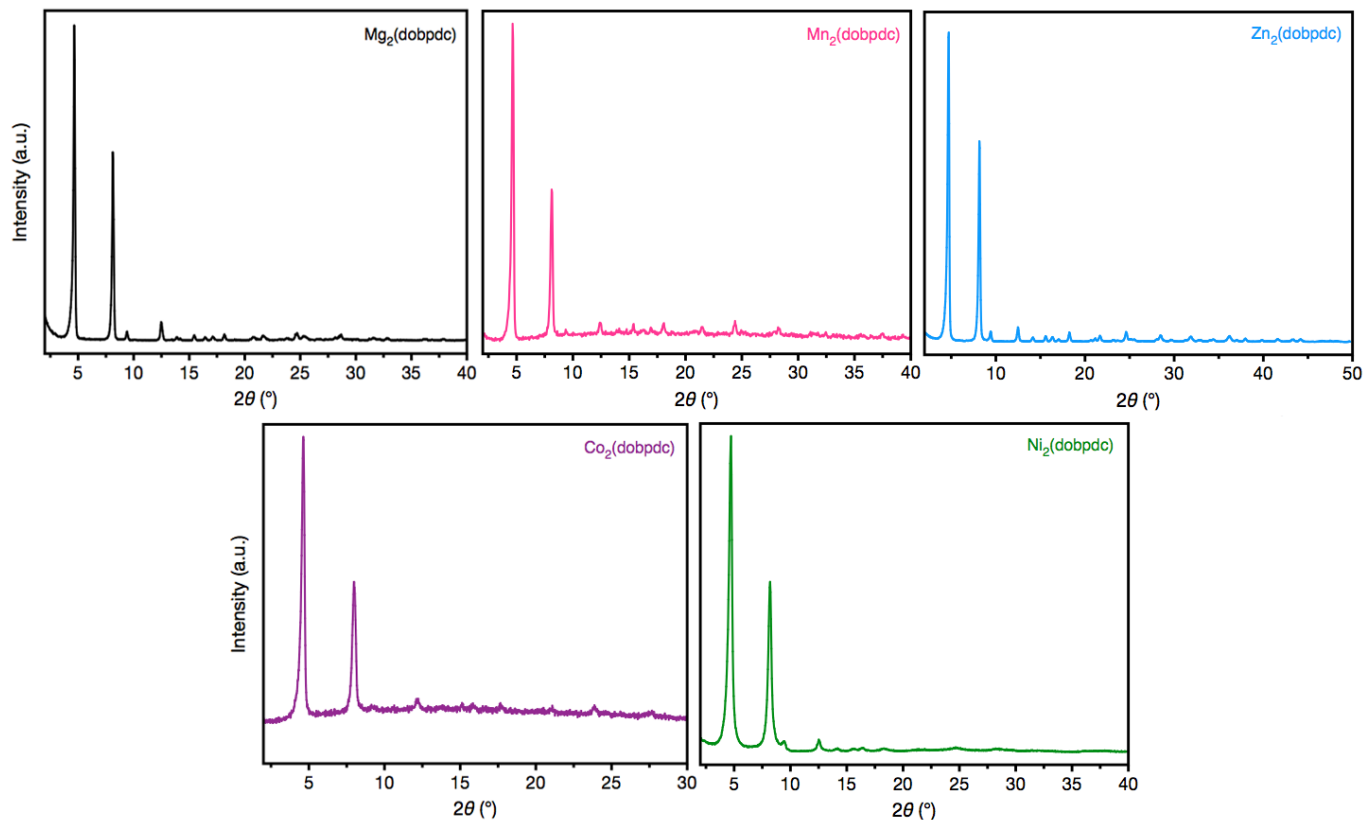

Figure S3. Powder X-ray diffraction patterns (CuKα radiation, λ = 1.5418 Å) of methanol-solvated Mg_2(dobpdc) (top left), Mn_2(dobpdc) (top middle), Zn_2(dobpdc) (top right), Co_2(dobpdc) (bottom left), and Ni_2(dobpdc) (bottom right).
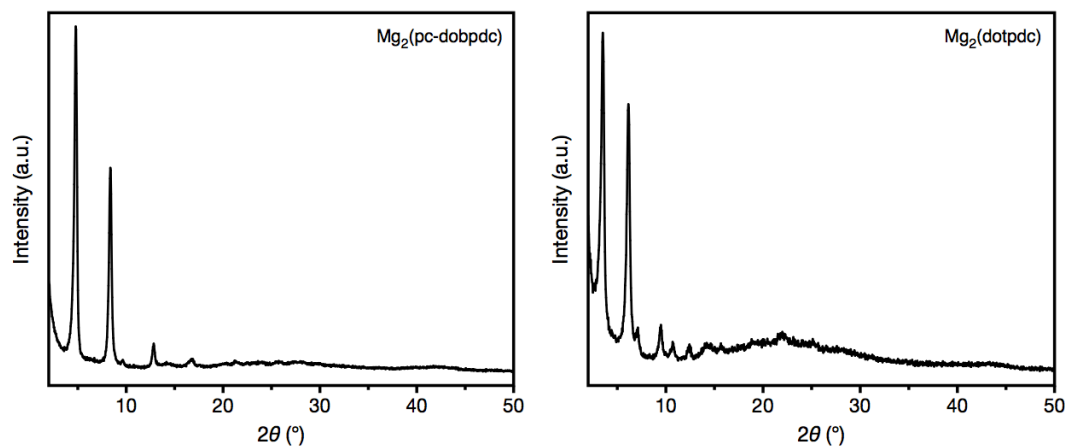
Figure S4. Powder X-ray diffraction patterns (CuKα radiation, λ = 1.5418 Å) of methanol-solvated Mg₂(pc-dobpdc) (left) and Mg₂(dotpdc) (right).

4. Synthesis of H₄(dotpdc) (4,4″-dioxido-[1,1′:4′,1″- terphenyl]-3,3″-dicarboxylic acid)

The H₄(dotpdc) ligand was synthesized using a new procedure to reduce the number of steps.
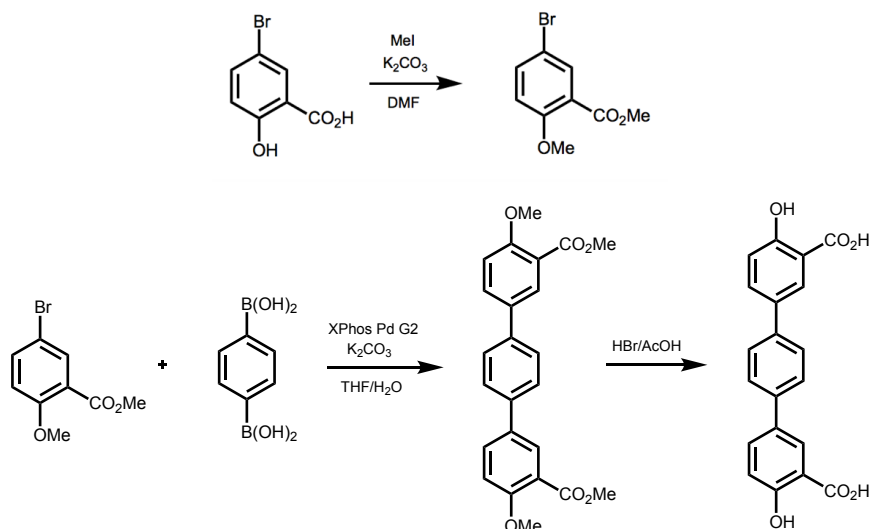
Figure S5. Reaction scheme for H₄(dotpdc) synthesis.

Methyl 5-bromo-2-methoxybenzoate[16] (4.00 g, 16.3 mmol, 49.8 eq.), benzene-1,4-diboronic acid (1.35 g, 8.15 mmol, 24.9 eq.), potassium carbonate (9.01 g, 65.2 mmol, 99.7 eq.), and XPhos Palladium G2 catalyst (0.26 g, 0.30 mmol, 1.0 eq.) were added to a round bottom Schlenk flask equipped with a stir bar and reflux condenser. The flask was cycled with vacuum and N_2 three times. Degassed THF (16 mL) and water (32 mL) were added, and the reaction was allowed to react under reflux at 100 °C for 24 hours. The reaction mixture was allowed to cool to room temperature, and the reaction mixture was poured into cold water (75 mL). The non-homogenous solution was filtered, and the precipitate was washed thoroughly with

cold water (3 × 10 mL). The resulting gray solid was dissolved in hot CH_2Cl_2 (100 mL) and the solution was filtered through celite, eluted with CH_2Cl_2 (300 mL), and concentrated in vacuo to yield a brown solid. The solid was triturated with cold methanol (20 mL), filtered, and washed with cold methanol (2 × 5 mL), yielding methyl 4,4″-dimethoxy-[1,1′:4′,1″-terphenyl]-3,3″-dicarboxylate (1.47 g, 44.4% yield) as an off-white solid. The ^{1}H NMR spectrum of this compound was identical to that previously reported.[3] Methyl 4,4″-dimethoxy-[1,1′:4′,1″-terphenyl]-3,3″-dicarboxylate was deprotected according to the literature procedure3 to yield H_4(dotpdc) (1.16 g, 91.0% yield) as a white solid.

5. Powder x-Ray diffraction patterns of alcoholamine- and alkoxyalkylamine-appended frameworks
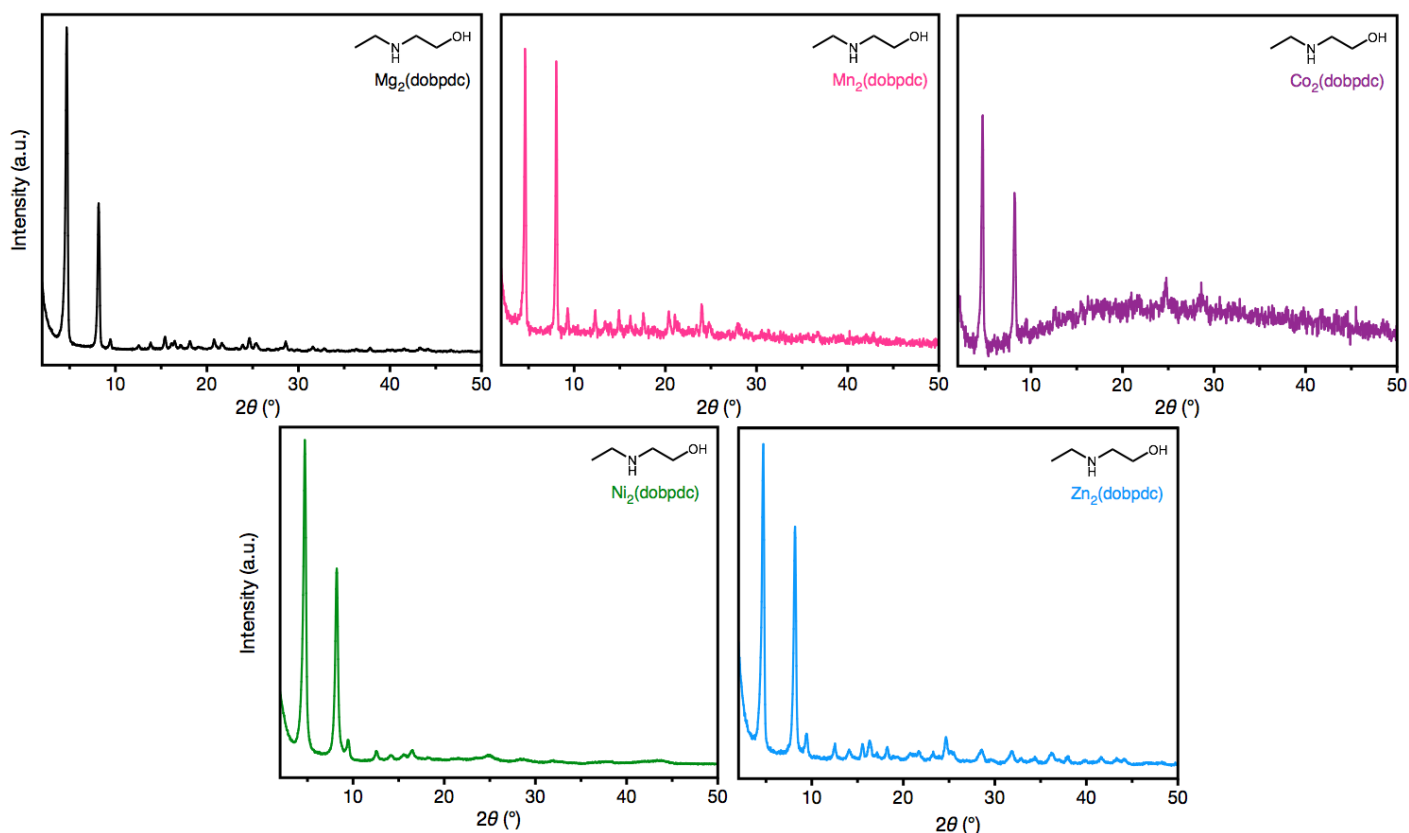
Figure S6. Powder X-ray diffraction pattern (CuKα radiation, λ = 1.5418 Å) of as-synthesized e-2-OH–Mg₂(dobpdc) (top left), e-2-OH–Mn₂(dobpdc) (top middle), e-2-OH–Co₂(dobpdc) (top right), e-2-OH–Ni₂(dobpdc) (bottom left), and e-2-OH–Zn₂(dobpdc) (bottom right).
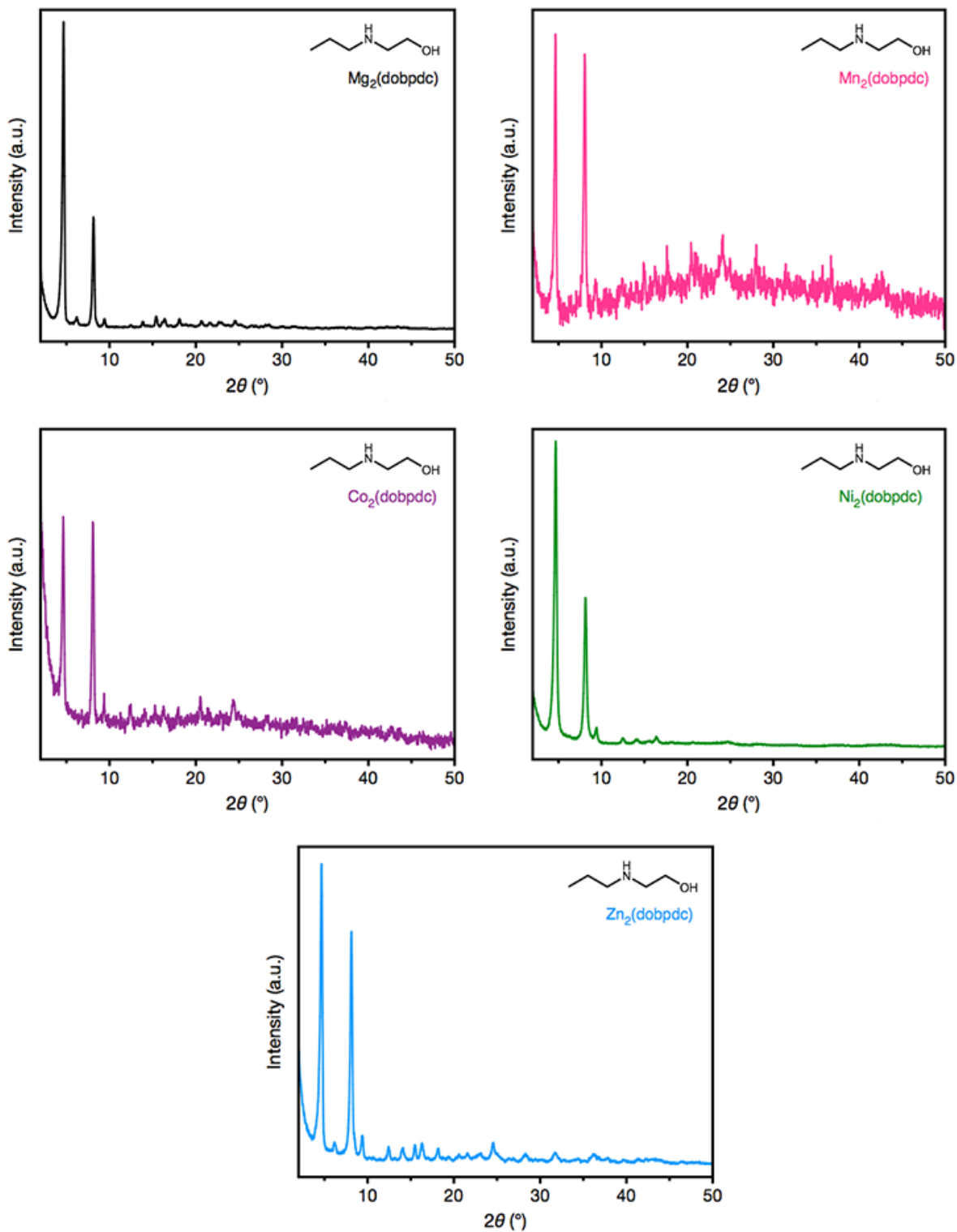
Figure S7. Powder X-ray diffraction pattern (CuKα radiation, λ = 1.5418 Å) of as-synthesized nPr-2-OH–Mg_2(dobpdc) (top left), nPr-2-OH–Mn_2(dobpdc) (top right), nPr-2-OH–Co_2(dobpdc) (middle left), nPr-2-OH–Ni_2(dobpdc) (middle right), and nPr-2-OH–Zn_2(dobpdc) (bottom).
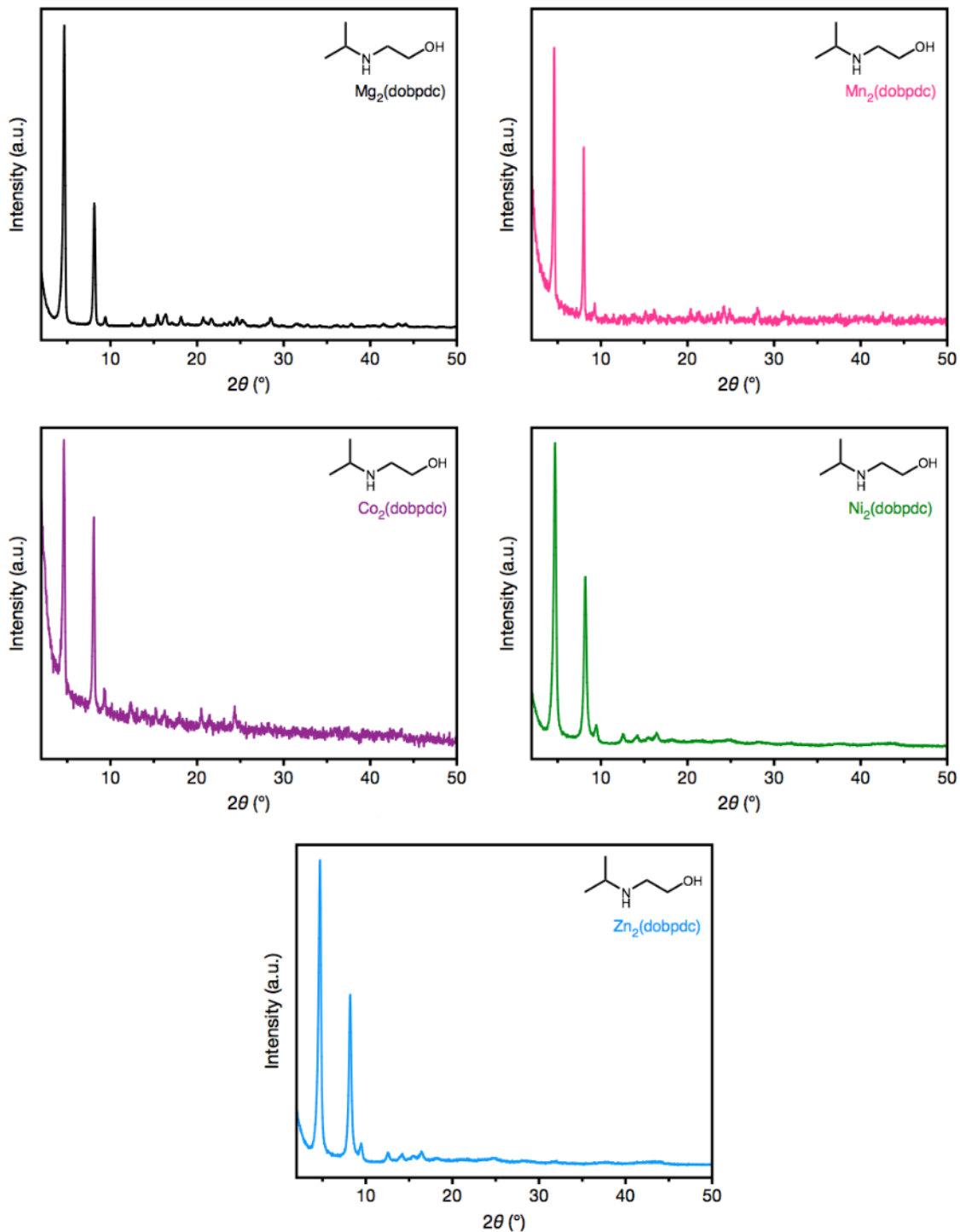
Figure S8. Powder X-ray diffraction pattern (CuKα radiation, λ = 1.5418 Å) of as-synthesized iPr-2-OH–Mg$_2$(dobpdc) (top left), iPr-2-OH–Mn$_2$(dobpdc) (top right), iPr-2-OH–Co$_2$(dobpdc) (middle left), iPr-2-OH–Ni$_2$(dobpdc) (middle right), and iPr-2-OH–Zn$_2$(dobpdc) (bottom).
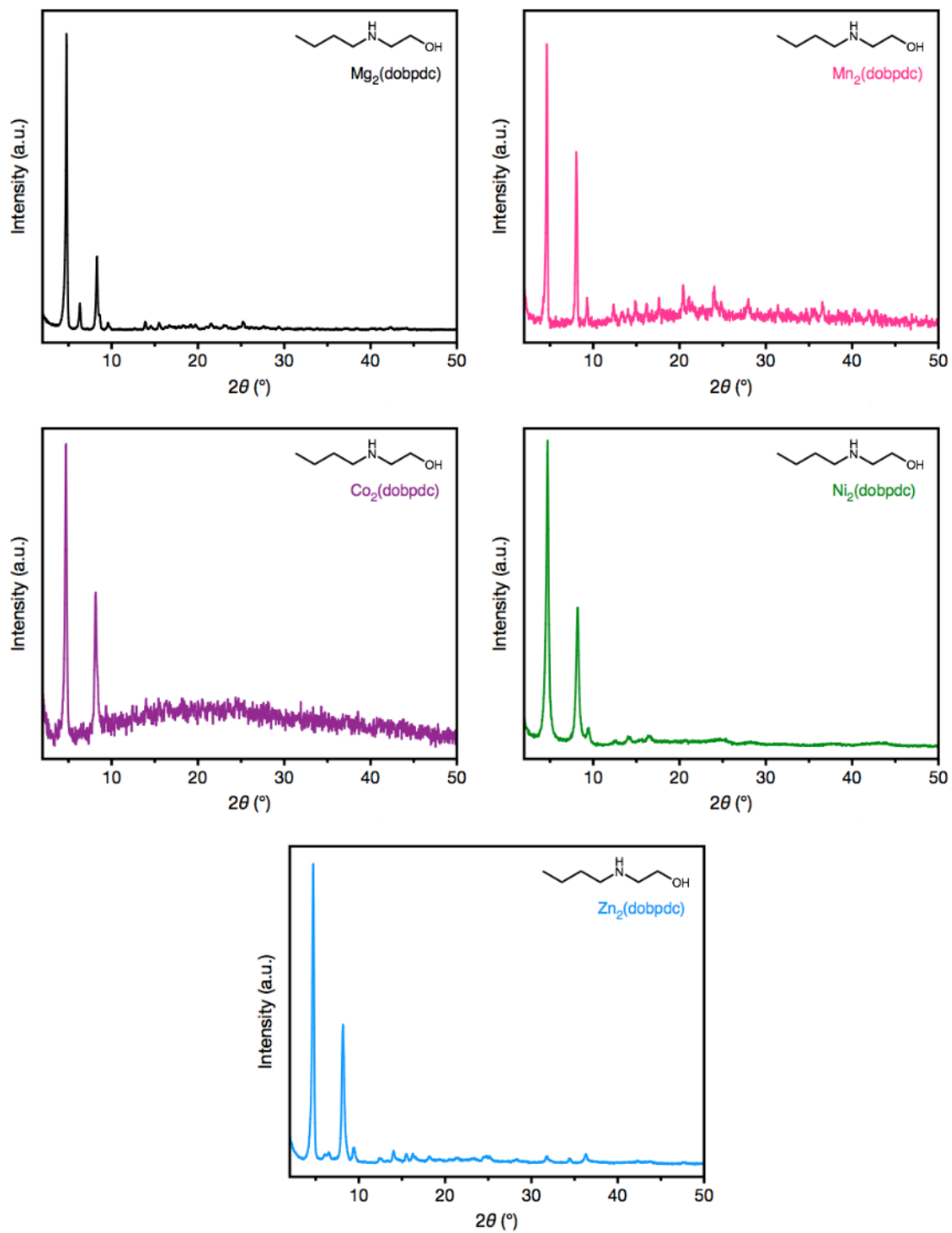
Figure S9. Powder X-ray diffraction pattern (CuKα radiation, λ = 1.5418 Å) of as-synthesized nBu-2-OH–Mg$_2$(dobpdc) (top left), nBu-2-OH–Mn$_2$(dobpdc) (top right), nBu-2-OH–Co$_2$(dobpdc) (middle left), nBu-2-OH–Ni$_2$(dobpdc) (middle right), and nBu-2-OH–Zn$_2$(dobpdc) (bottom).
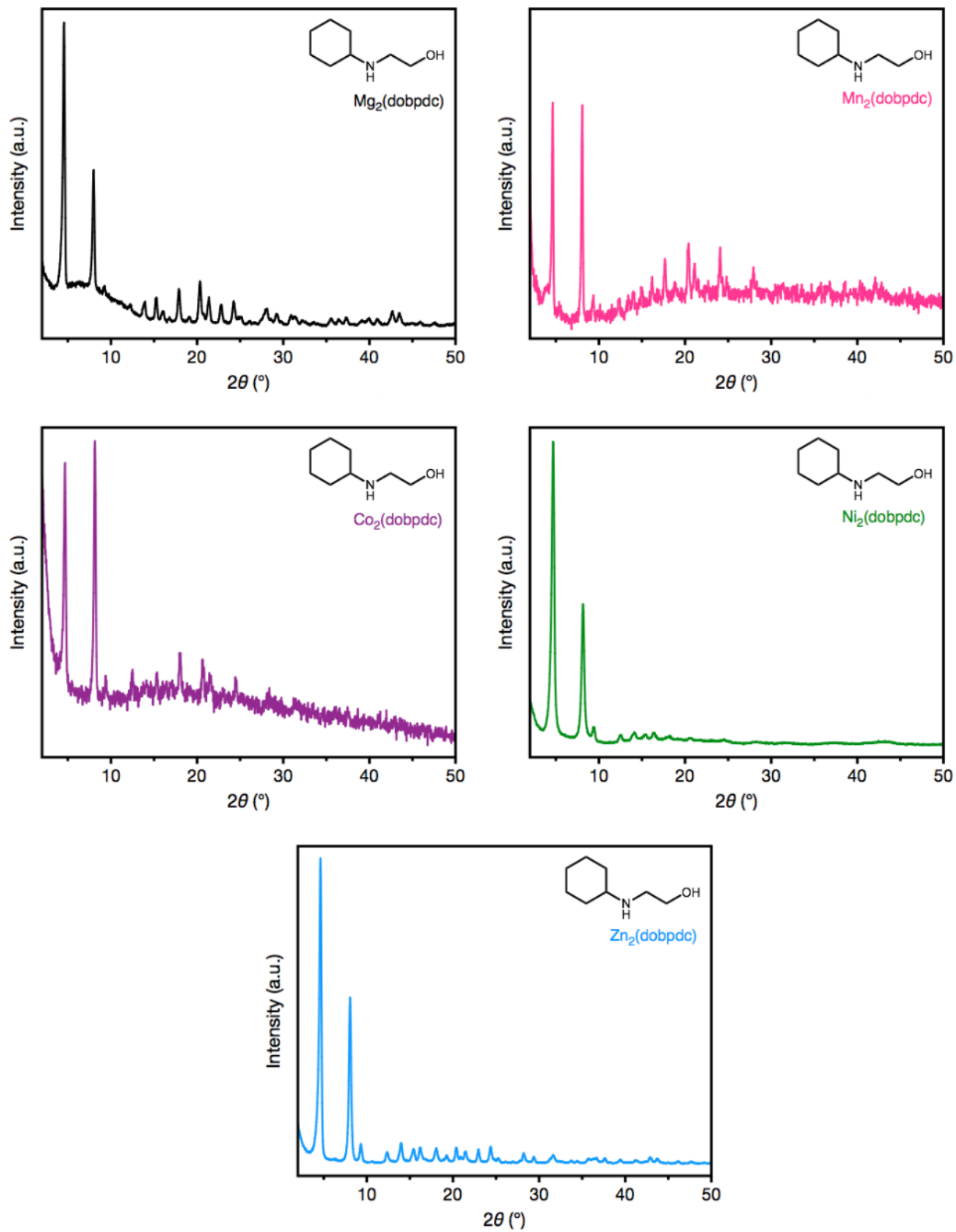
Figure S10. Powder X-ray diffraction pattern (CuKα radiation, λ = 1.5418 Å) of as-synthesized cy-2-OH–Mg$_2$(dobpdc) (top left), cy-2-OH–Mn$_2$(dobpdc) (top right), cy-2-OH–Co$_2$(dobpdc) (middle left), cy-2-OH–Ni$_2$(dobpdc) (middle right), and cy-2-OH–Zn$_2$(dobpdc) (bottom).
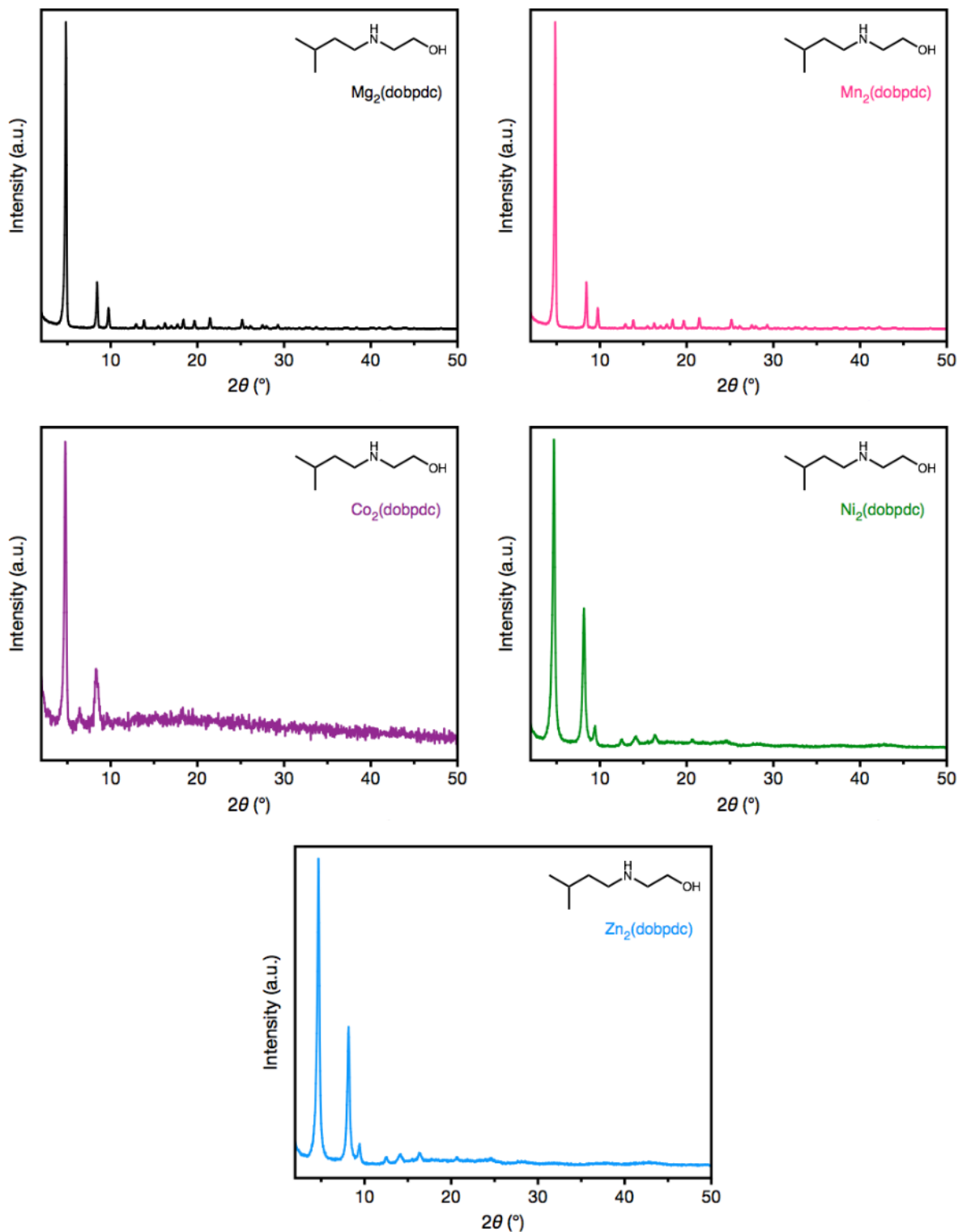
Figure S11. Powder X-ray diffraction pattern (CuKα radiation, λ = 1.5418 Å) of as-synthesized iPent-2-OH–Mg$_2$(dobpdc) (top left), iPent-2-OH–Mn$_2$(dobpdc) (top right), iPent-2-OH–Co$_2$(dobpdc) (middle left), iPent-2-OH–Ni$_2$(dobpdc) (middle right), and iPent-2-OH–Zn$_2$(dobpdc) (bottom).
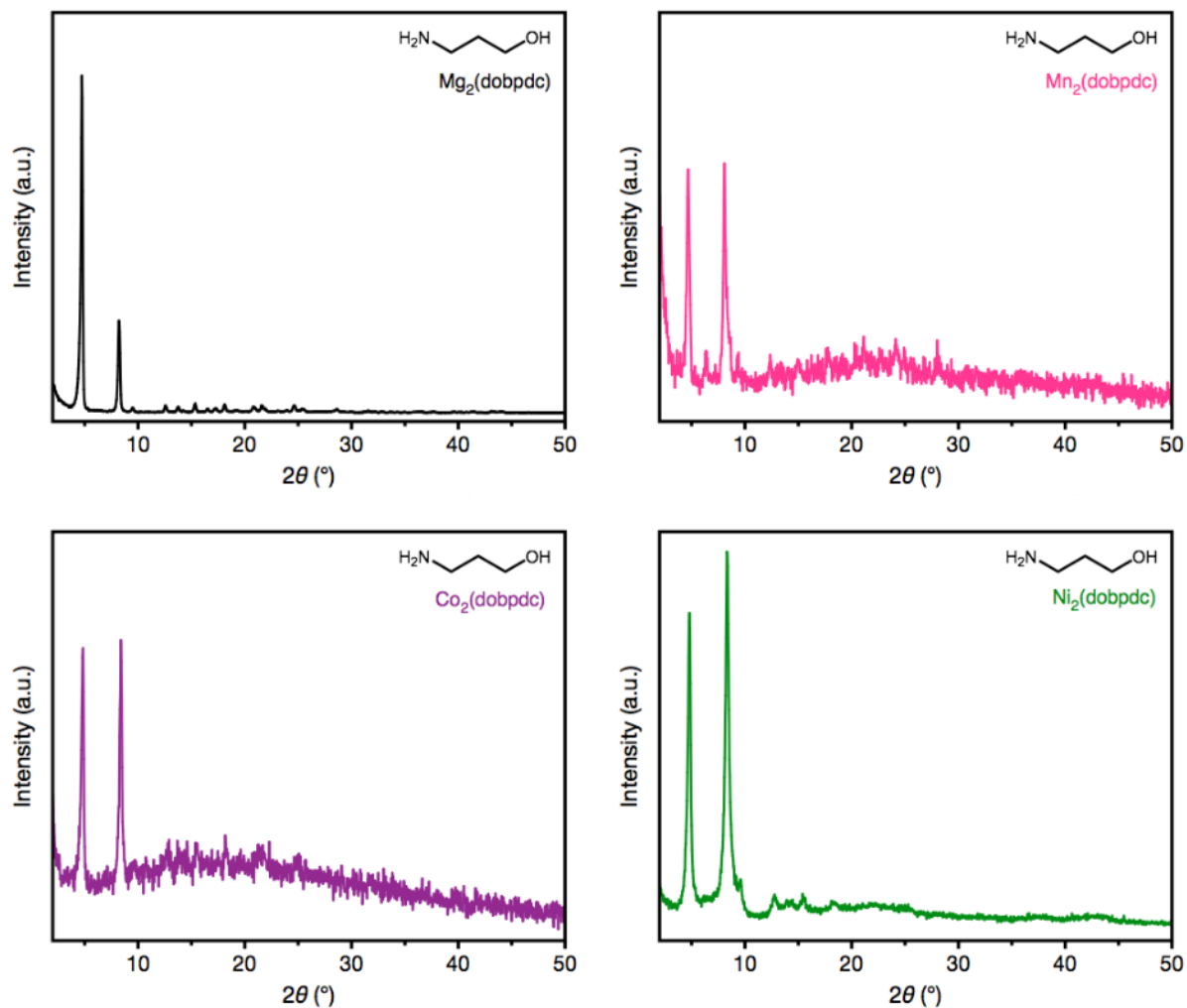
Figure S12. Powder X-ray diffraction pattern (CuKα radiation, λ = 1.5418 Å) of as-synthesized 3-OH–Mg$_2$(dobpdc) (top left), 3-OH–Mn$_2$(dobpdc) (top right), 3-OH–Co$_2$(dobpdc) (bottom left), and 3-OH–Ni$_2$(dobpdc) (bottom right). 3-OH–Zn$_2$(dobpdc) appeared to decompose and lose crystallinity by PXRD.
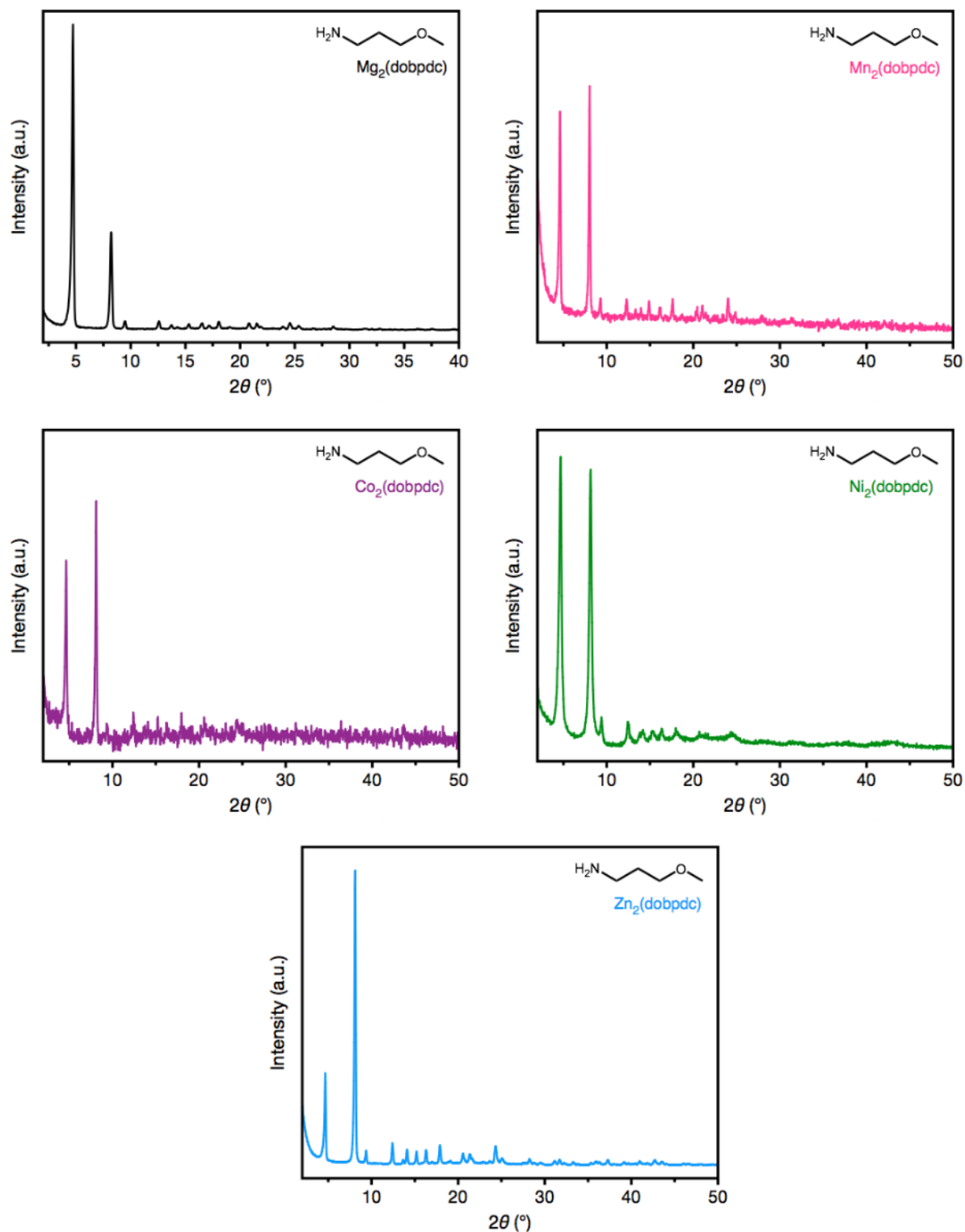
Figure S13. Powder X-ray diffraction pattern (CuKα radiation, λ = 1.5418 Å) of as-synthesized 3-O-m–Mg$_2$(dobpdc) (top left), 3-O-m–Mn$_2$(dobpdc) (top right), 3-O-m–Co$_2$(dobpdc) (middle left), 3-O-m–Ni$_2$(dobpdc) (middle right), and 3-O-m–Zn$_2$(dobpdc) (bottom).
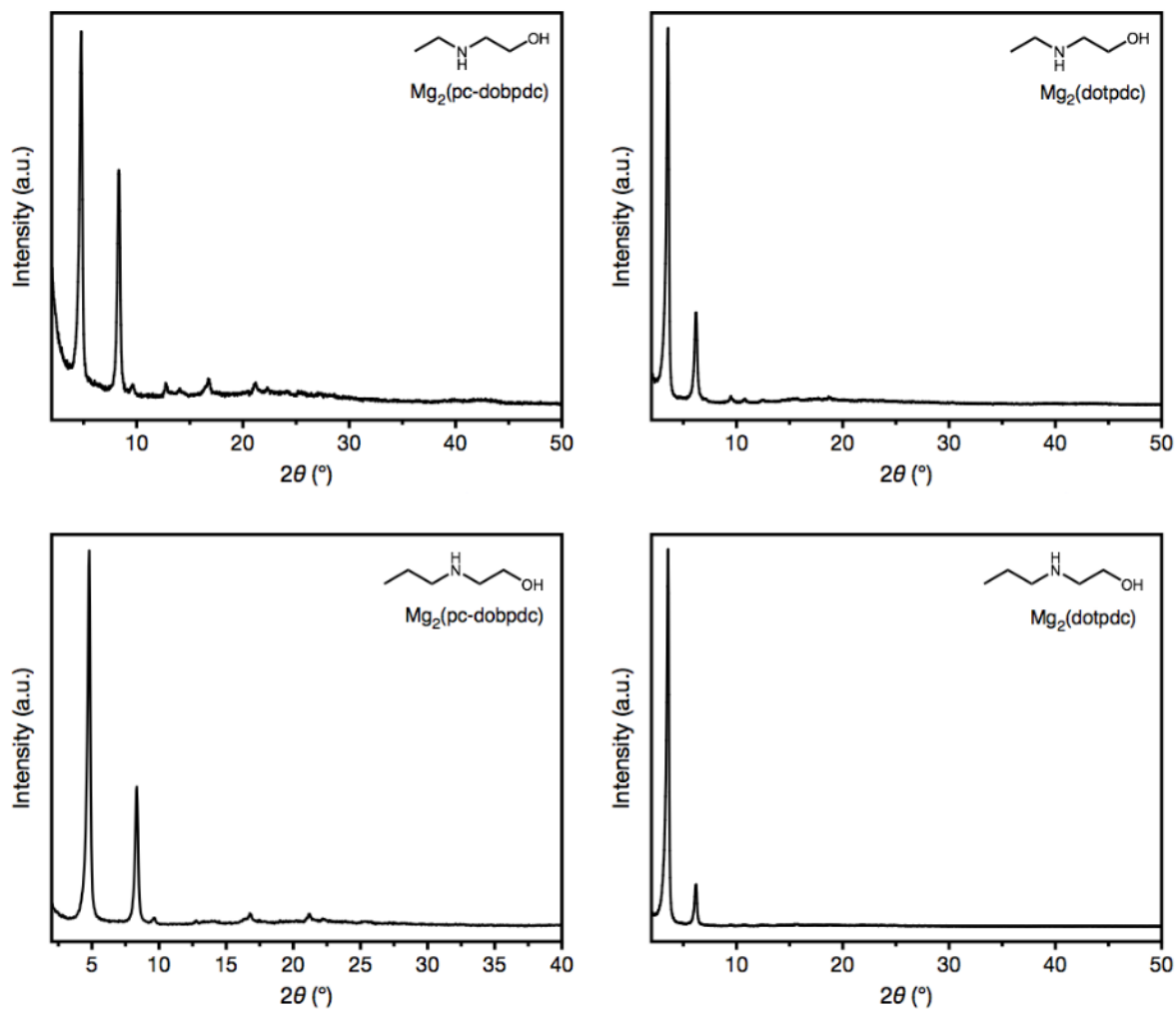
Figure S14. Powder X-ray diffraction pattern (CuKα radiation, λ = 1.5418 Å) of as-synthesized e-2-OH–Mg$_2$(pc-dobpdc) (top left), e-2-OH–Mg$_2$(dotpdc) (top right), nPr-2-OH–Mg$_2$(pc-dobpdc) (bottom left), and nPr-2-OH–Mg$_2$(dotpdc) (bottom right).
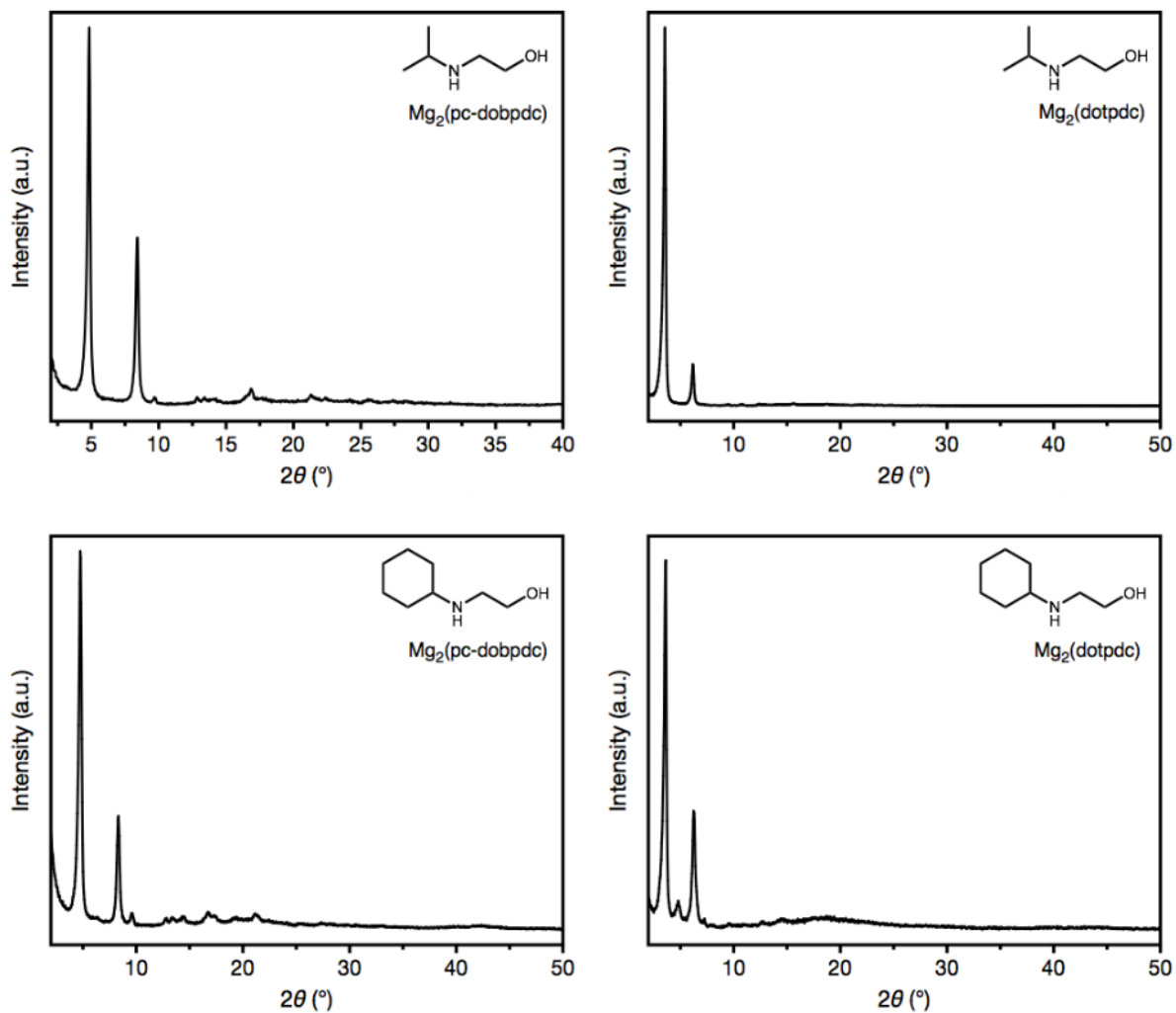
Figure S15. Powder X-ray diffraction pattern (CuKα radiation, λ = 1.5418 Å) of as-synthesized iPr-2-OH–Mg$_2$(pc-dobpdc) (top left), iPr-2-OH–Mg$_2$(dotpdc) (top right), cy-2-OH–Mg$_2$(pc-dobpdc) (bottom left), and cy-2-OH–Mg$_2$(dotpdc) (bottom right).
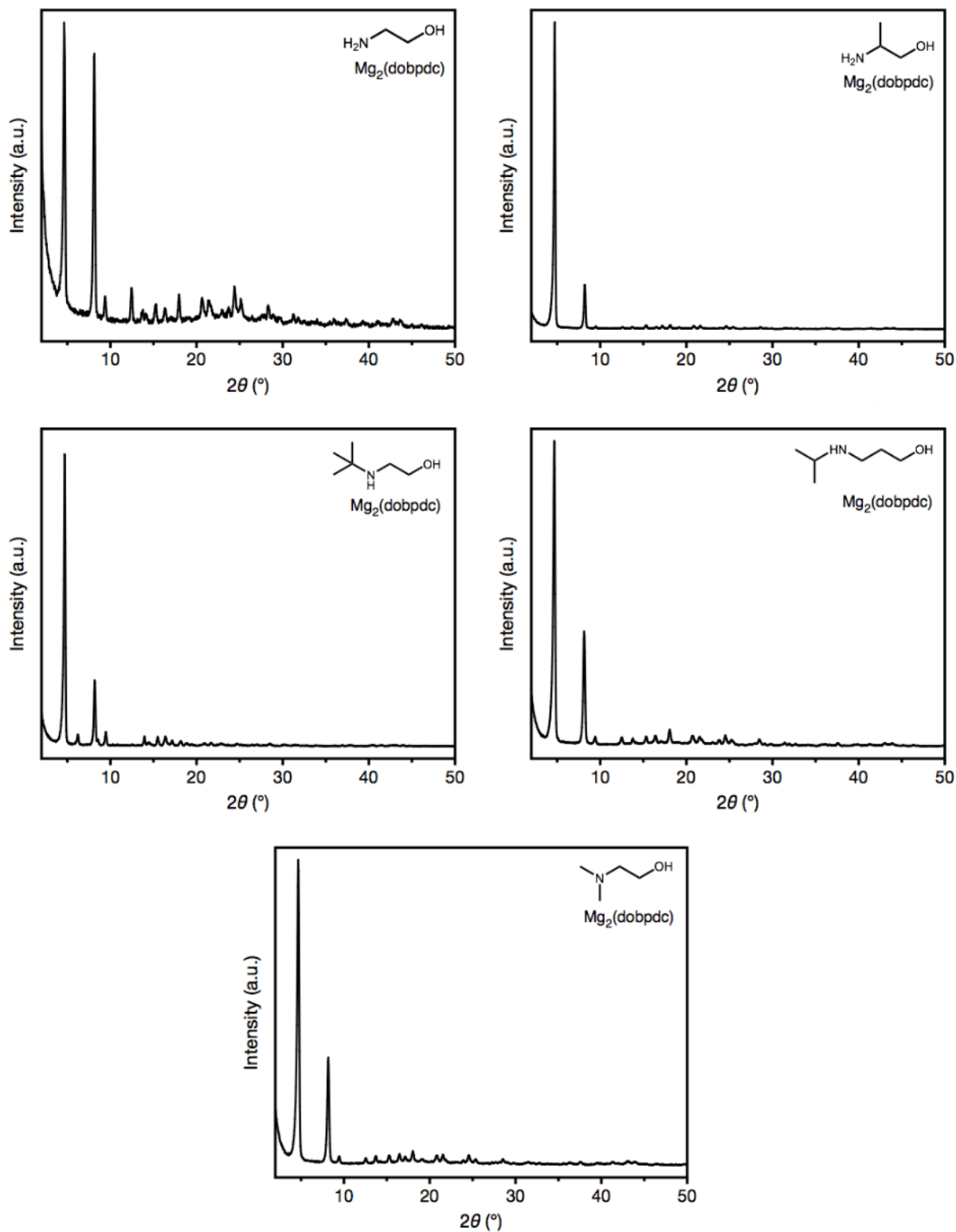
Figure S16. Powder X-ray diffraction pattern (CuKα radiation, λ = 1.5418 Å) of as-synthesized 2-OH–Mg$_2$(dobpdc) (top left), 2a-OH–Mg$_2$(dobpdc) (top right), tBu-2-OH–Mg$_2$(dobpdc) (middle left), iPr-3-OH–Mg$_2$(dobpdc) (middle right), and mm-2–Mg$_2$(dobpdc) (bottom).
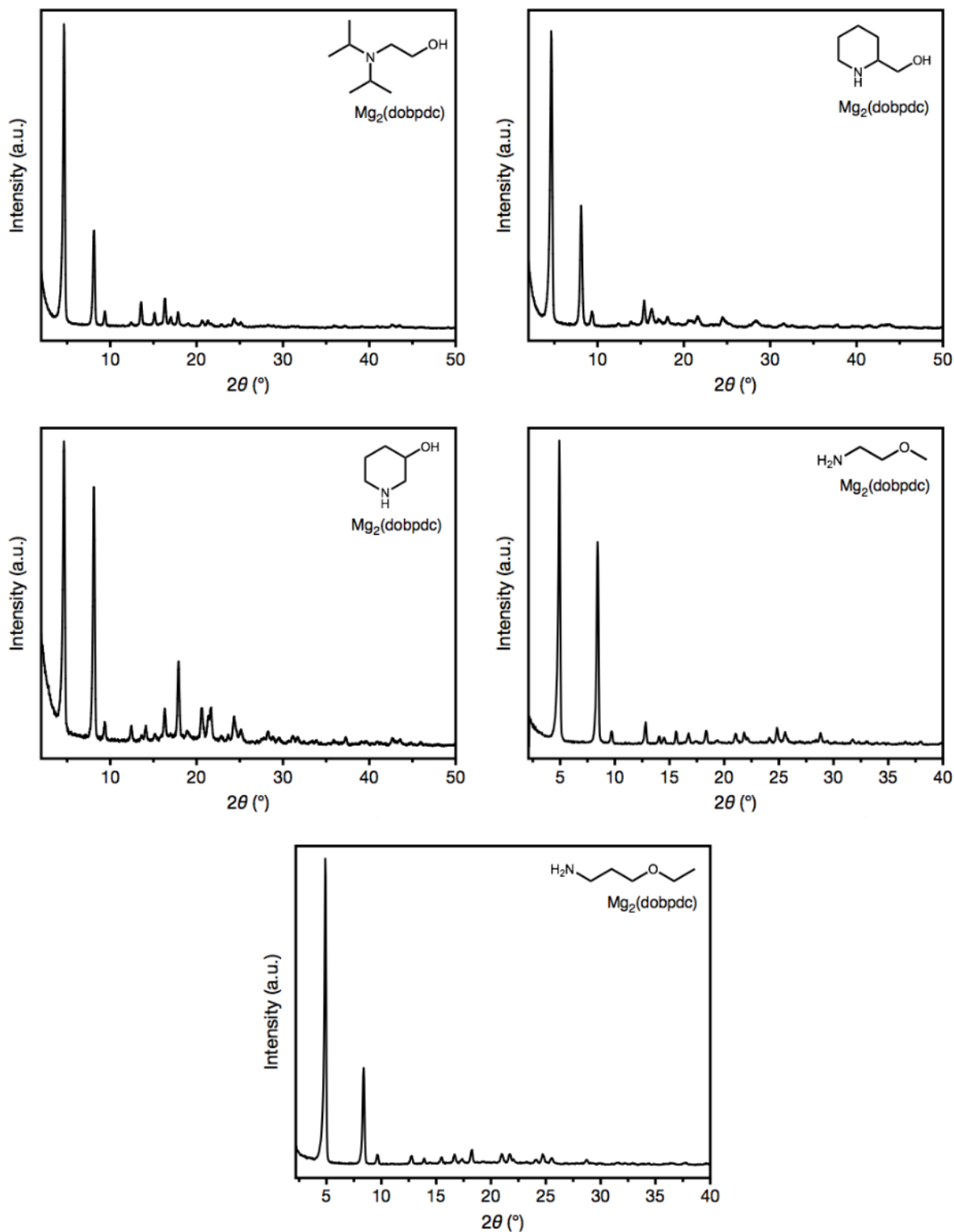
Figure S17. Powder X-ray diffraction pattern (CuKα radiation, λ = 1.5418 Å) of as-synthesized iPr,iPr-2-OH–Mg₂(dobpdc) (top left), pip-2-OH–Mg₂(dobpdc) (top right), pip-2,OH–Mg₂(dobpdc) (middle left), 2-O-m–Mg₂(dobpdc) (middle right), and 3-O-e–Mg₂(dobpdc) (bottom).
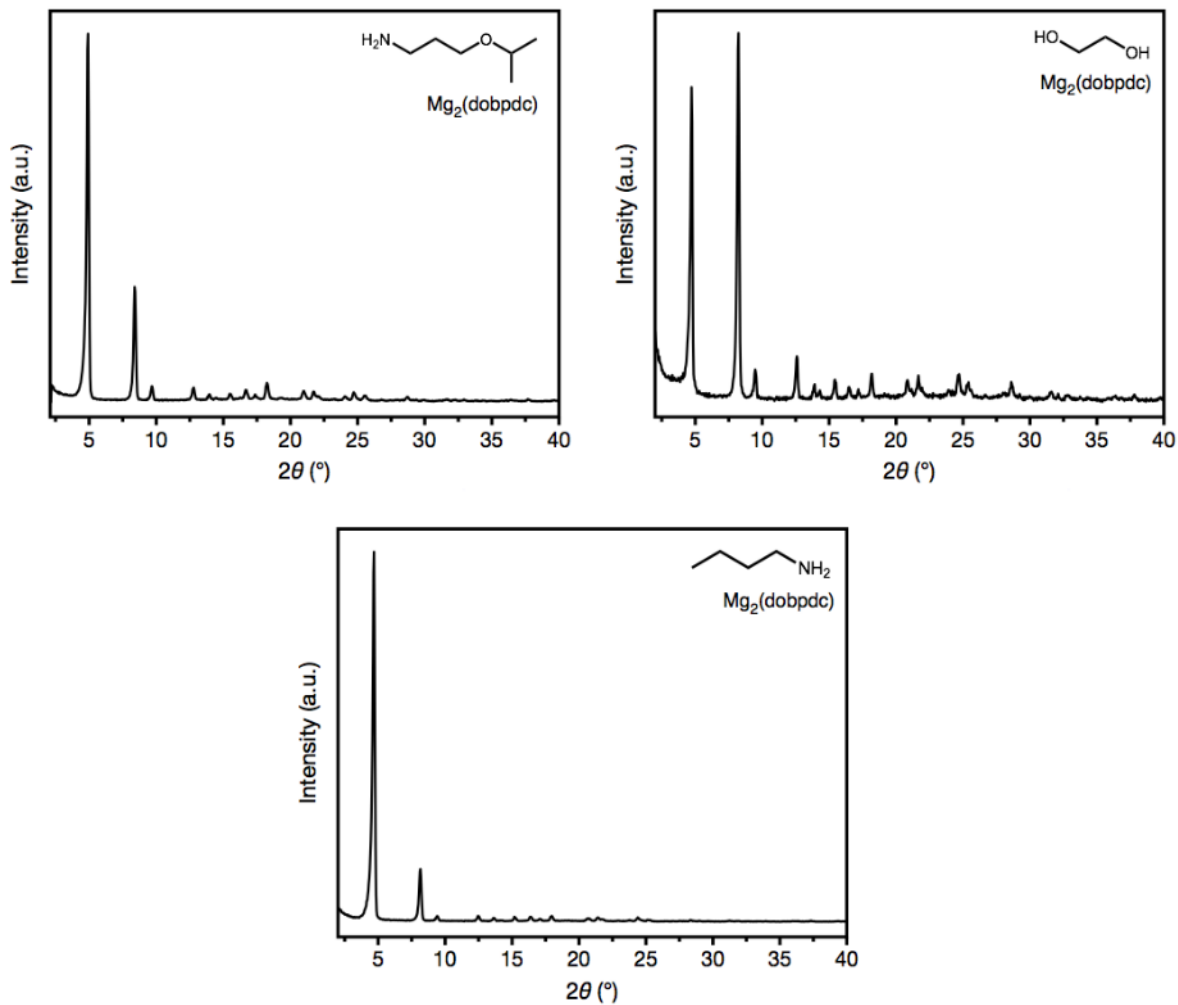
Figure S18. Powder X-ray diffraction pattern (CuKα radiation, λ = 1.5418 Å) of as-synthesized 3-O-iPr–Mg$_2$(dobpdc) (top left), OH-2-OH–Mg$_2$(dobpdc) (top right), and nBu–Mg$_2$(dobpdc) (bottom).

## 6. Infrared spectra of alcoholamine- and alkoxyalkylamine-appended frameworks
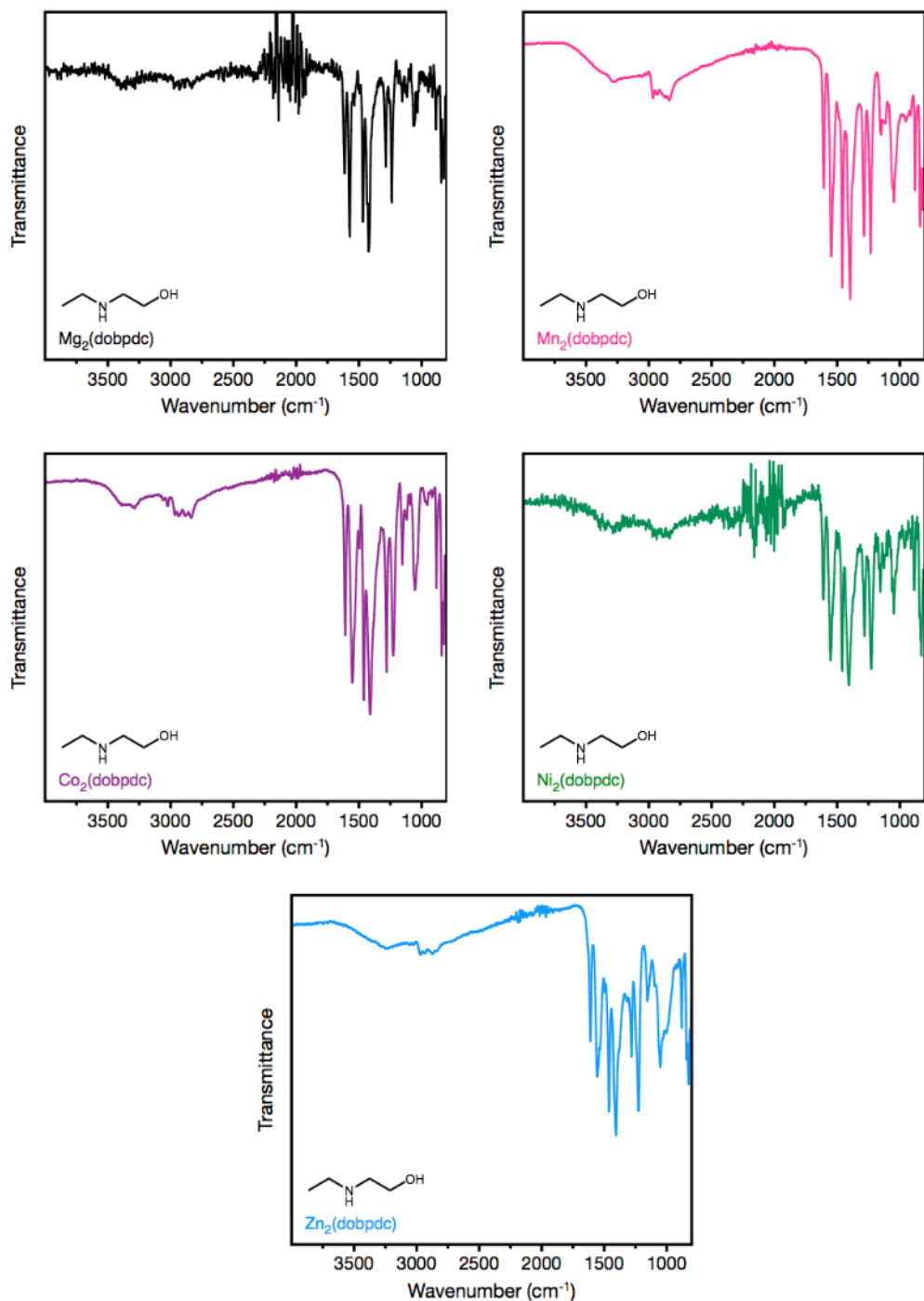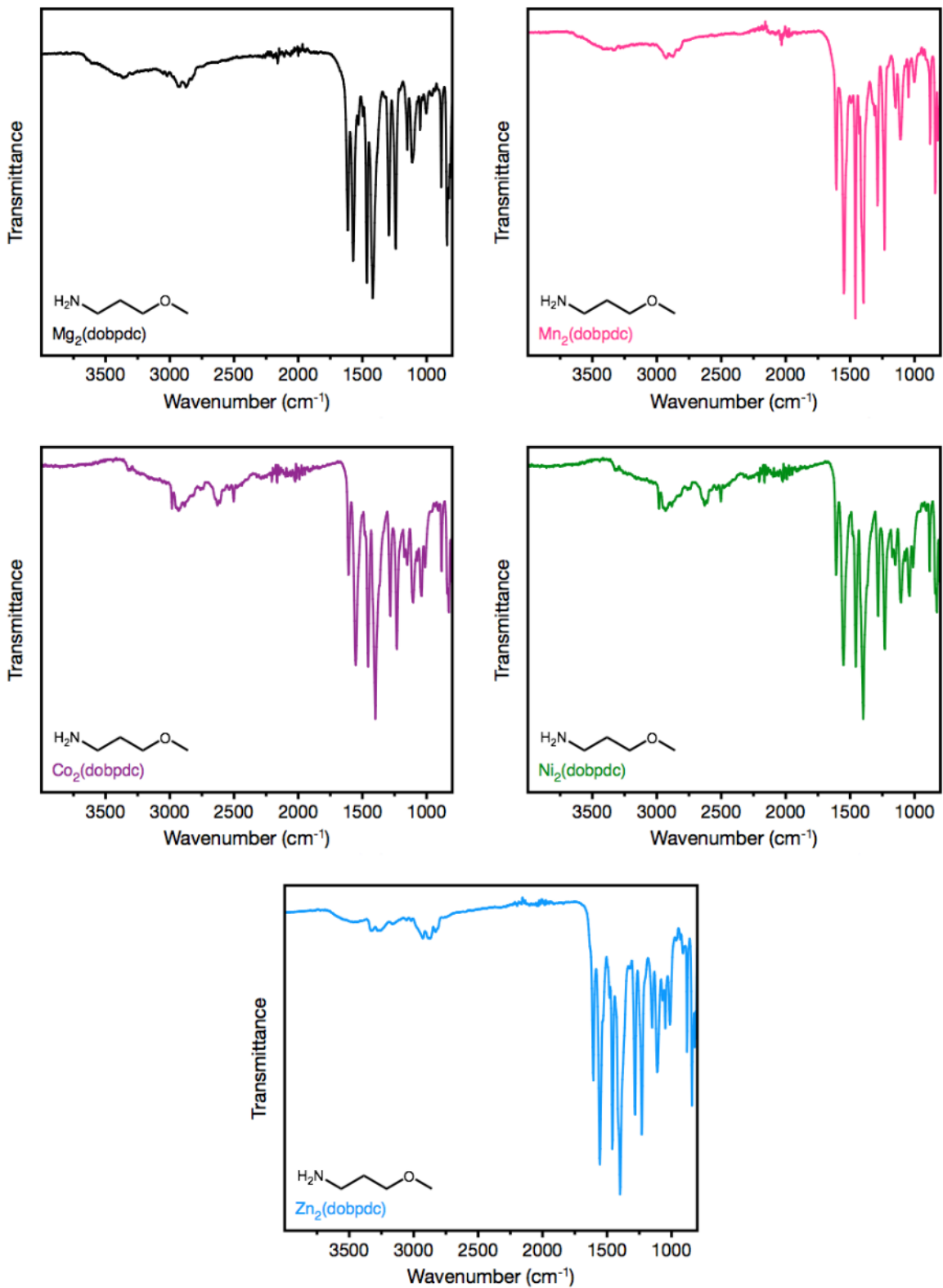

Figure S19. Infrared spectrum of as-synthesized e-2-OH–Mg$_2$(dobpdc) (top left), e-2-OH–Mn$_2$(dobpdc) (top right), e-2-OH–Co$_2$(dobpdc) (middle left), e-2-OH–Ni$_2$(dobpdc) (middle right), and e-2-OH–Zn$_2$(dobpdc) (bottom).
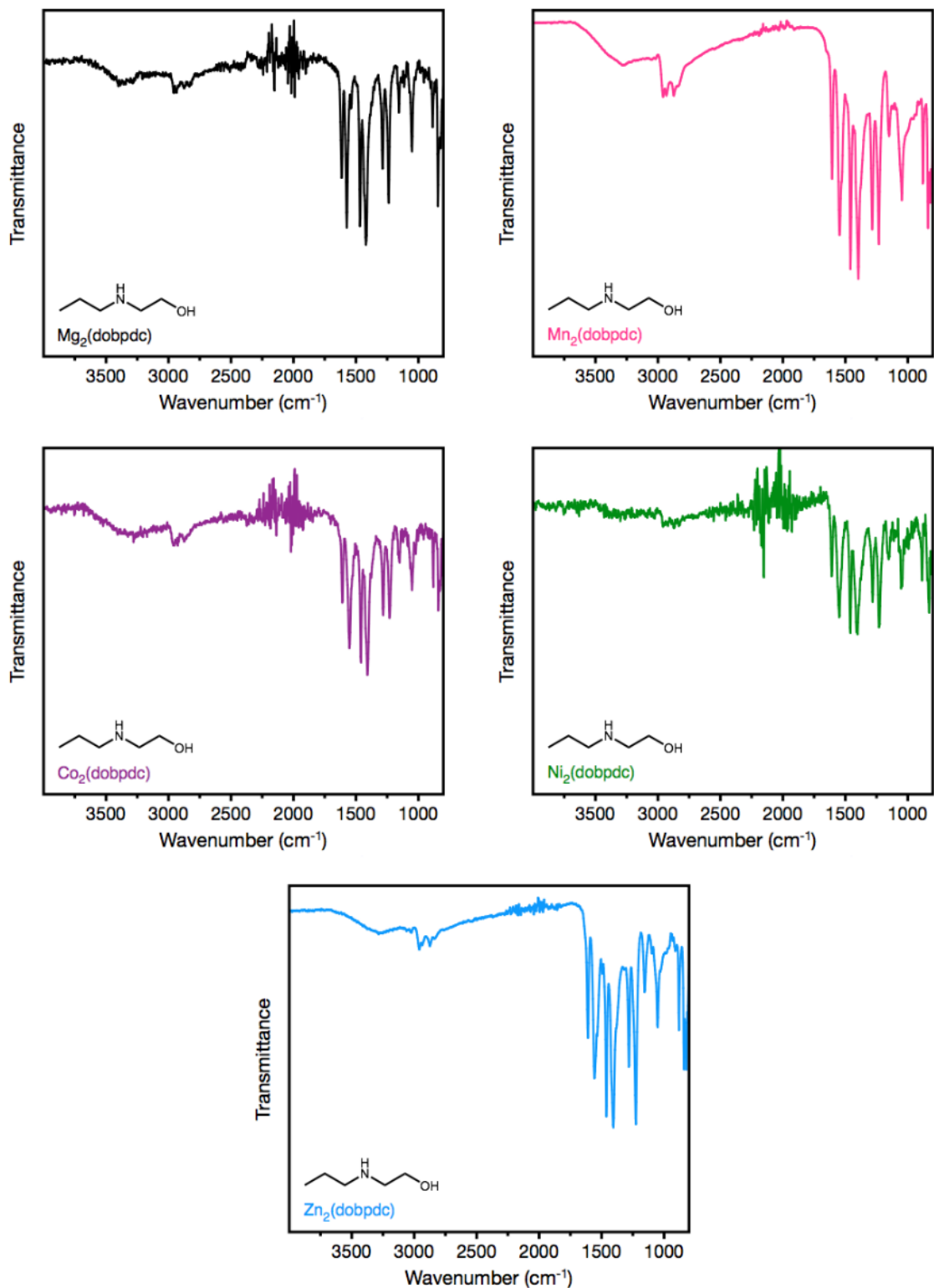
Figure S20. Infrared spectrum of as-synthesized nPr-2-OH–Mg$_2$(dobpdc) (top left), nPr-2-OH–Mn$_2$(dobpdc) (top right), nPr-2-OH–Co$_2$(dobpdc) (middle left), nPr-2-OH–Ni$_2$(dobpdc) (middle right), and nPr-2-OH–Zn$_2$(dobpdc) (bottom).
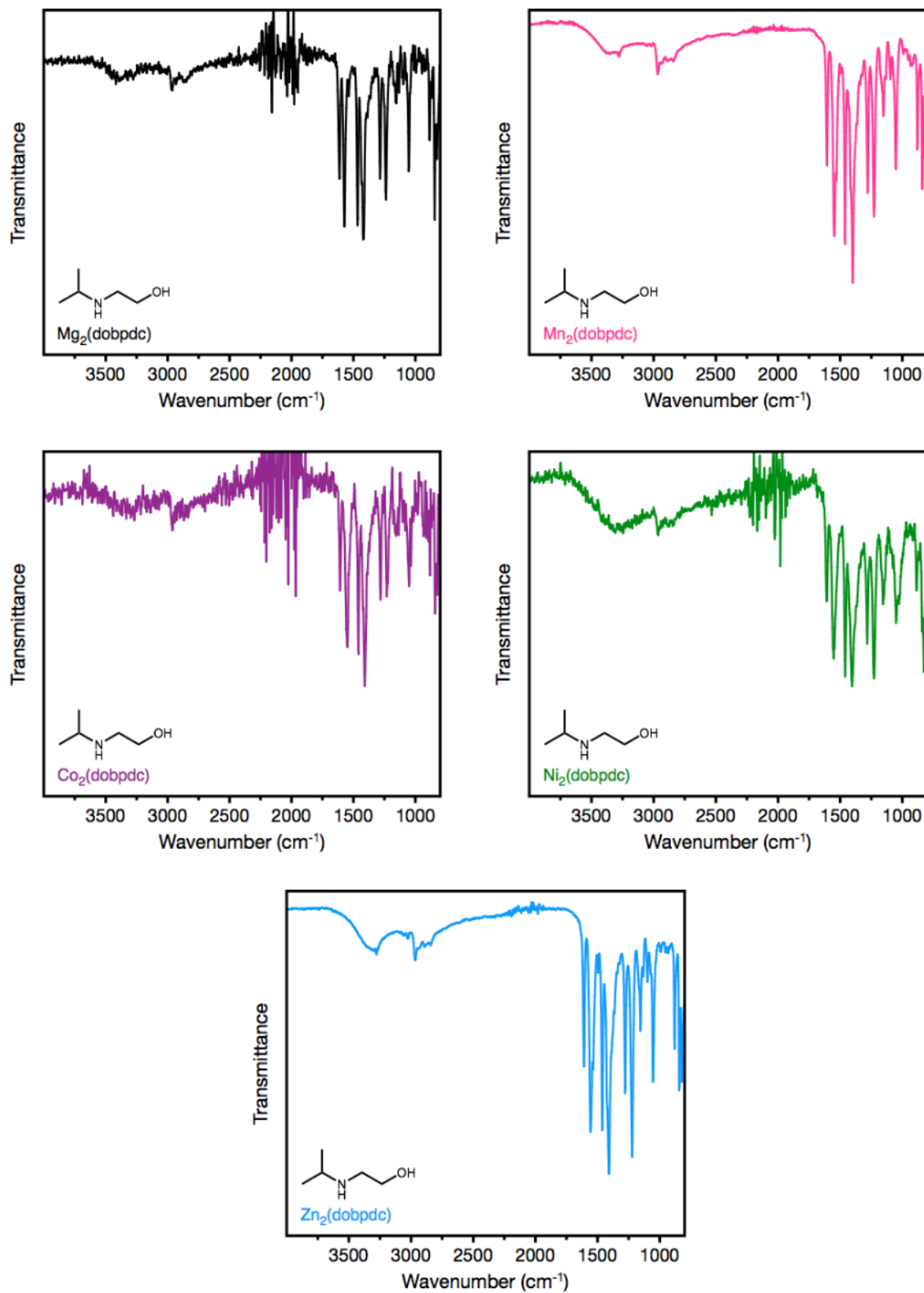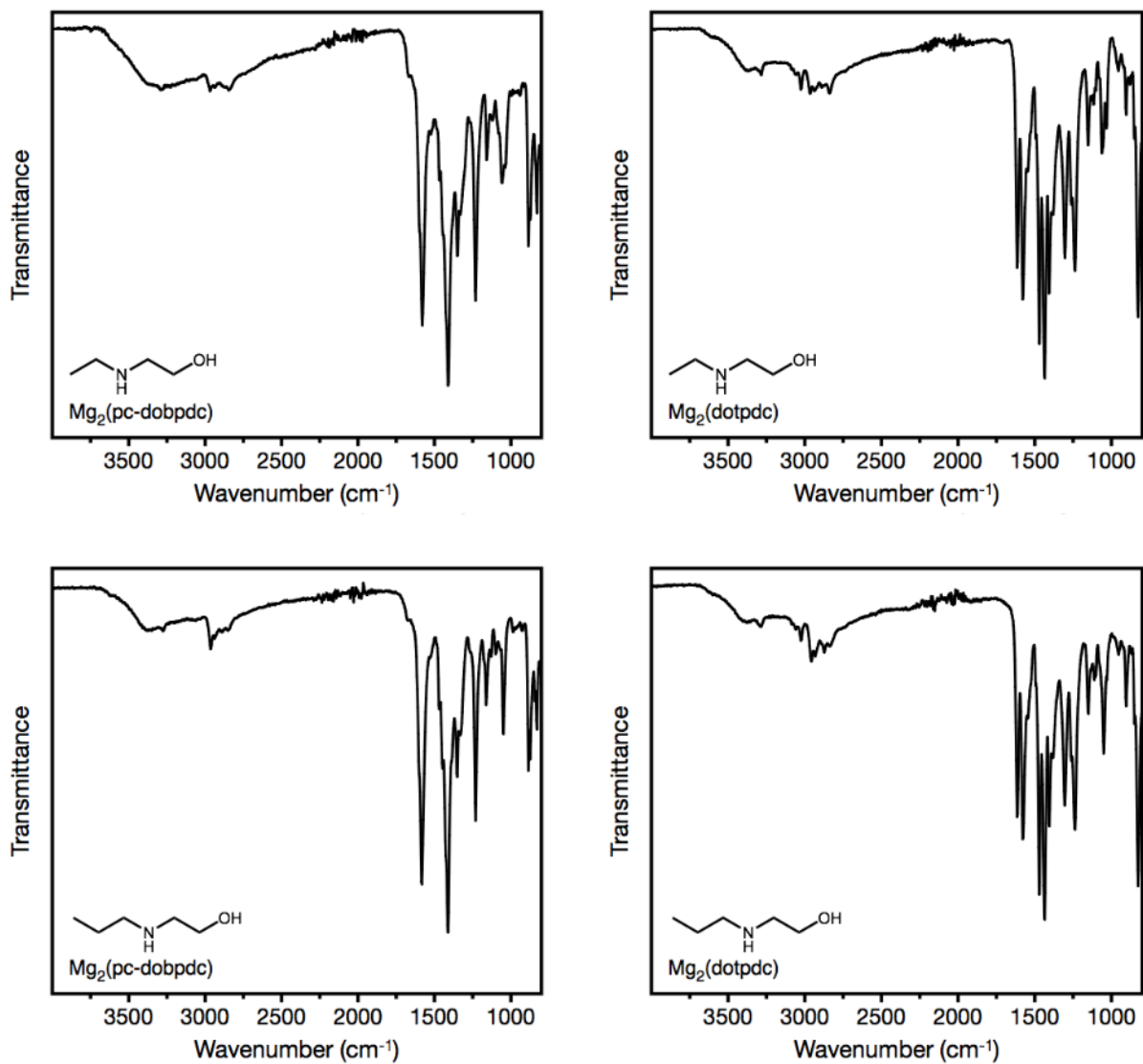
Figure S21. Infrared spectrum of as-synthesized iPr-2-OH–Mg₂(dobpdc) (top left), iPr-2-OH–Mn₂(dobpdc) (top right), iPr-2-OH–Co₂(dobpdc) (middle left), iPr-2-OH–Ni₂(dobpdc) (middle right), and iPr-2-OH–Zn₂(dobpdc) (bottom).
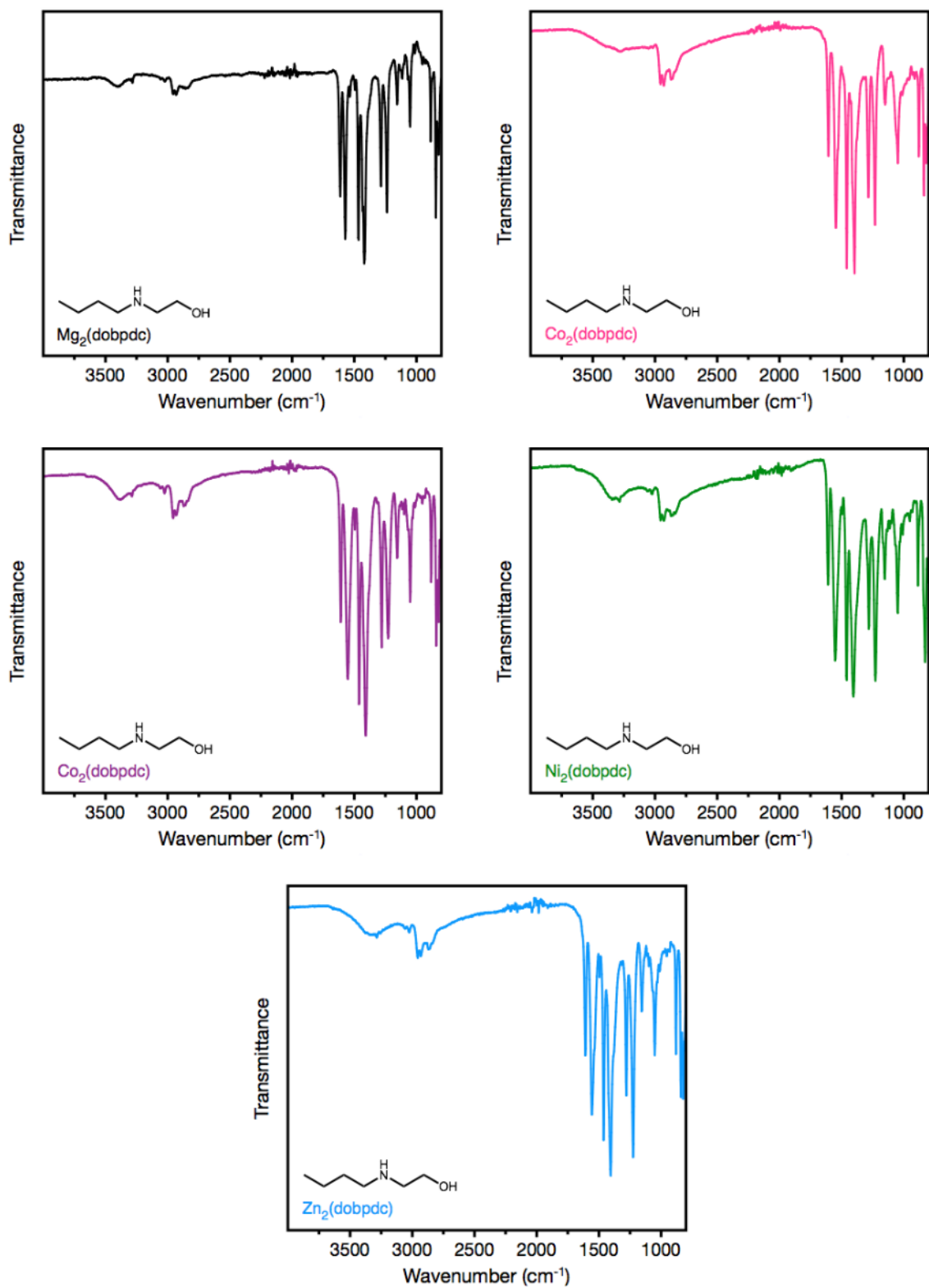
Figure S22. Infrared spectrum of as-synthesized nBu-2-OH–Mg$_2$(dobpdc) (top left), nBu-2-OH–Mn$_2$(dobpdc) (top right), nBu-2-OH–Co$_2$(dobpdc) (middle left), nBu-2-OH–Ni$_2$(dobpdc) (middle right), and nBu-2-OH–Zn$_2$(dobpdc) (bottom).
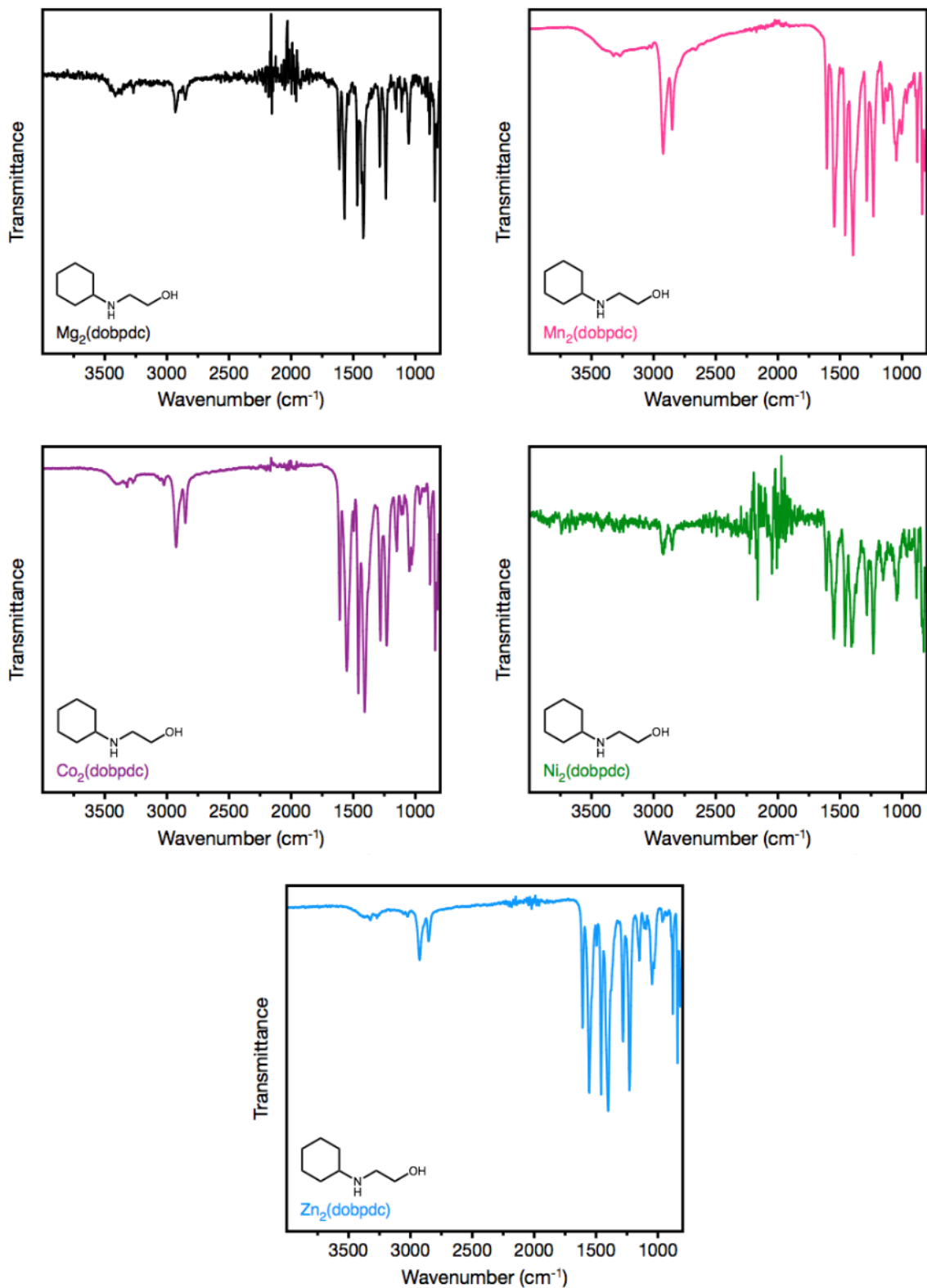
Figure S23. Infrared spectrum of as-synthesized cy-2-OH–Mg$_2$(dobpdc) (top left), cy-2-OH–Mn$_2$(dobpdc) (top right), cy-2-OH–Co$_2$(dobpdc) (middle left), cy-2-OH–Ni$_2$(dobpdc) (middle right), and cy-2-OH–Zn$_2$(dobpdc) (bottom).
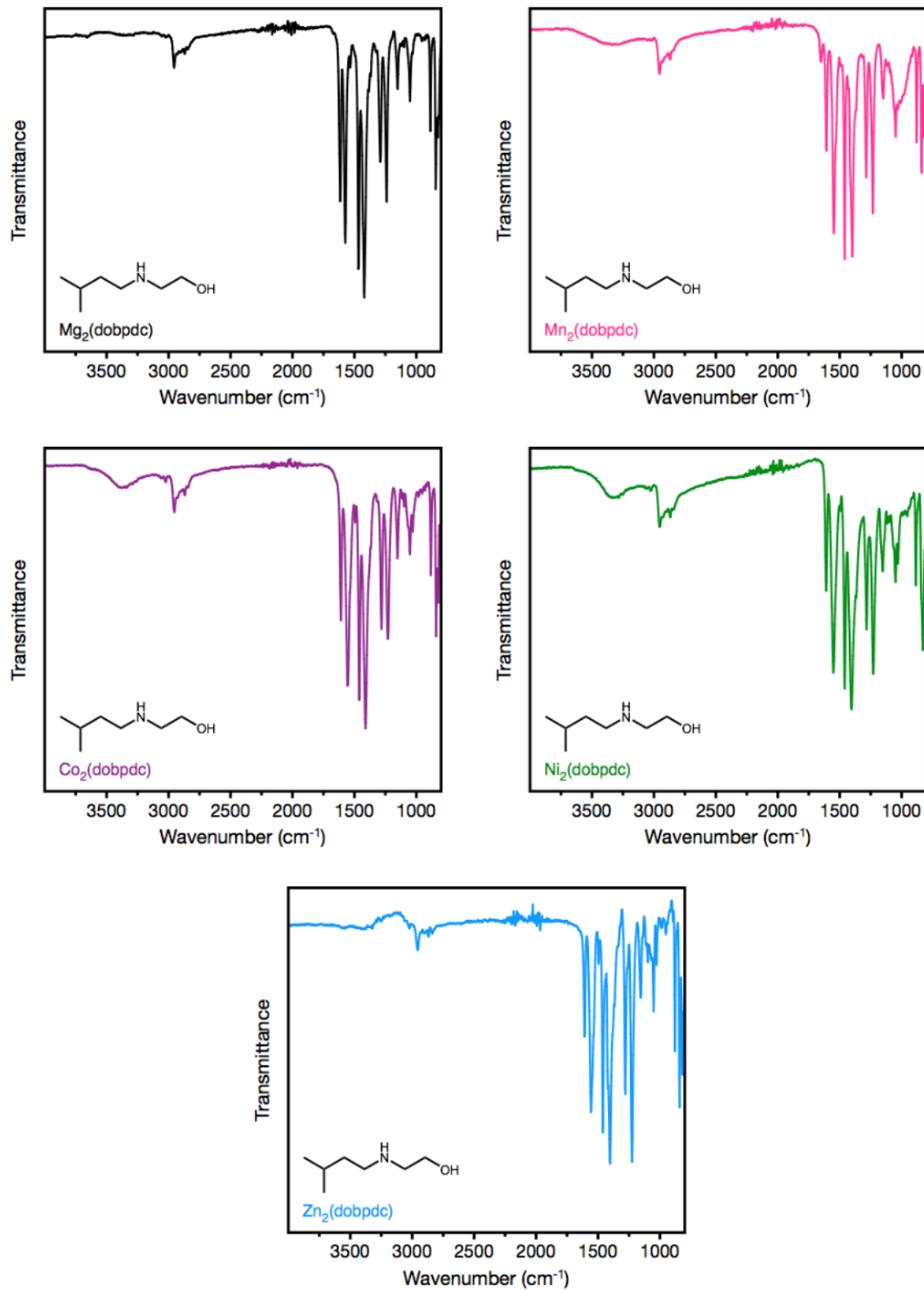
Figure S24. Infrared spectrum of as-synthesized iPent-2-OH–Mg$_2$(dobpdc) (top left), iPent-2-OH–Mn$_2$(dobpdc) (top right), iPent-2-OH–Co$_2$(dobpdc) (middle left), iPent-2-OH–Ni$_2$(dobpdc) (middle right), and iPent-2-OH–Zn$_2$(dobpdc) (bottom).
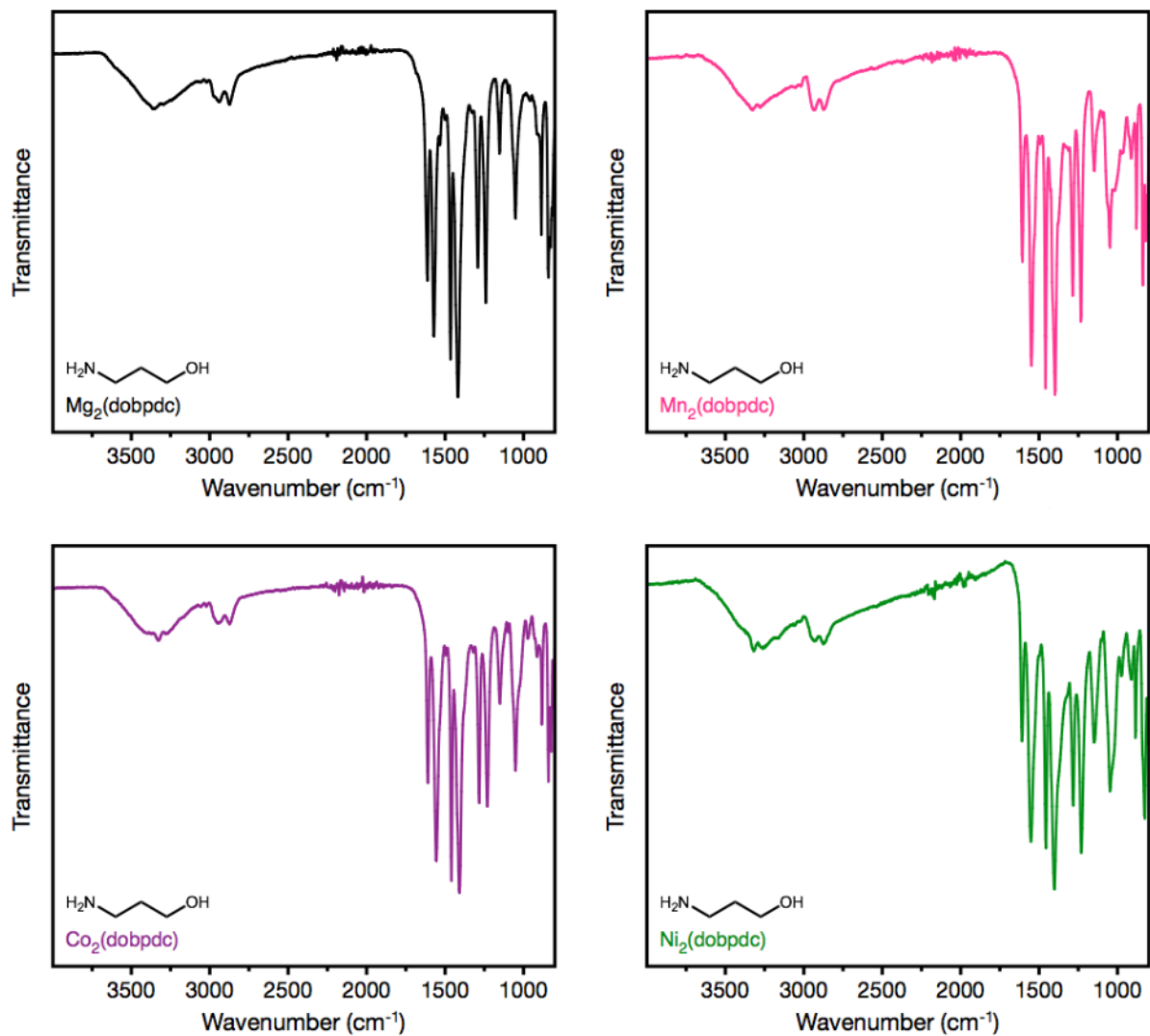
Figure S25. Infrared spectrum of as-synthesized 3-OH–Mg$_2$(dobpdc) (top left), 3-OH–Mn$_2$(dobpdc) (top right), 3-OH–Co$_2$(dobpdc) (bottom left), and 3-OH–Ni$_2$(dobpdc) (bottom right). Note that 3-OH–Zn$_2$(dobpdc) appeared to decompose and lost crystallinity by PXRD.

Figure S26. Infrared spectrum of as-synthesized 3-O-m–Mg$_2$(dobpdc) (top left), 3-O-m–Mn$_2$(dobpdc) (top right), 3-O-m–Co$_2$(dobpdc) (middle left), 3-O-m–Ni$_2$(dobpdc) (middle right), and 3-O-m–Zn$_2$(dobpdc) (bottom).

Figure S27. Infrared spectrum of as-synthesized e-2-OH–Mg$_2$(pc-dobpdc) (top left), e-2-OH–Mg$_2$(dotpdc) (top right), nPr-2-OH–Mg$_2$(pc-dobpdc) (bottom left), and nPr-2-OH–Mg$_2$(dotpdc) (bottom right).
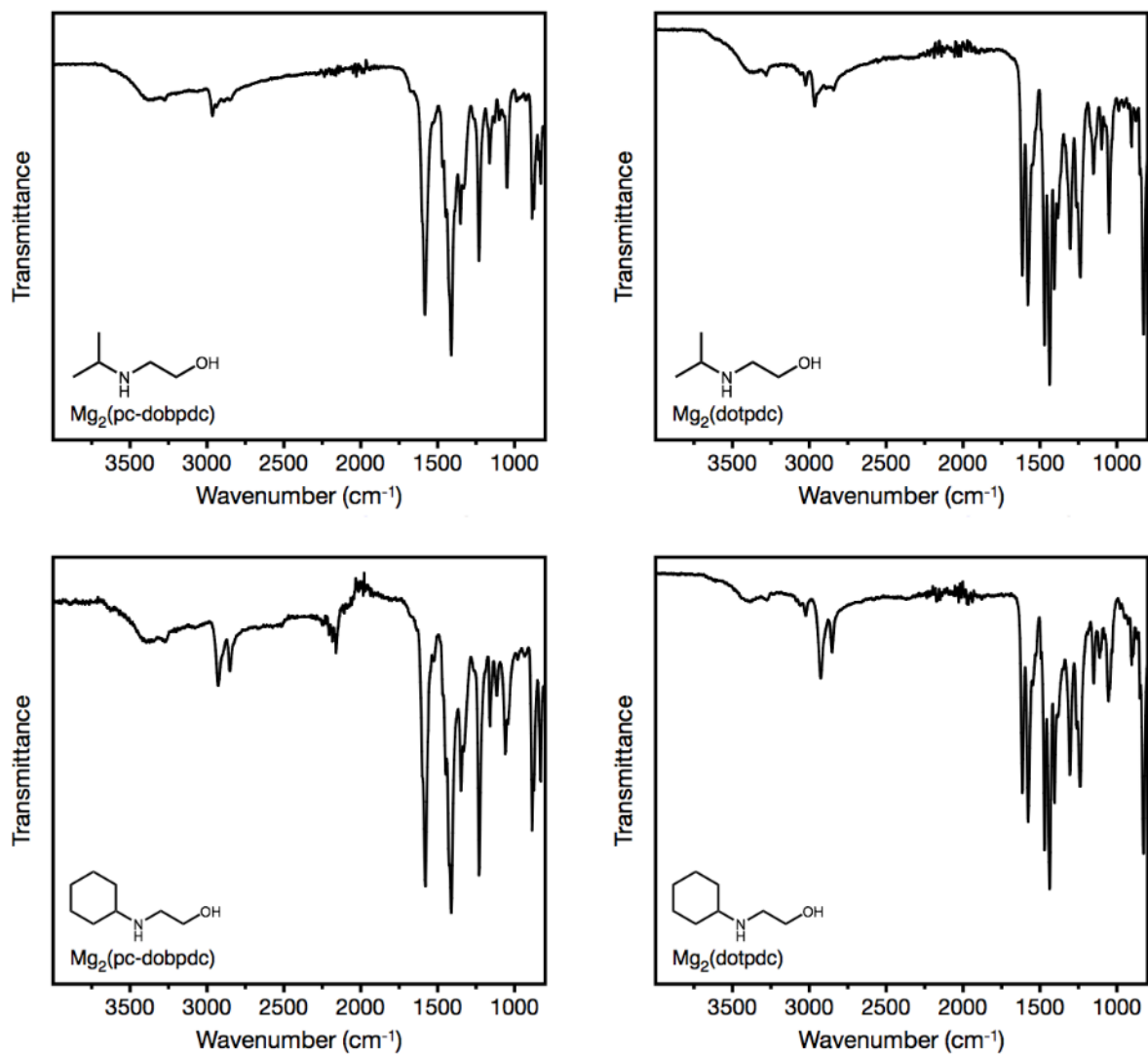
Figure S28. Infrared spectrum of as-synthesized iPr-2-OH–Mg$_2$(pc-dobpdc) (top left), iPr-2-OH–Mg$_2$(dotpdc) (top right), cy-2-OH–Mg$_2$(pc-dobpdc) (bottom left), and cy-2-OH–Mg$_2$(dotpdc) (bottom right).
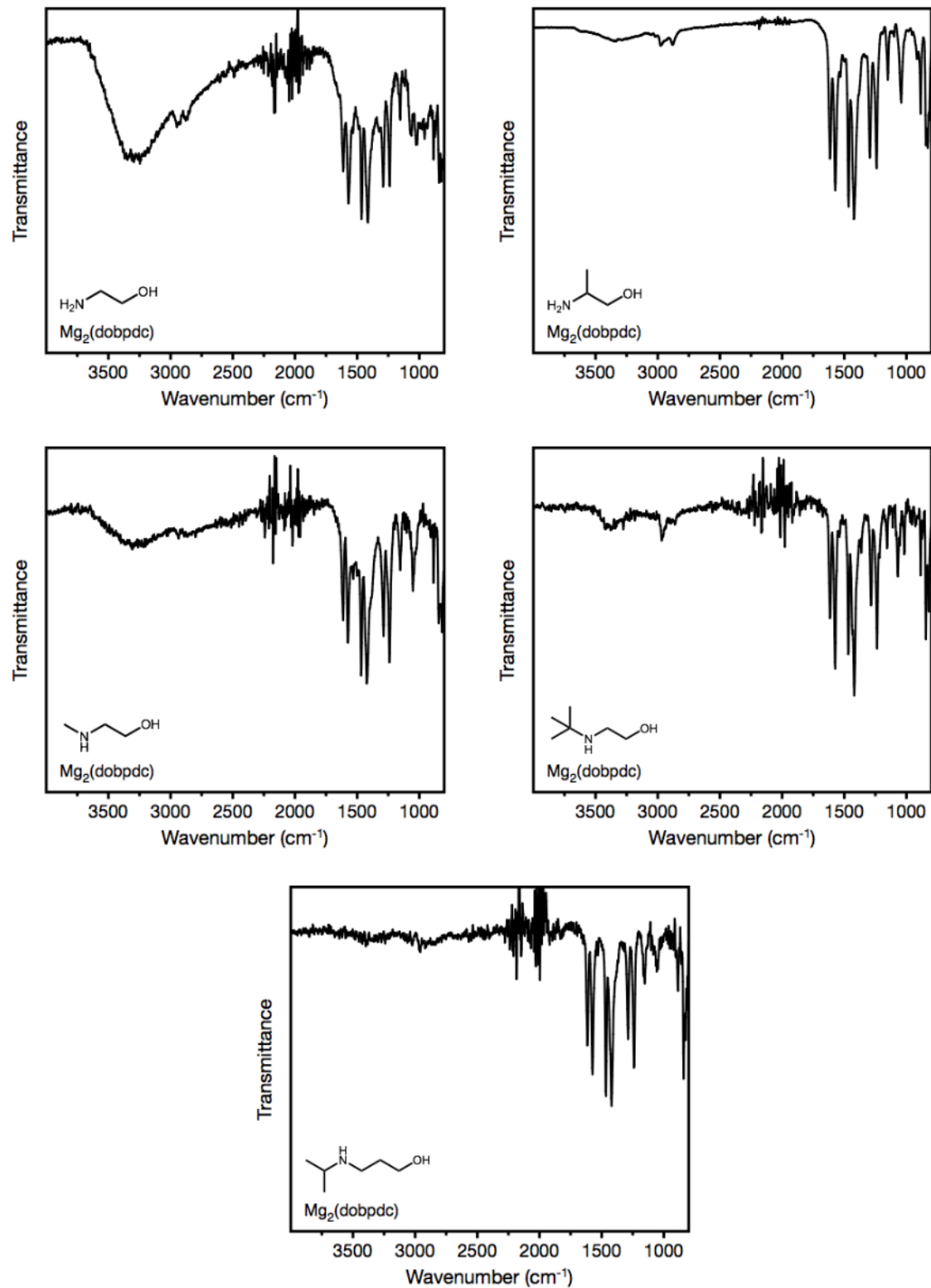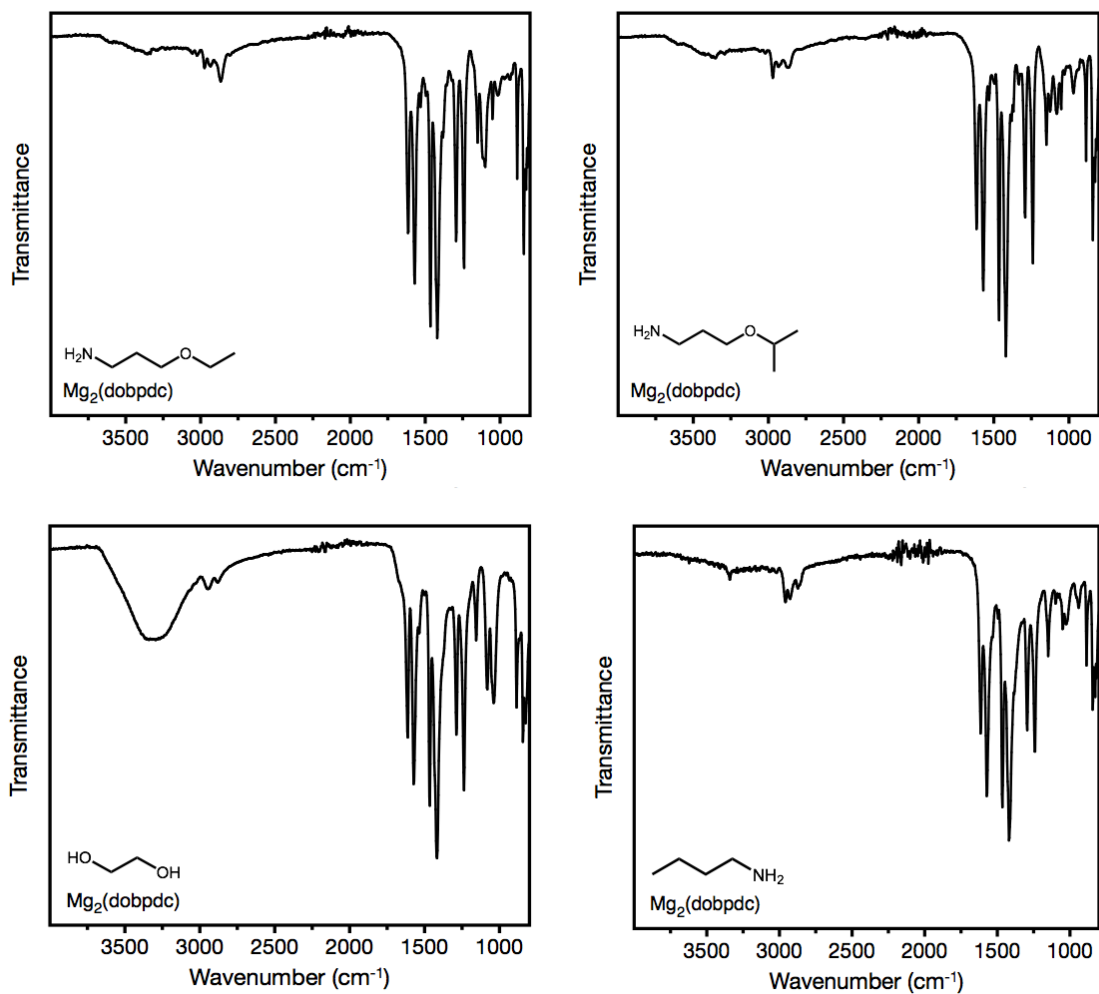
Figure S29. Infrared spectrum of as-synthesized 2-OH–Mg$_2$(dobpdc) (top left), 2a-OH–Mg$_2$(dobpdc) (top right), m-2-OH–Mg$_2$(dobpdc) (middle left), tBu-2-OH–Mg$_2$(dobpdc) (middle right), and iPr-3-OH– Mg$_2$(dobpdc) (bottom).
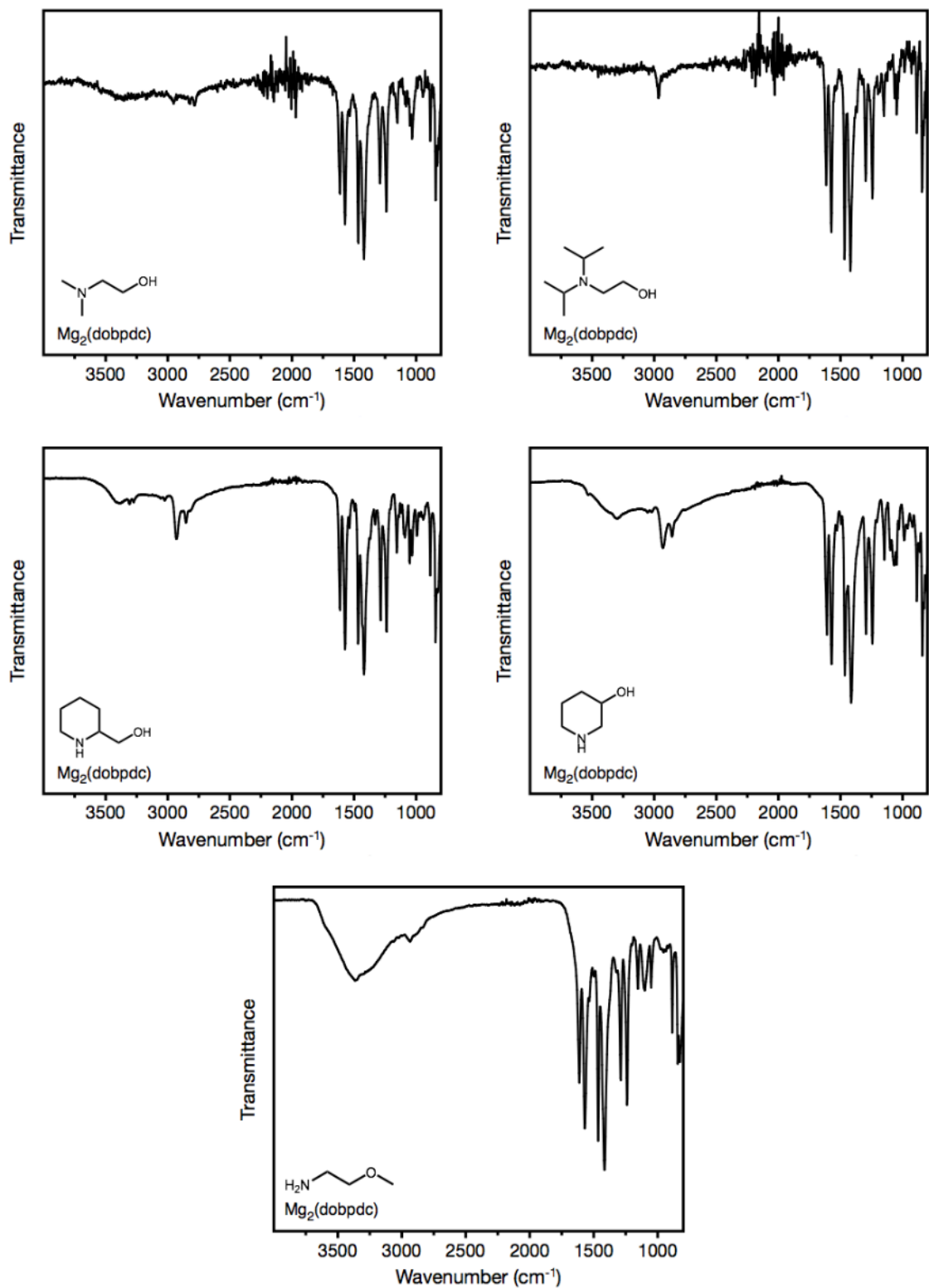
Figure S30. Infrared spectrum of as-synthesized mm-2-OH–Mg$_2$(dobpdc) (top left), iPr,iPr-2-OH–Mg$_2$(dobpdc) (top right), pip-2-OH–Mg$_2$(dobpdc) (middle left), pip-2,OH–Mg$_2$(dobpdc) (middle right), and 2-O-m–Mg$_2$(dobpdc) (bottom).

Figure S31. Infrared spectrum of as-synthesized 3-O-e–Mg$_2$(dobpdc) (top left), 3-O-iPr–Mg$_2$(dobpdc) (top right), OH-2-OH–Mg$_2$(dobpdc) (middle left), and nBu–Mg$_2$(dobpdc) (bottom).

7. Activated and CO₂-dosed infrared spectra of alcoholamine-appended Mg₂(dobpdc)
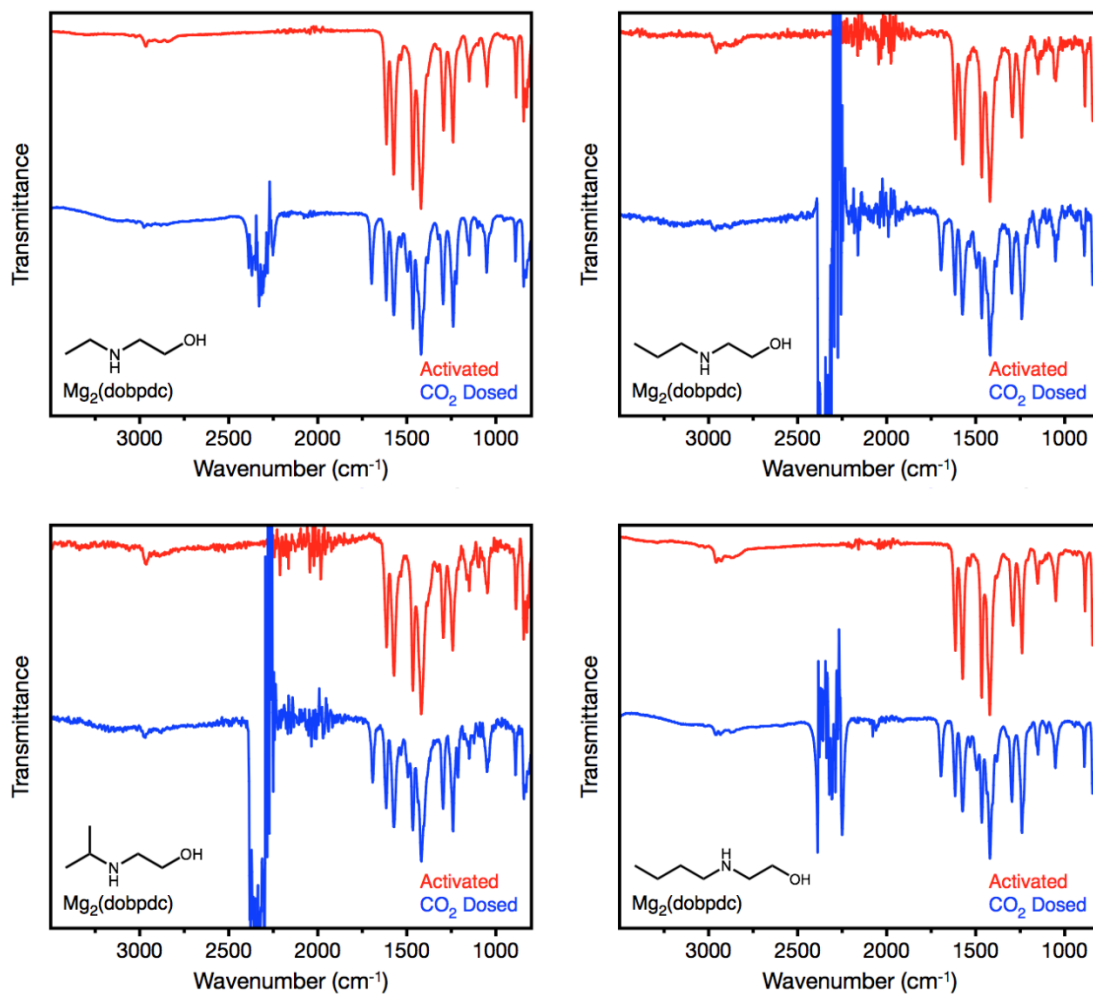
Figure S32. Infrared spectrum of activated e-2-OH–Mg₂(dobpdc) (top left), nBu-2-OH–Mg₂(dobpdc) (top right), iPr-2-OH–Mg₂(dobpdc) (bottom left), and nBu-2-OH–Mg₂(dobpdc) (bottom right) under an environment of dry N_2 (red) and dry CO_2 (blue).
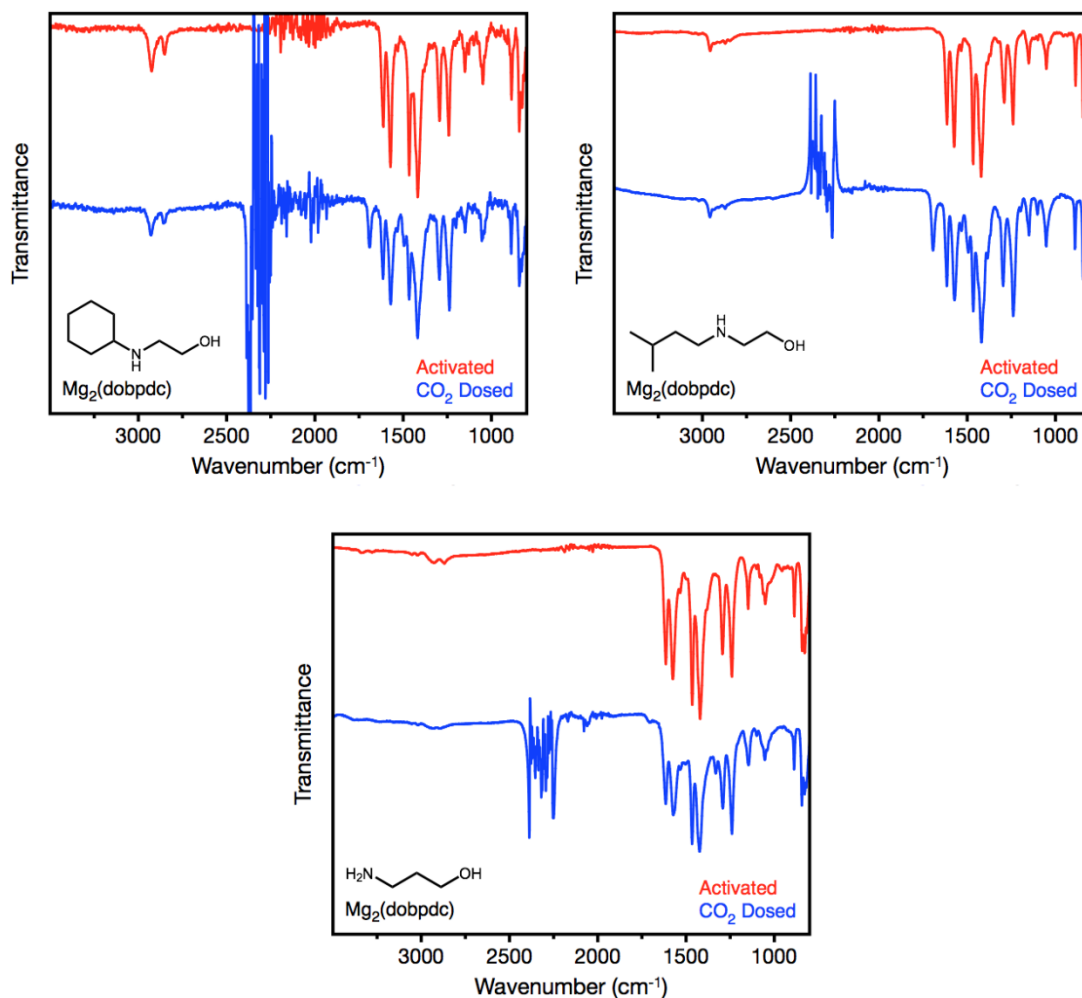
Figure S33. IR spectra for activated cy-2-OH–Mg$_2$(dobpdc) (top left), iPent-2-OH–Mg$_2$(dobpdc) (top right), and 3-OH–Mg$_2$(dobpdc) (bottom) under dry N$_2$ (red) and dry CO$_2$ (blue).

Table S1. New stretching frequencies appearing in the CO$_2$-dosed spectra for each alcoholamine-appended Mg$_2$(dobpdc) material. Note that e-2-OH and 3-OH materials exhibit new stretches at 1330 cm^{-1} that are not evident for the other alcoholamines.

| Alcoholamine	New Stretching Frequencies ν (cm^{-1})
e-2-OH	1695, 1495, 1440, 1405, 1330, 1220
nPr-2-OH	1695, 1495, 1440, 1210
iPr-2-OH	1695, 1495, 1440, 1405, 1210
nBu-2-OH	1695, 1495, 1440, 1405, 1100
cy-2-OH	1690, 1495, 1200
iPent-2-OH	1695, 1495, 1380, 1100
3-OH	1710, 1330

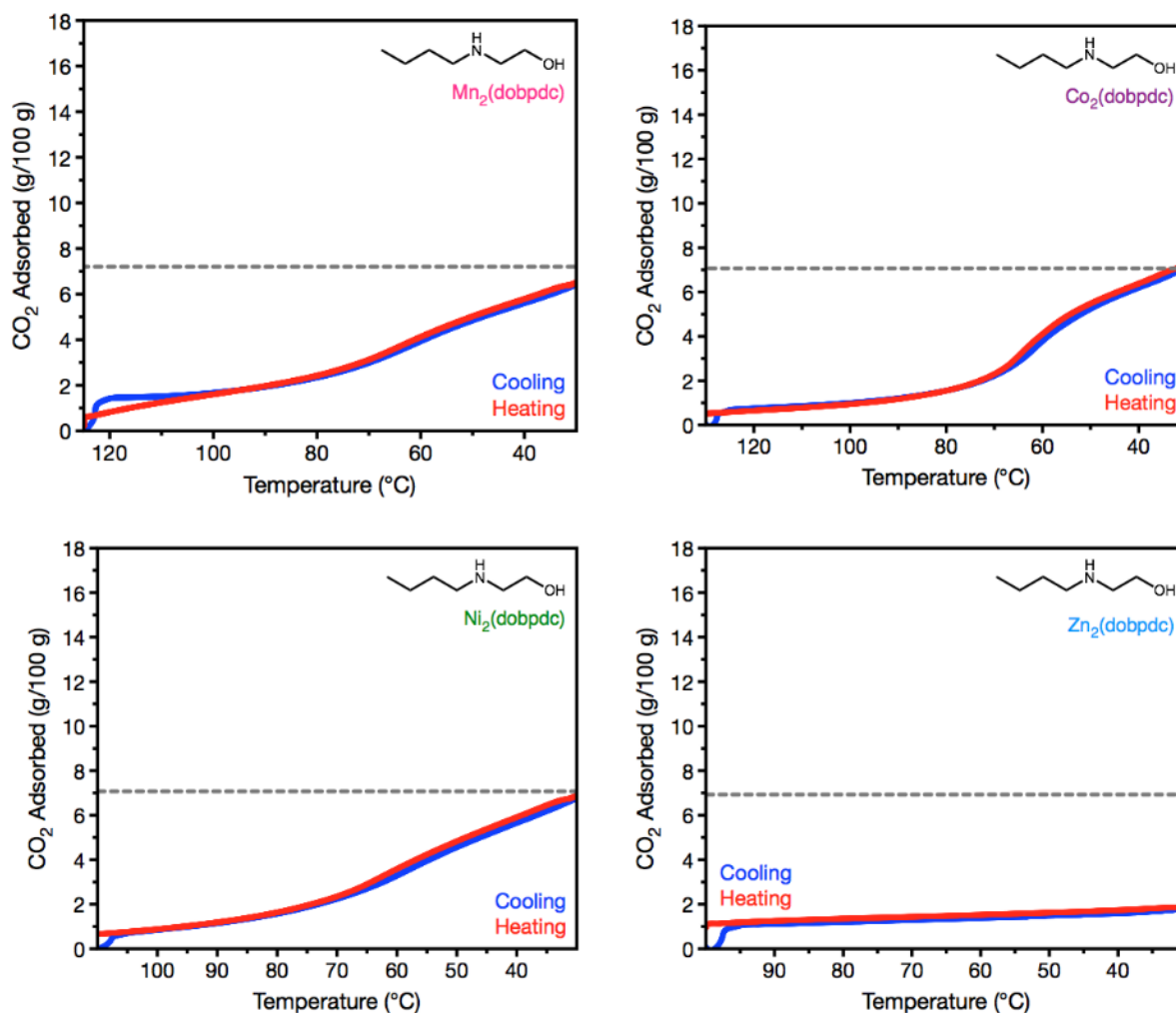# 8. Pure CO₂ adsorption/desorption isobars for alcoholamine- and alkoxyalkylamine-appended frameworks
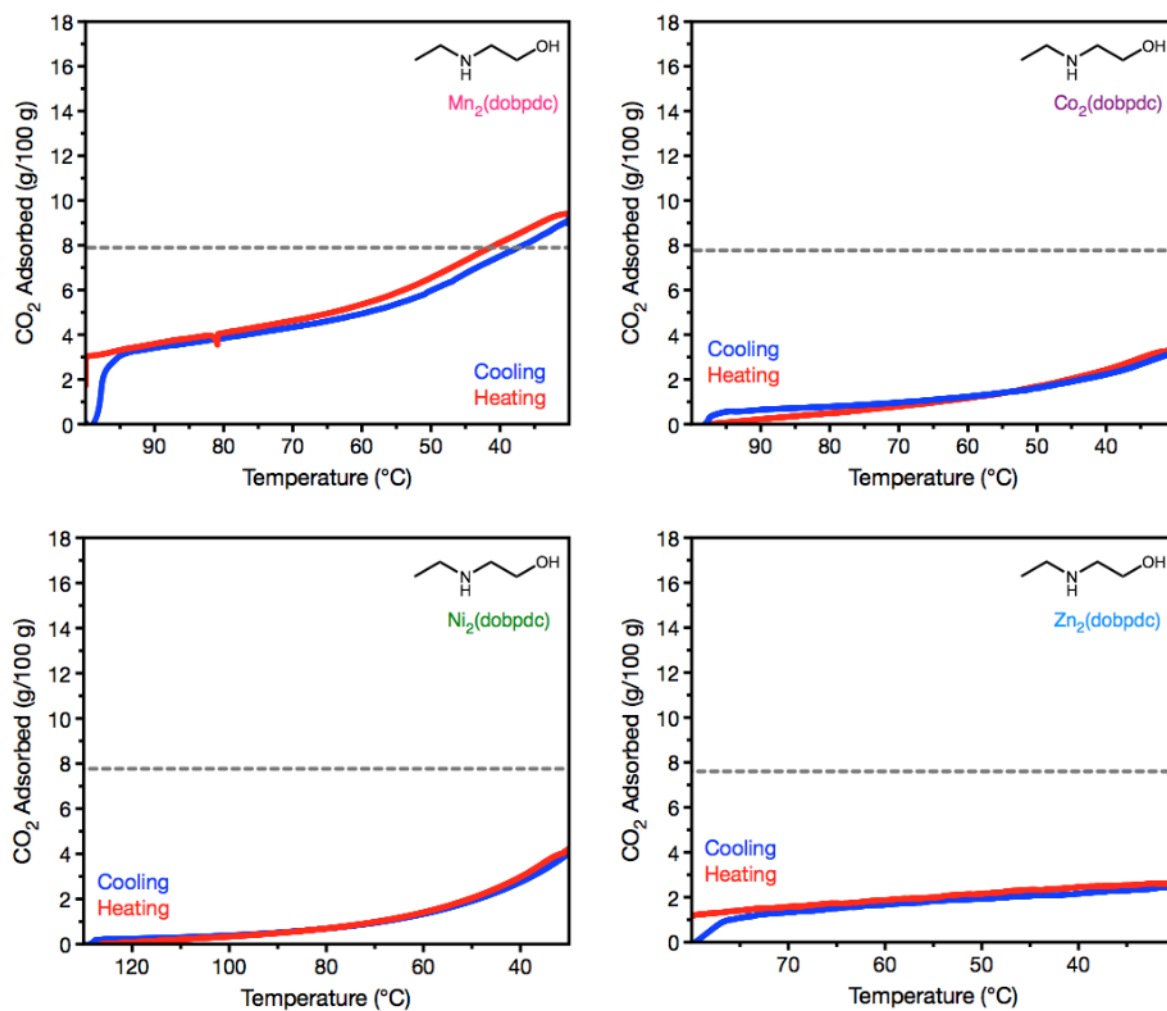
Figure S34. Pure CO₂ adsorption (blue) and desorption (red) isobars for e-2-OH–appended M₂(dobpdc). The dashed grey lines indicate theoretical loading (1 CO₂ per 2 alcoholamines).
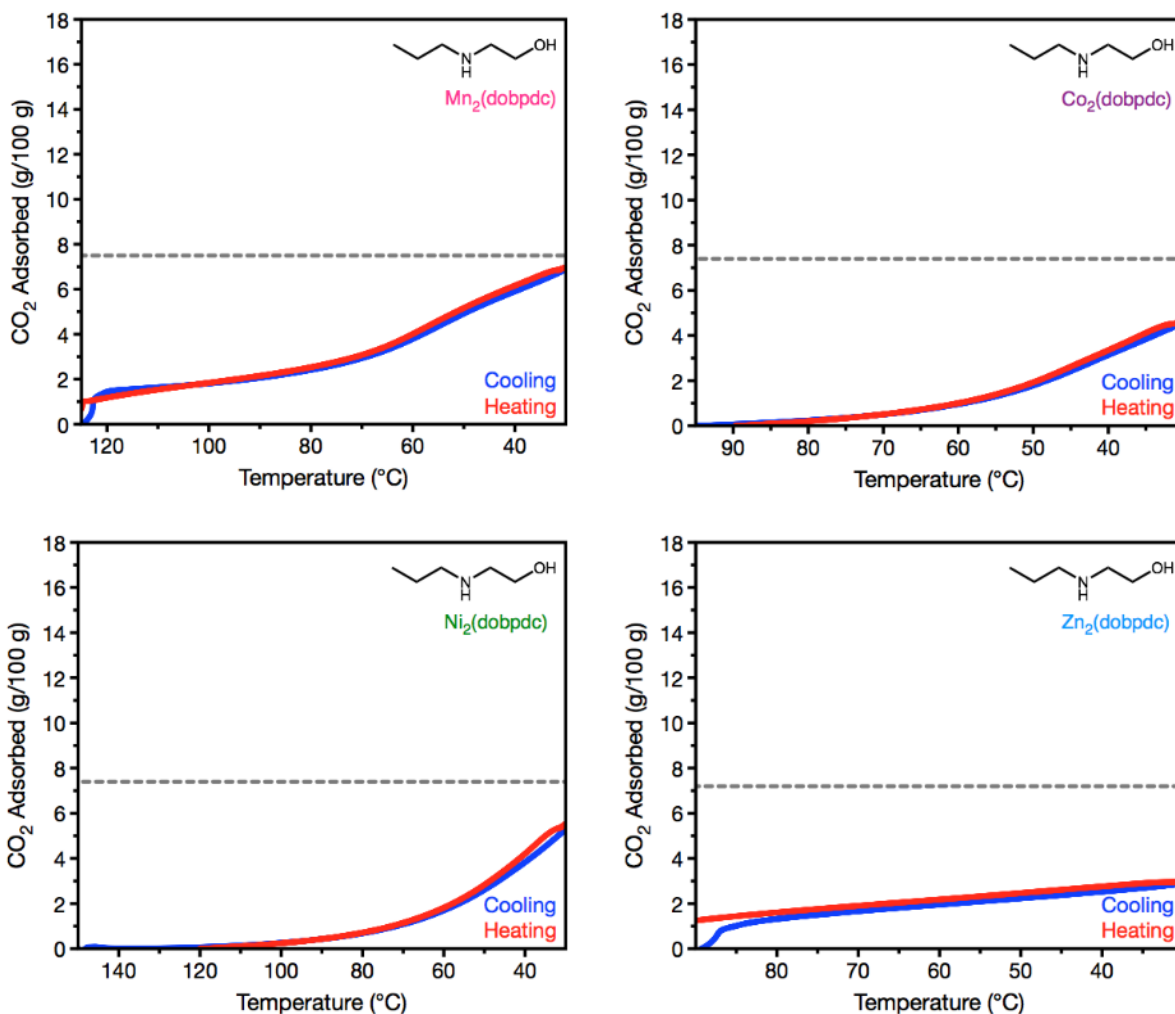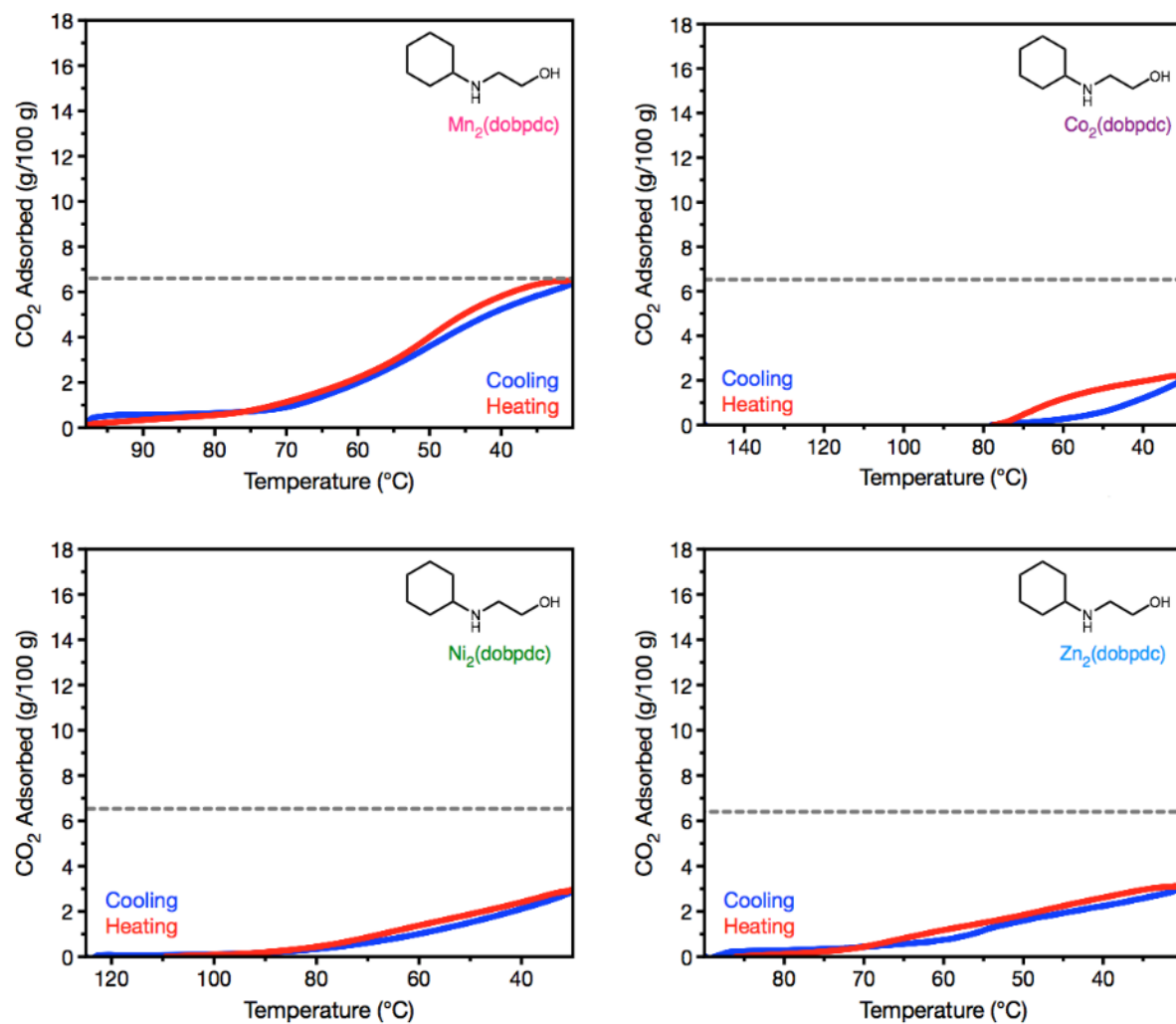
Figure S35. Pure CO_2 adsorption (blue) and desorption (red) isobars of nPr-2-OH–Mn_2(dobpdc) (top left), nPr-2-OH–Co_2(dobpdc) (top right), nPr-2-OH–Ni_2(dobpdc) (bottom left), and nPr-2-OH–Zn_2(dobpdc) (bottom right). The dashed grey line indicates theoretical loading (1 CO_2 per 2 alcoholamines).
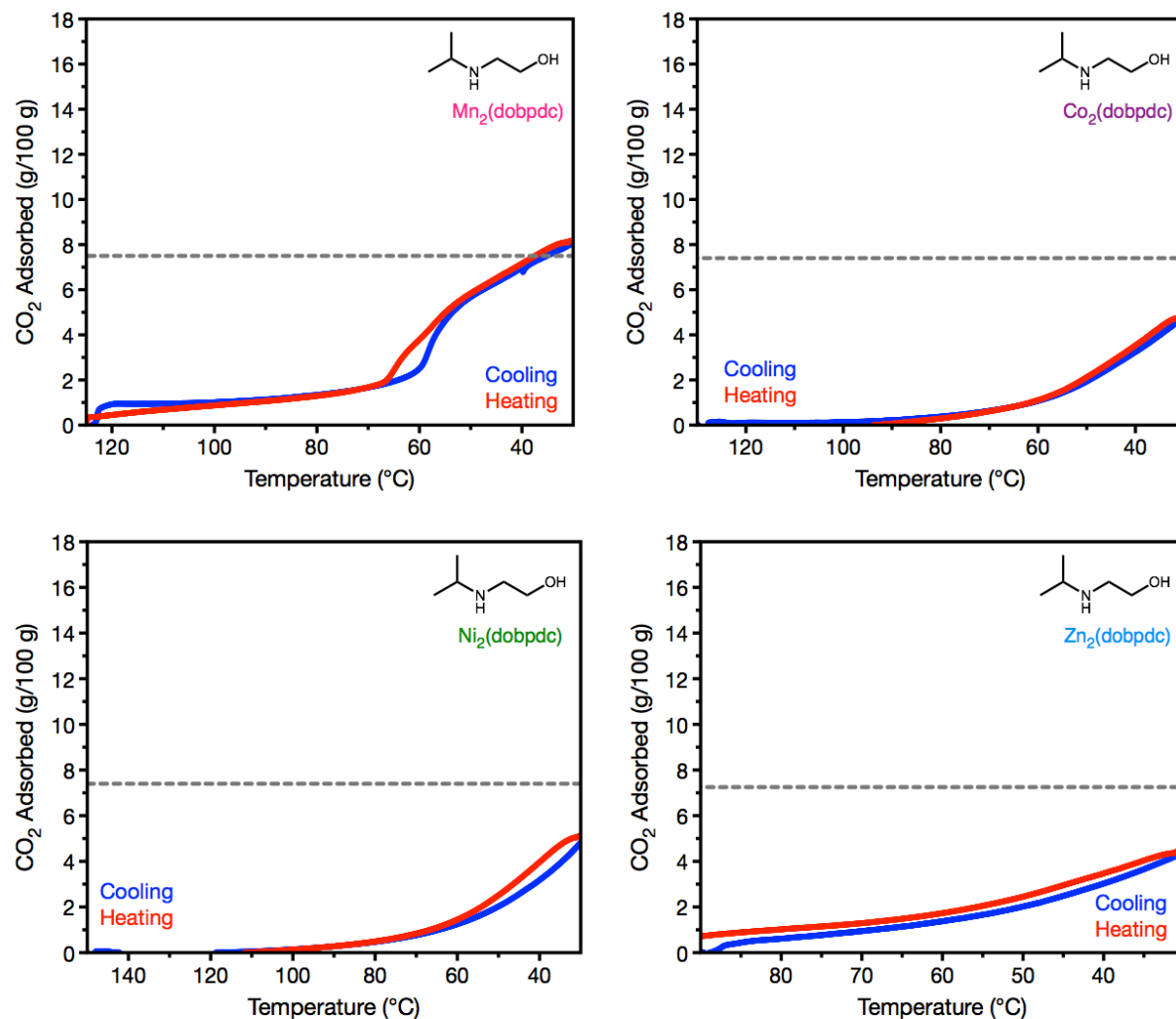
Figure S36. Pure CO_2 adsorption (blue) and desorption (red) isobars of iPr-2-OH–Mn_2(dobpdc) (top left), iPr-2-OH–Co_2(dobpdc) (top right), iPr-2-OH–Ni_2(dobpdc) (bottom left), and iPr-2-OH–Zn_2(dobpdc) (bottom right). The dashed grey line indicates theoretical loading (1 CO_2 per 2 alcoholamines). Note that iPr-2-OH–Mn_2(dobpdc) appears to show a step at approximately the same temperature of iPr-2-OH–Mg_2(dobpdc). Also, note that iPr-2-OH–Ni_2(dobpdc) has a low initial loading after appending, and hence the actual capacity and amount of CO_2 adsorbed may be higher than what is currently observed.
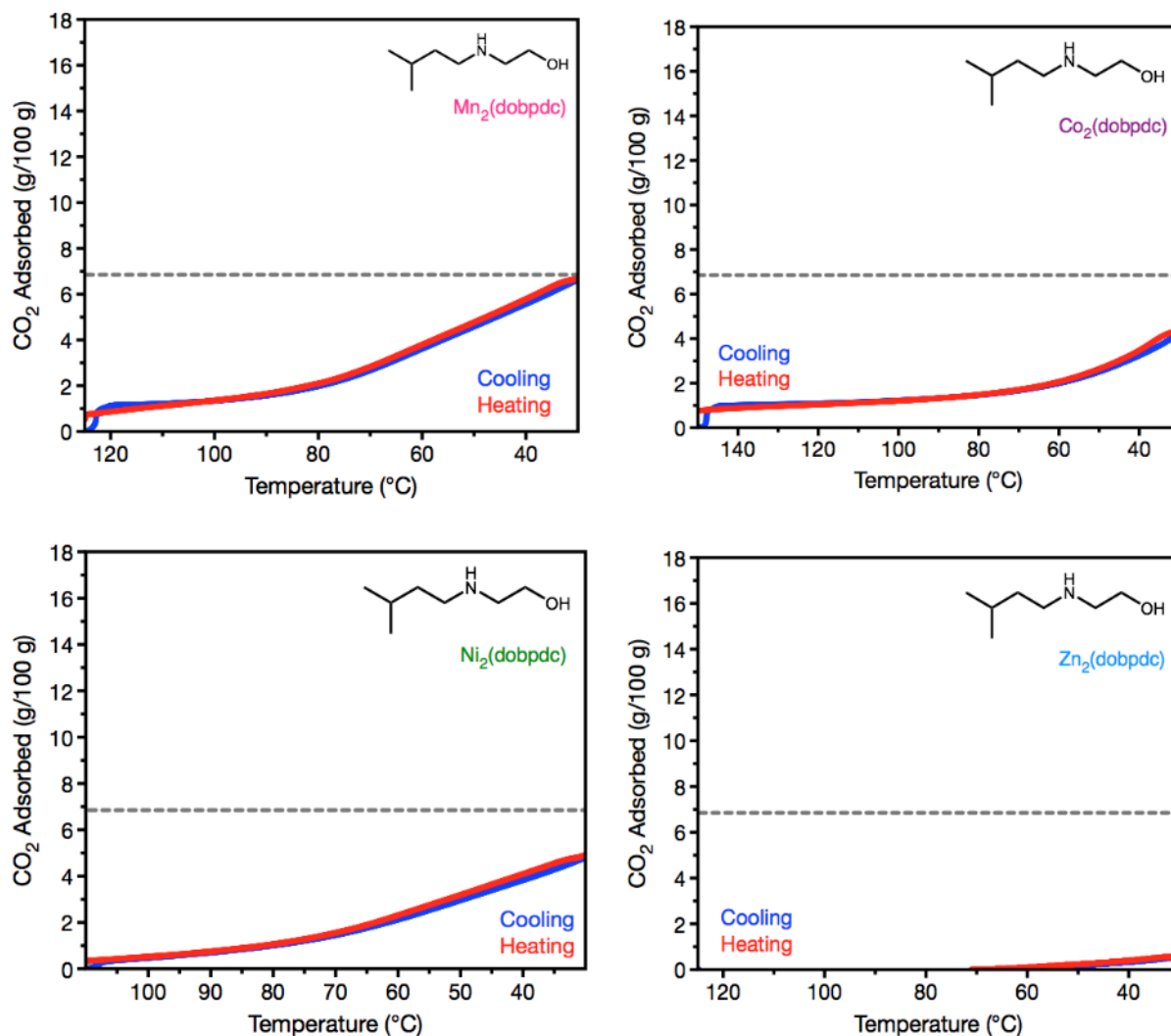
Figure S37. Pure CO_2 adsorption (blue) and desorption (red) isobars of nBu-2-OH–Mn$_2$(dobpdc) (top left), nBu-2-OH–Co$_2$(dobpdc) (top right), nBu-2-OH–Ni$_2$(dobpdc) (bottom left), and nBu-2-OH–Zn$_2$(dobpdc) (bottom right). The dashed grey line indicates theoretical loading (1 CO_2 per 2 alcoholamines).
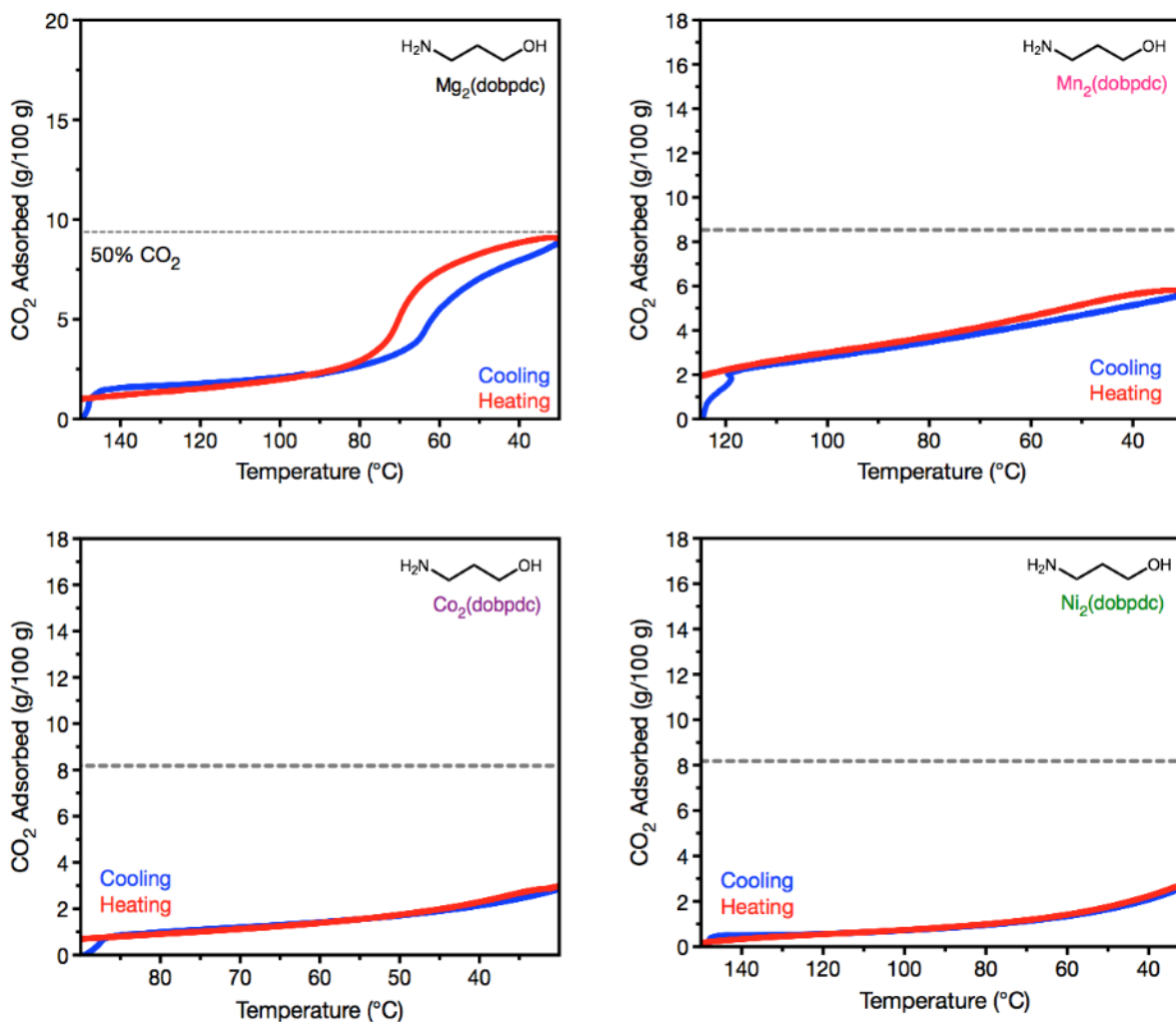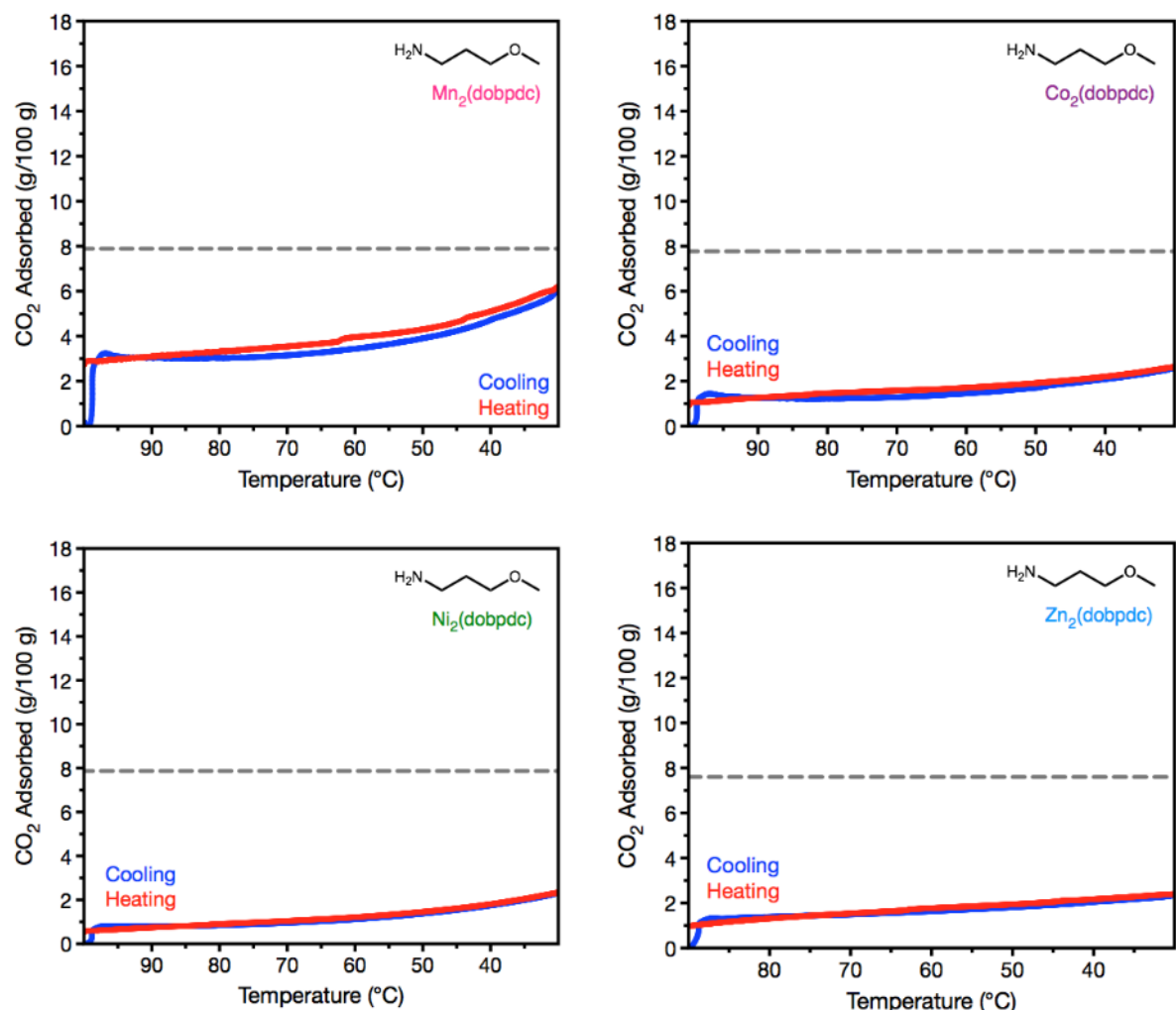
Figure S38. Pure CO_2 adsorption (blue) and desorption (red) isobars of cy-2-OH–Mn_2(dobpdc) (top left), cy-2-OH–Co_2(dobpdc) (top right), cy-2-OH–Ni_2(dobpdc) (bottom left), and cy-2-OH–Zn_2(dobpdc) (bottom right). The dashed grey line indicates theoretical loading (1 CO_2 per 2 alcoholamines).
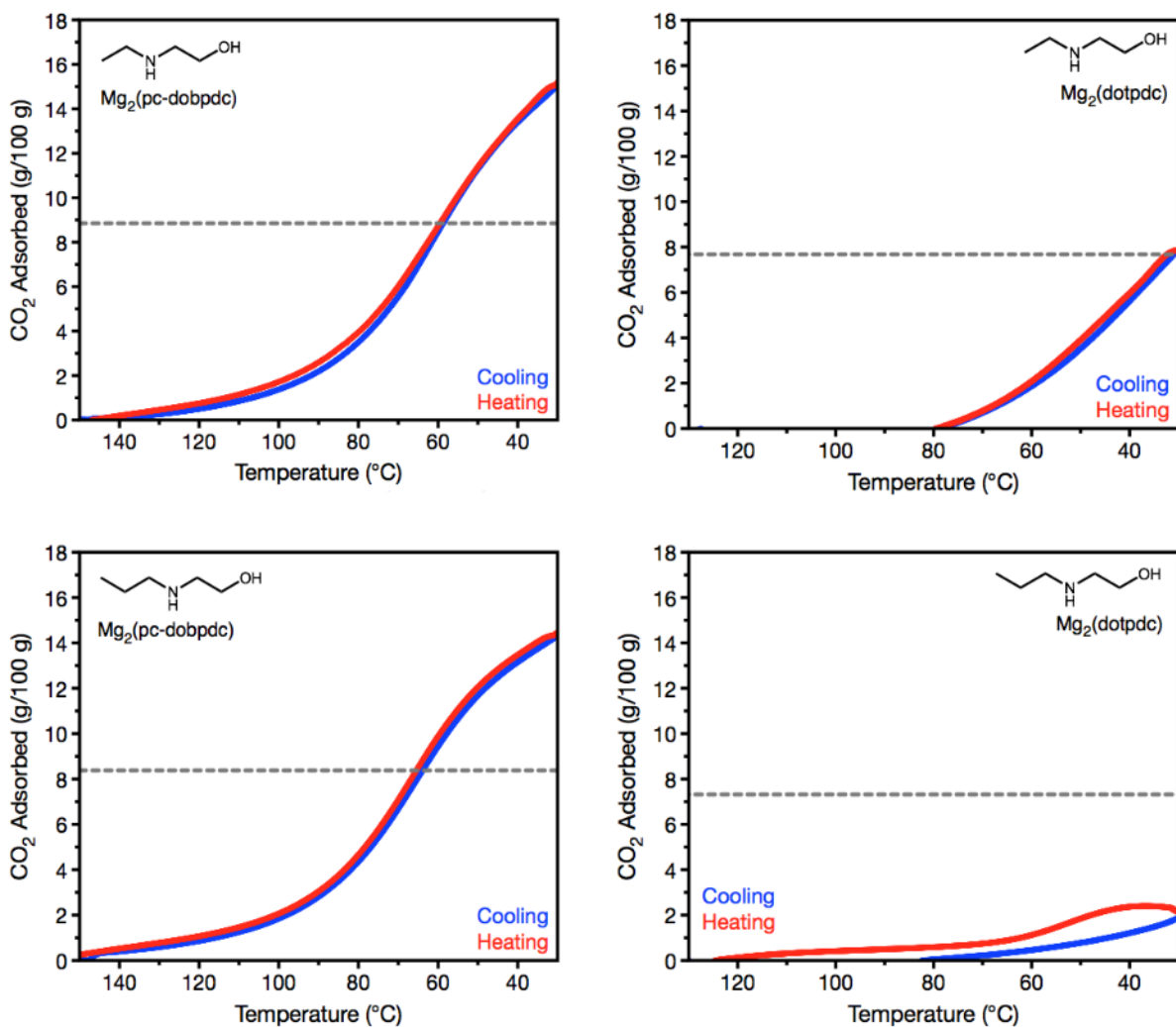
Figure S39. Pure CO_2 adsorption (blue) and desorption (red) isobars of iPent-2-OH–Mn_2(dobpdc) (top left), iPent-2-OH–Co_2(dobpdc) (top right), iPent-2-OH–Ni_2(dobpdc) (bottom left), and iPent-2-OH–Zn_2(dobpdc) (bottom right). The dashed grey line indicates theoretical loading (1 CO_2 per 2 alcoholamines). Also, note that iPent-2-OH–Co_2(dobpdc) and iPent-2-OH–Zn_2(dobpdc) have a relatively low initial loading after appending, and hence the actual capacity and amount of CO_2 adsorbed may be higher than what is currently observed.
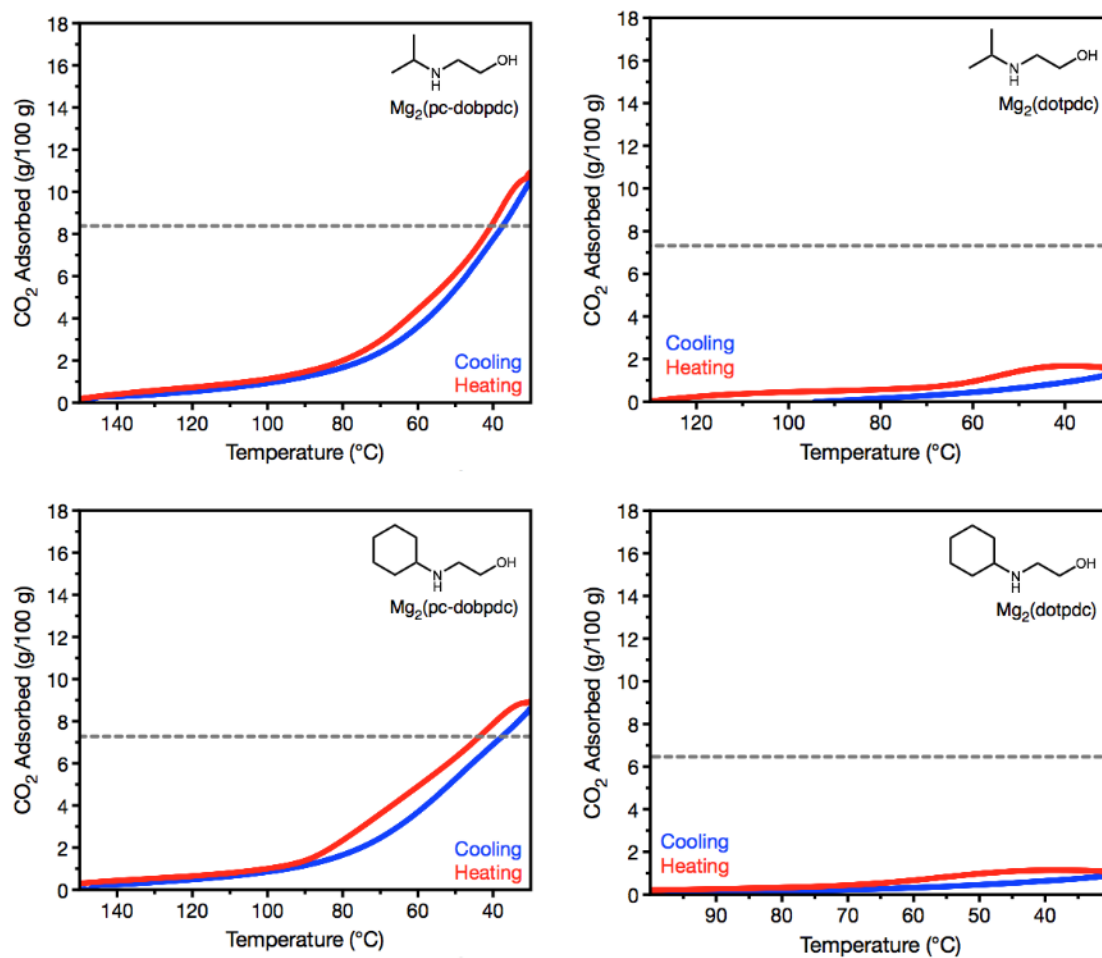
Figure S40. Pure CO_2 adsorption (blue) and desorption (red) isobars of 3-OH–Mg_2(dobpdc) (top left), 3-OH–Mn_2(dobpdc) (top right), 3-OH–Co_2(dobpdc) (bottom right), and 3-OH–Ni_2(dobpdc) (bottom right). The dashed grey line indicates theoretical loading (1 CO_2 per 2 alcoholamines). 3-OH–Zn_2(dobpdc) appeared to decompose and lose crystallinity by PXRD, and was thus not tested.
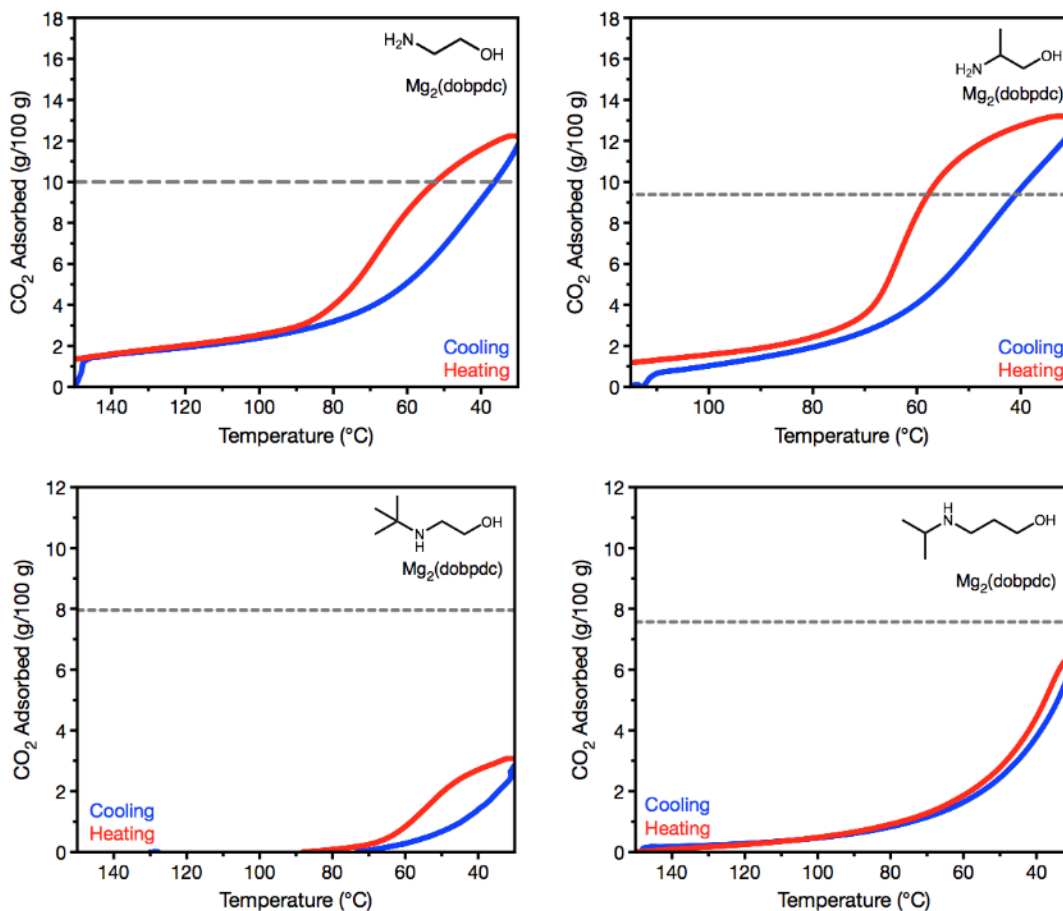
Figure S41. Pure CO_2 adsorption (blue) and desorption (red) isobars of 3-O-m–Mg_2(dobpdc) (top left), 3-O-m–Mn_2(dobpdc) (top right), 3-O-m–Co_2(dobpdc) (middle left), 3-O-m–Ni_2(dobpdc) (middle right), and 3-O-m–Zn_2(dobpdc) (bottom). The dashed grey line indicates theoretical loading (1 CO_2 per 2 alcoholamines).
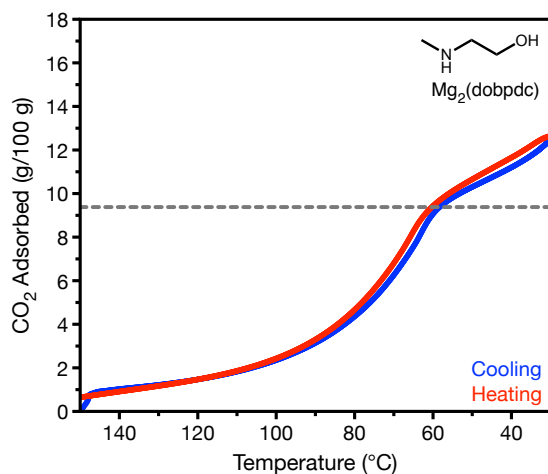
Figure S42. Pure CO_2 adsorption (blue) and desorption (red) isobars of e-2-OH–Mg_2(pc-dobpdc) (top left), e-2-OH–Mg_2(dotpdc) (top right), nPr-2-OH–Mg_2(pc-dobpdc) (bottom left), and nPr-2-OH–Mg_2(dotpdc) (right). The dashed grey line indicates theoretical loading (1 CO_2 per 2 alcoholamines).
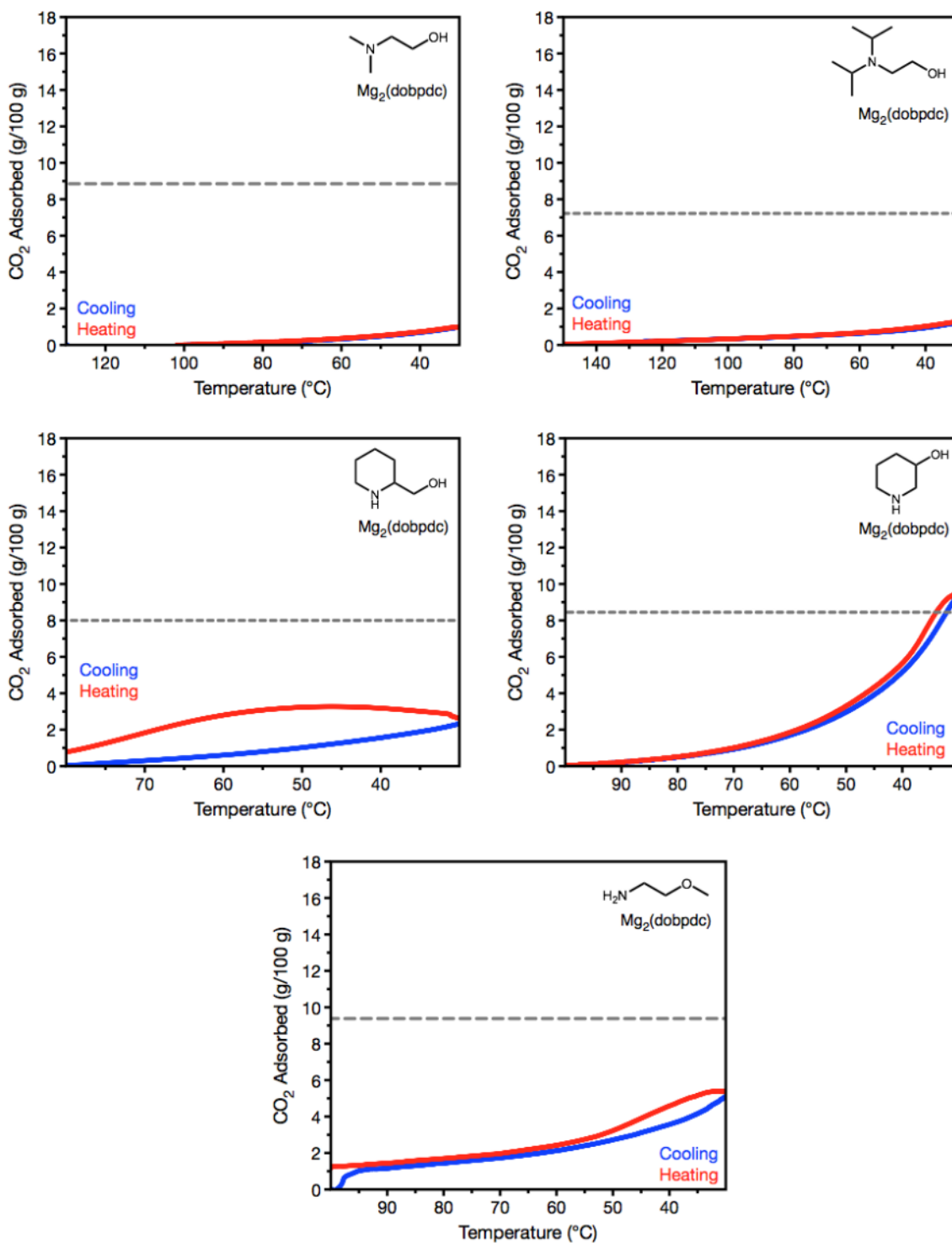
Figure S43. Pure CO_2 adsorption (blue) and desorption (red) isobars of iPr-2-OH–Mg_2(pc-dobpdc) (top left), iPr-2-OH–Mg_2(dotpdc) (top right), cy-2-OH–Mg_2(pc-dobpdc) (bottom left) and cy-2-OH–Mg_2(dotpdc) (right). The dashed grey line indicates theoretical loading (1 CO_2 per 2 alcoholamines). Also, note that cy-2-OH–Mg_2(pc-dobpdc) has a relatively low initial loading after appending, and hence the actual capacity and amount of CO_2 adsorbed may be higher than what is currently observed. The dashed grey line indicates theoretical loading (1 CO_2 per 2 alcoholamines).
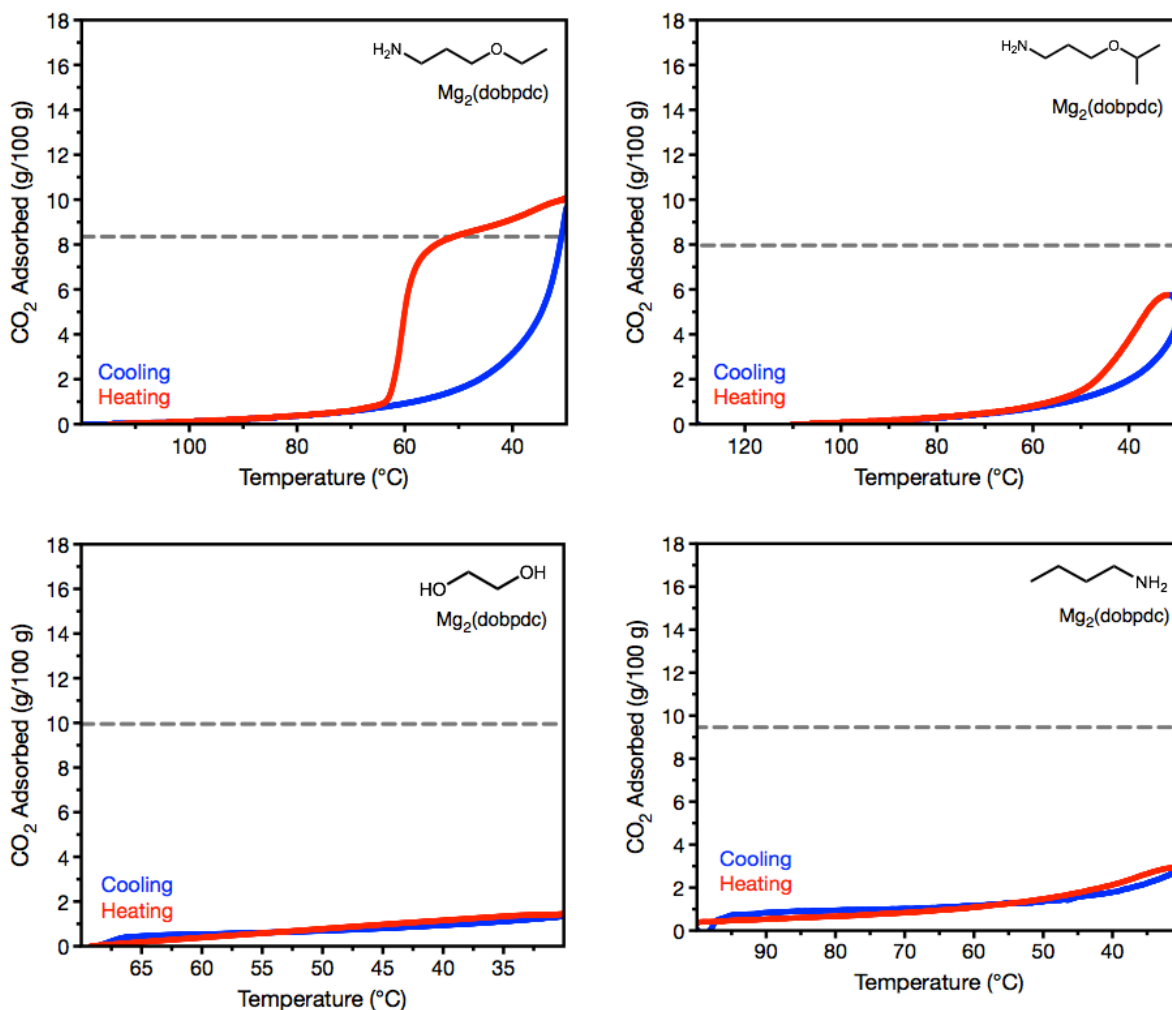
Figure S44. Pure CO_2 adsorption (blue) and desorption (red) isobars for Mg_2(dobpdc) appended with 2-OH (top left), 2a-OH (top right), tBu-2-OH (bottom left), and iPr-3-OH (bottom right). Dashed line indicates theoretical loading of 1 CO_2 per 2 alcoholamines.

Figure S45. Pure CO_2 adsorption (blue) and desorption (red) isobars of m-2-OH–Mg_2(dobpdc). The dashed grey line indicates theoretical loading (1 CO_2 per 2 alcoholamines). A clear transition in the adsorption and desorption profile at 50% loading indicates two different regimes of adsorption behavior.

Figure S46. Pure CO_2 adsorption (blue) and desorption (red) isobars of mm-2-OH–Mg_2(dobpdc) (top left), iPr,iPr-2-OH–Mg_2(dobpdc) (top right), pip-2-OH–Mg_2(dobpdc) (middle left), pip-2,OH–Mg_2(dobpdc) (middle right), and 2-O-m–Mg_2(dobpdc) (middle right)The dashed grey line indicates theoretical loading (1 CO_2 per 2 molecules).

Figure S47. Pure CO_2 adsorption (blue) and desorption (red) isobars of 3-O-e–Mg_2(dobpdc) (top left), 3-O-iPr–Mg_2(dobpdc) (top right), OH-2-OH–Mg_2(dobpdc) (bottom left), and nBu–Mg_2(dobpdc) (bottom right). The dashed grey line indicates theoretical loading (1 CO_2 per 2 molecules). Note absence of adsorption upon utilizing no amines.

## 9. Decomposition of alcoholamine- and alkoxyalkylamine-appended frameworks
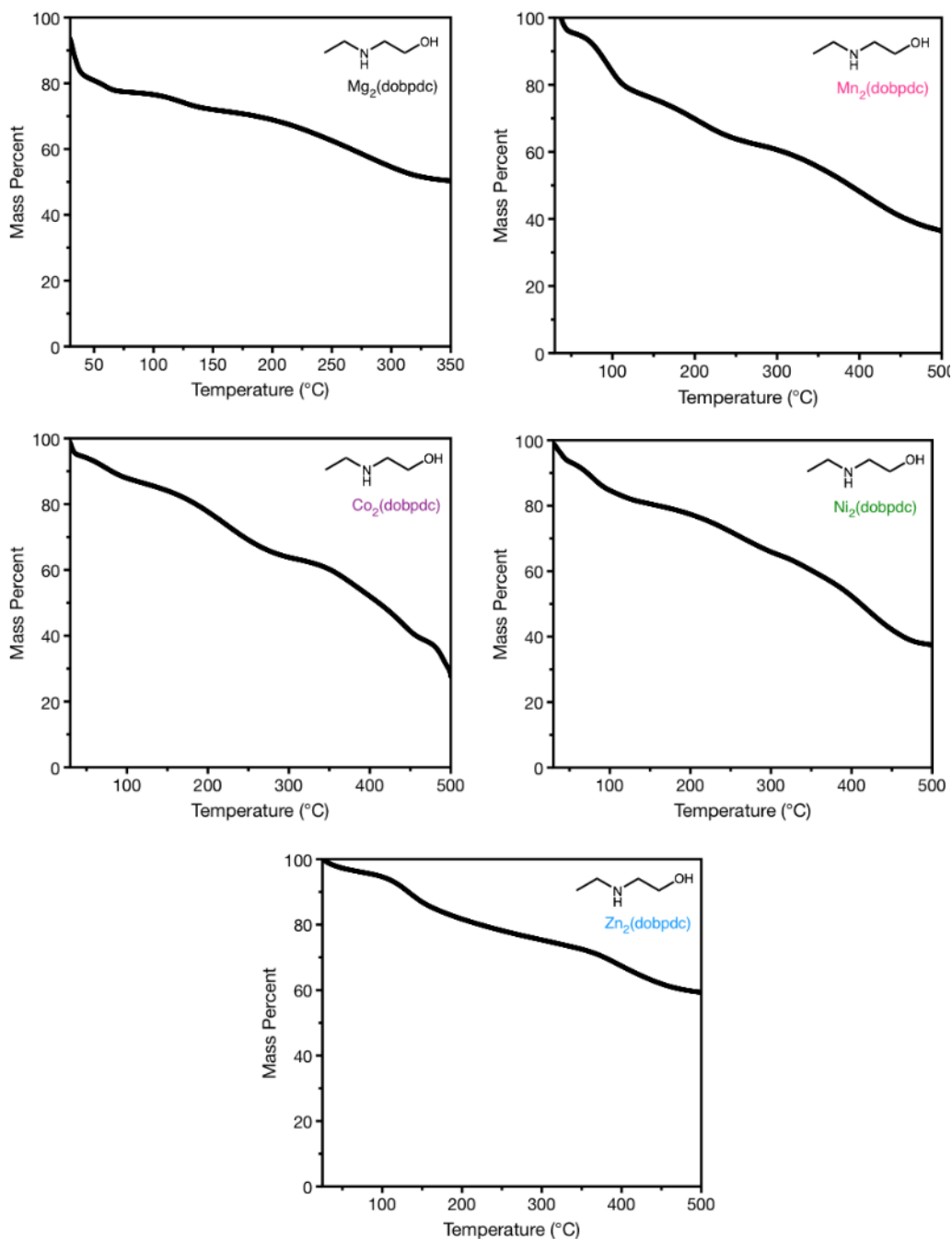
Figure S48. N$_2$ decomposition profiles of e-2-OH–Mg$_2$(dobpdc) (top left), e-2-OH–Mn$_2$(dobpdc) (top right), e-2-OH–Co$_2$(dobpdc) (middle left), e-2-OH–Ni$_2$(dobpdc) (middle right), and e-2-OH–Zn$_2$(dobpdc) (bottom).
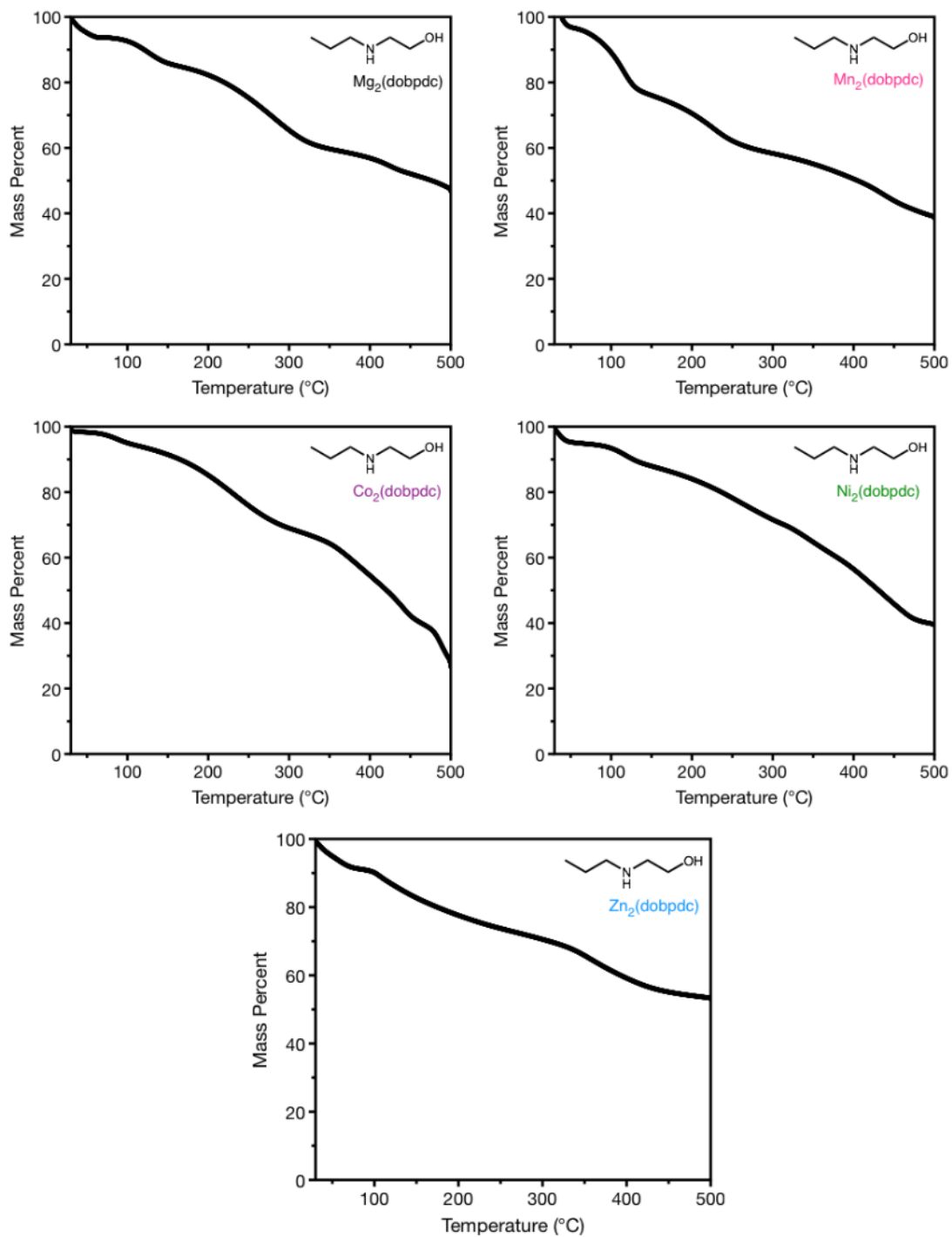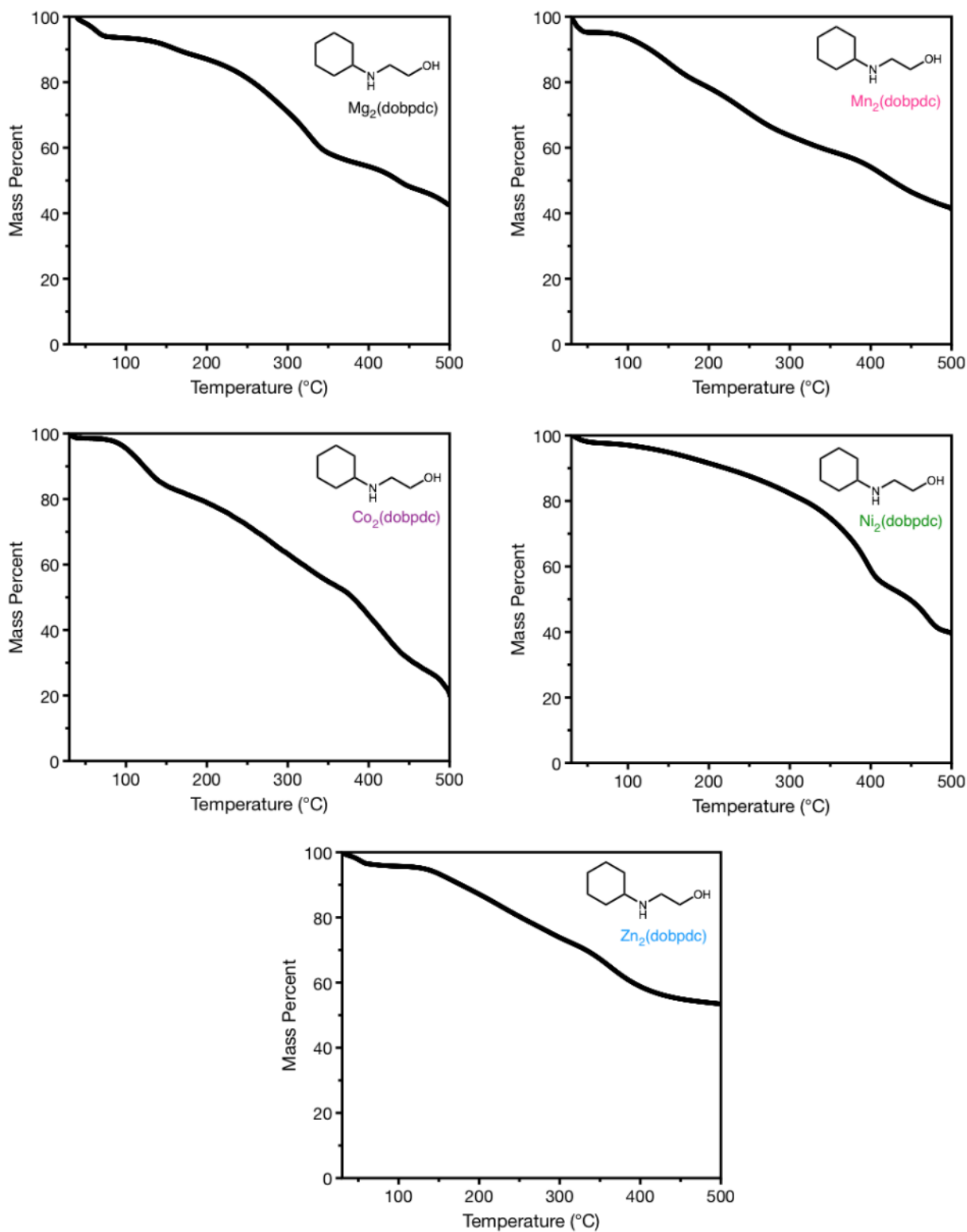
Figure S49. N_2 decomposition profiles of nPr-2-OH–Mg_2(dobpdc) (top left), nPr-2-OH–Mn_2(dobpdc) (top right), nPr-2-OH–Co_2(dobpdc) (middle left), nPr-2-OH–Ni_2(dobpdc) (middle right), and nPr-2-OH–Zn_2(dobpdc) (bottom).
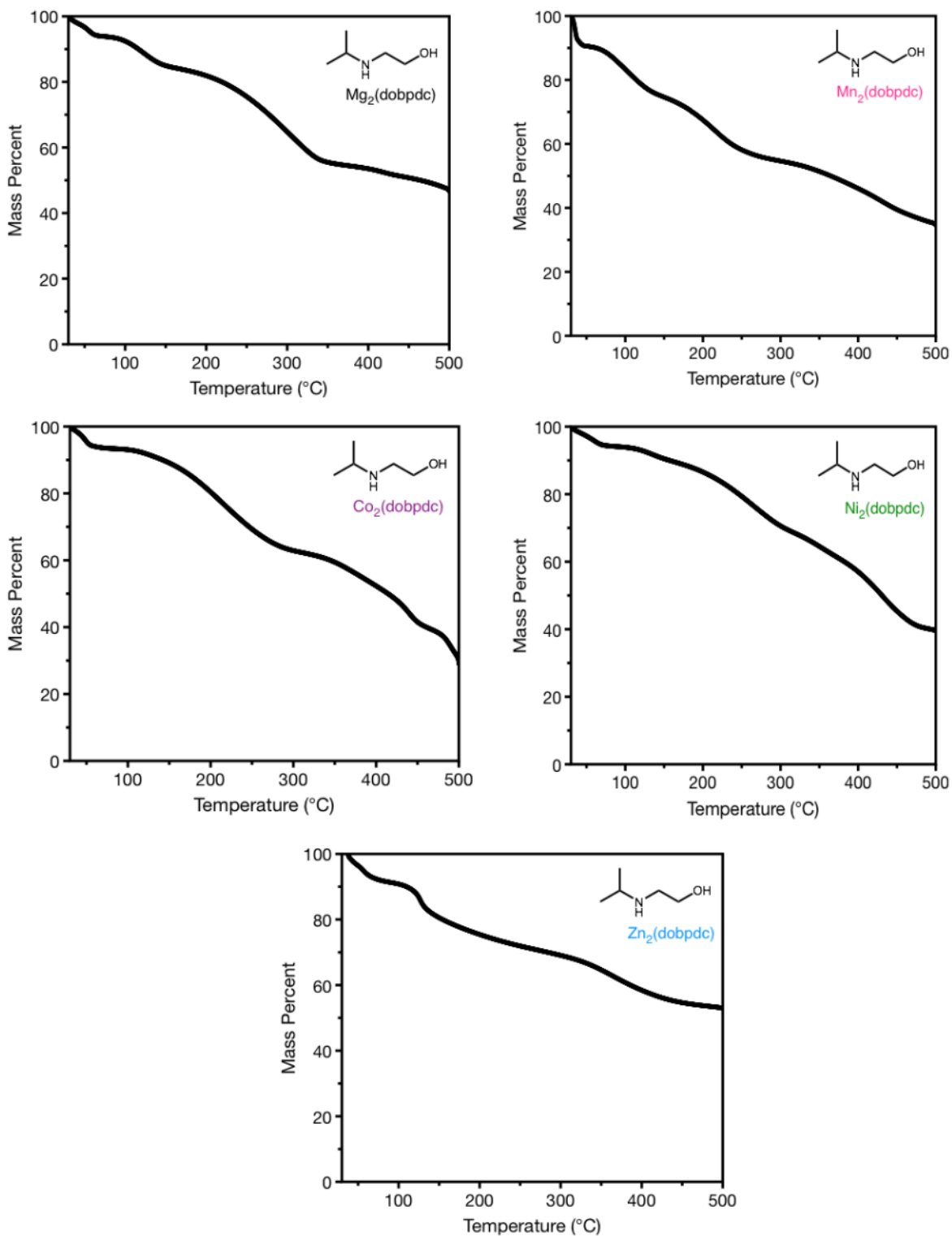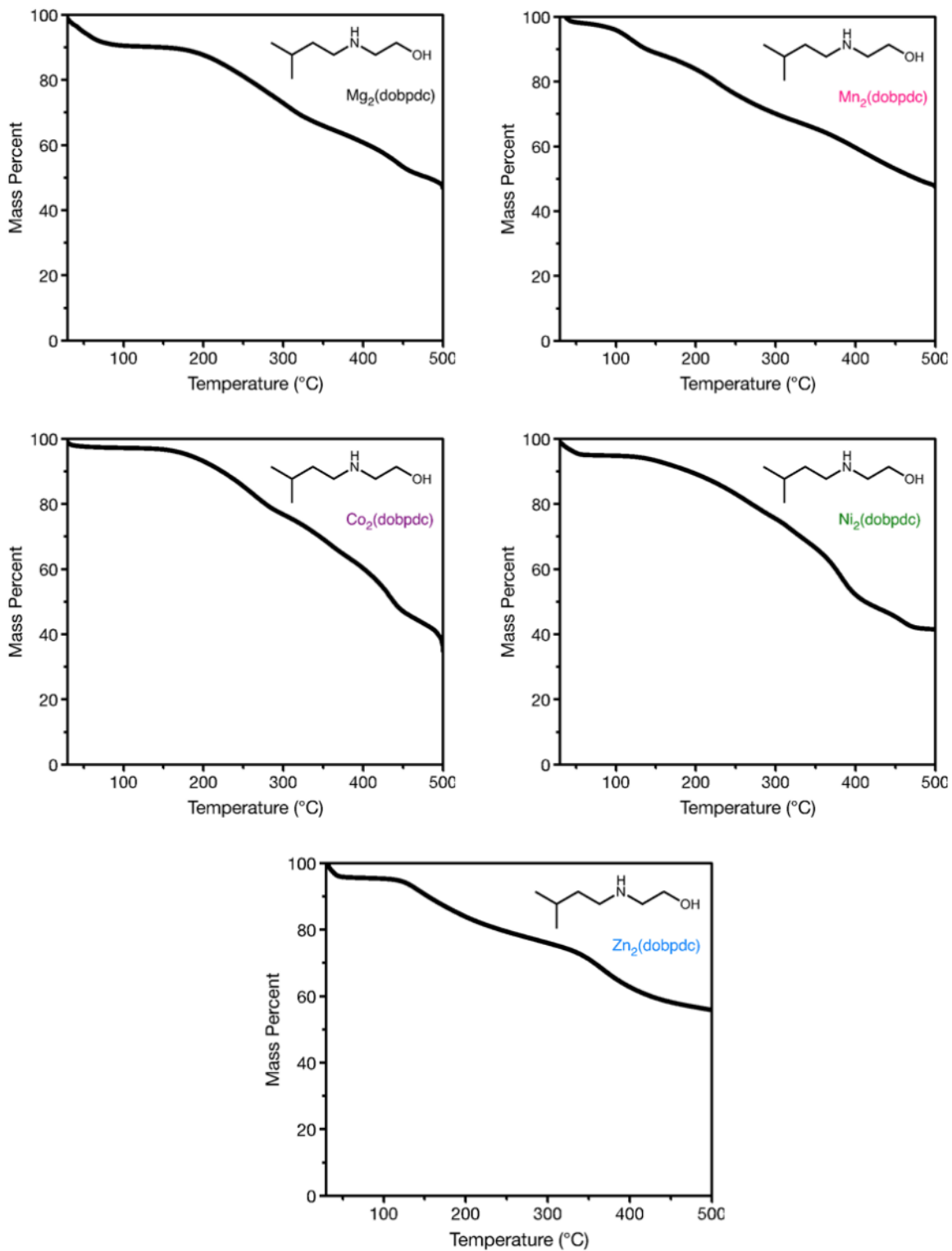
Figure S50. N_2 decomposition profiles of iPr-2-OH–Mg_2(dobpdc) (top left), iPr-2-OH–Mn_2(dobpdc) (top right), iPr-2-OH–Co_2(dobpdc) (middle left), iPr-2-OH–Ni_2(dobpdc) (middle right), and iPr-2-OH–Zn_2(dobpdc) (bottom).
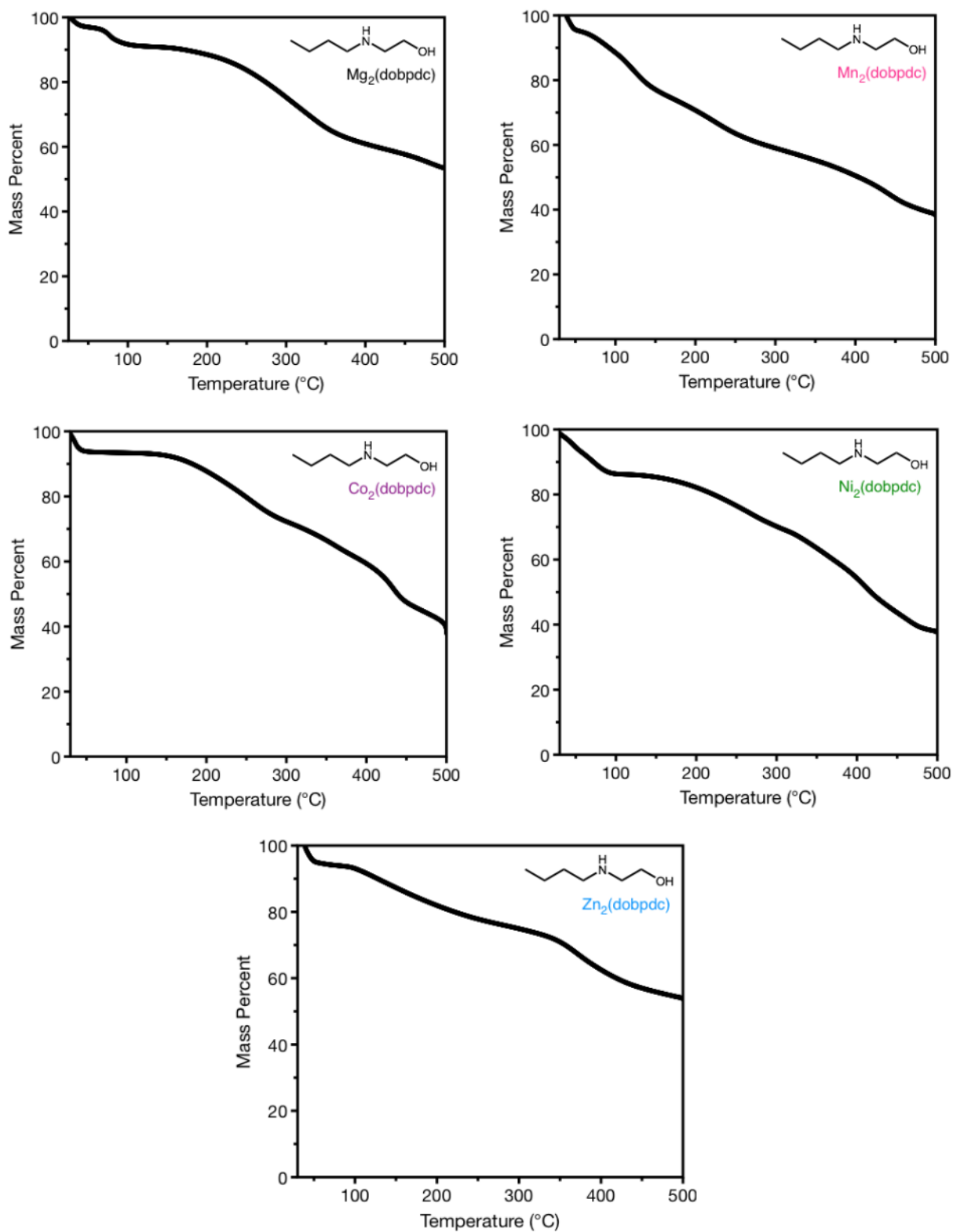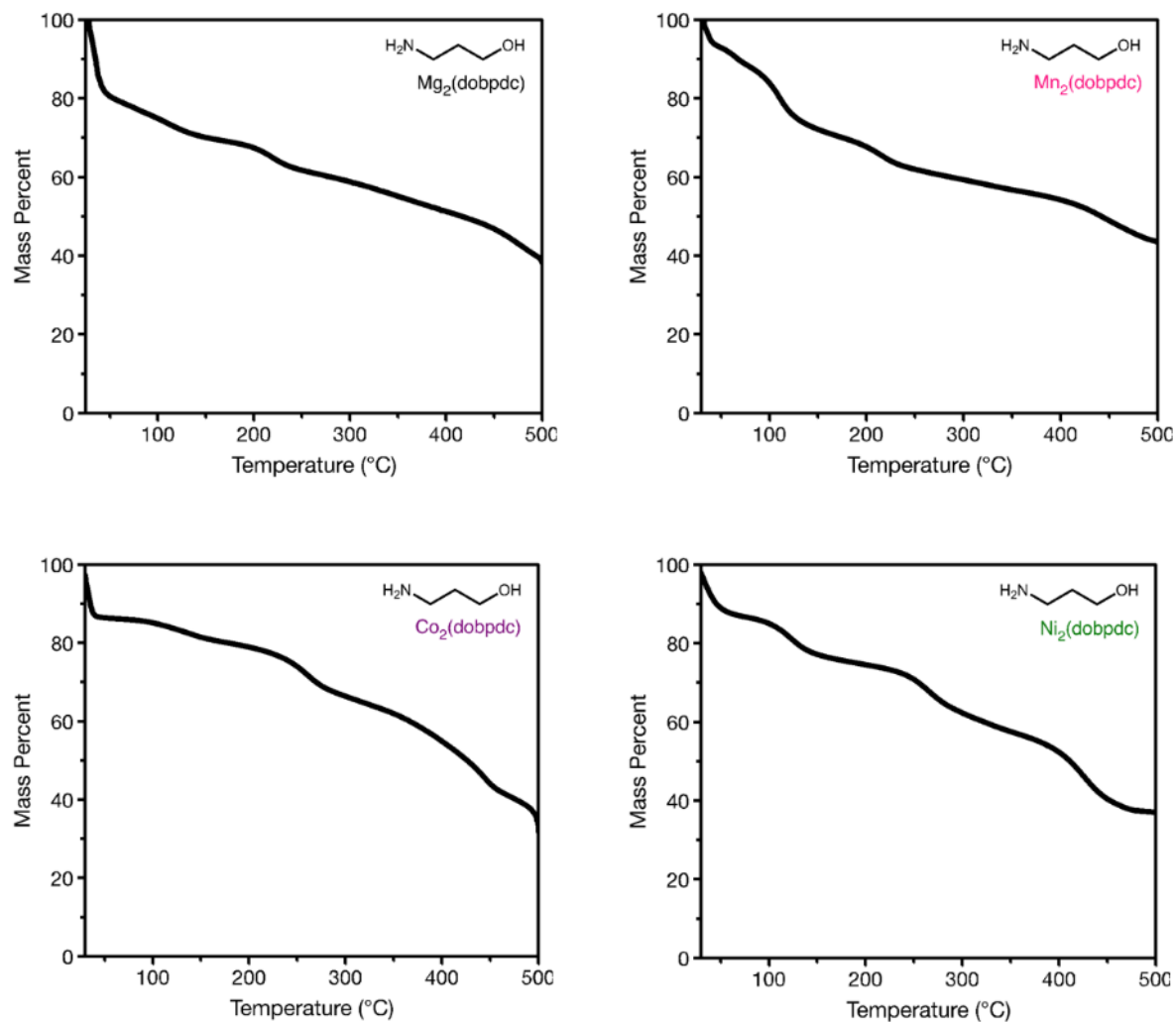
Figure S51. N_2 decomposition profiles of nBu-2-OH–Mg_2(dobpdc) (top left), nBu-2-OH–Mn_2(dobpdc) (top right), nBu-2-OH–Co_2(dobpdc) (middle left), nBu-2-OH–Ni_2(dobpdc) (middle right), and nBu-2-OH–Zn_2(dobpdc) (bottom).
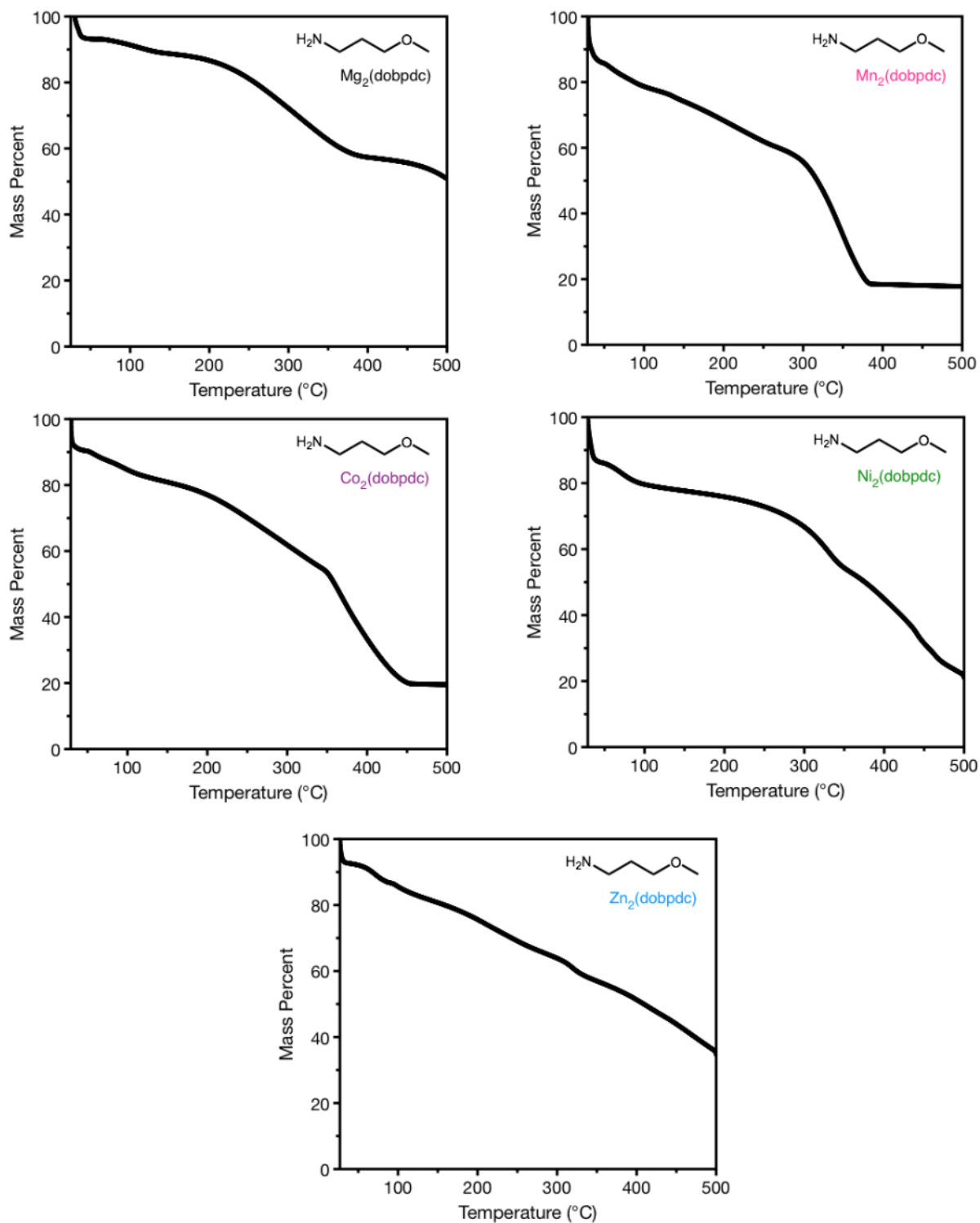
Figure S52. N$_2$ decomposition profiles of cy-2-OH–Mg$_2$(dobpdc) (top left), cy-2-OH–Mn$_2$(dobpdc) (top right), cy-2-OH–Co$_2$(dobpdc) (middle left), cy-2-OH–Ni$_2$(dobpdc) (middle right), and cy-2-OH–Zn$_2$(dobpdc) (bottom).

Figure S53. N$_2$ decomposition profiles of iPent-2-OH–Mg$_2$(dobpdc) (top left), iPent-2-OH–Mn$_2$(dobpdc) (top right), iPent-2-OH–Co$_2$(dobpdc) (middle left), iPent-2-OH–Ni$_2$(dobpdc) (middle right), and iPent-2-OH–Zn$_2$(dobpdc) (bottom).
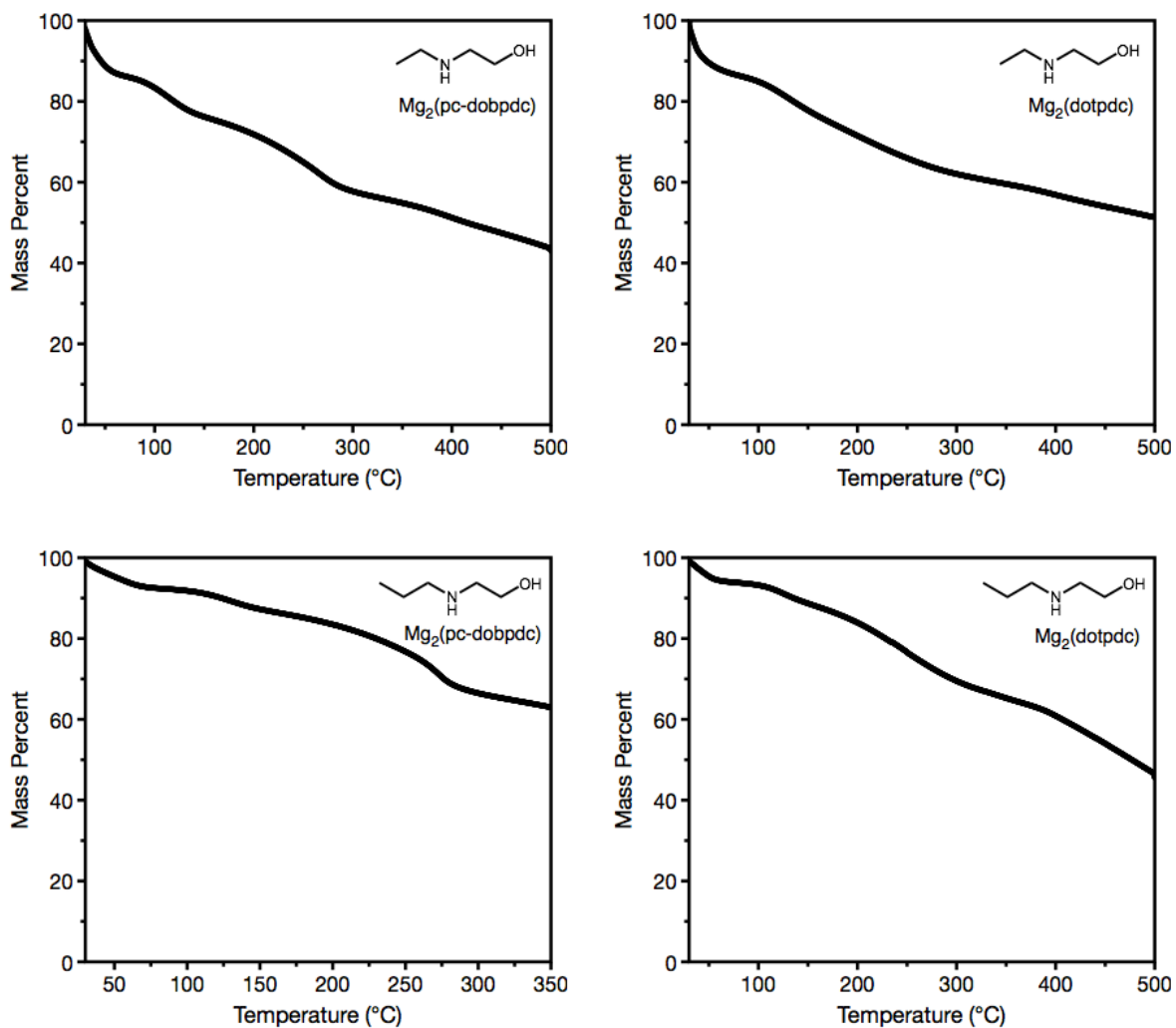
Figure S54. N_2 decomposition profiles of 3-OH–Mg_2(dobpdc) (top left), 3-OH–Mn_2(dobpdc) (top right), 3-OH–Co_2(dobpdc) (bottom left), and 3-OH–Ni_2(dobpdc) (bottom right). Note that 3-OH–Zn_2(dobpdc) appeared to decompose and lose crystallinity by PXRD.
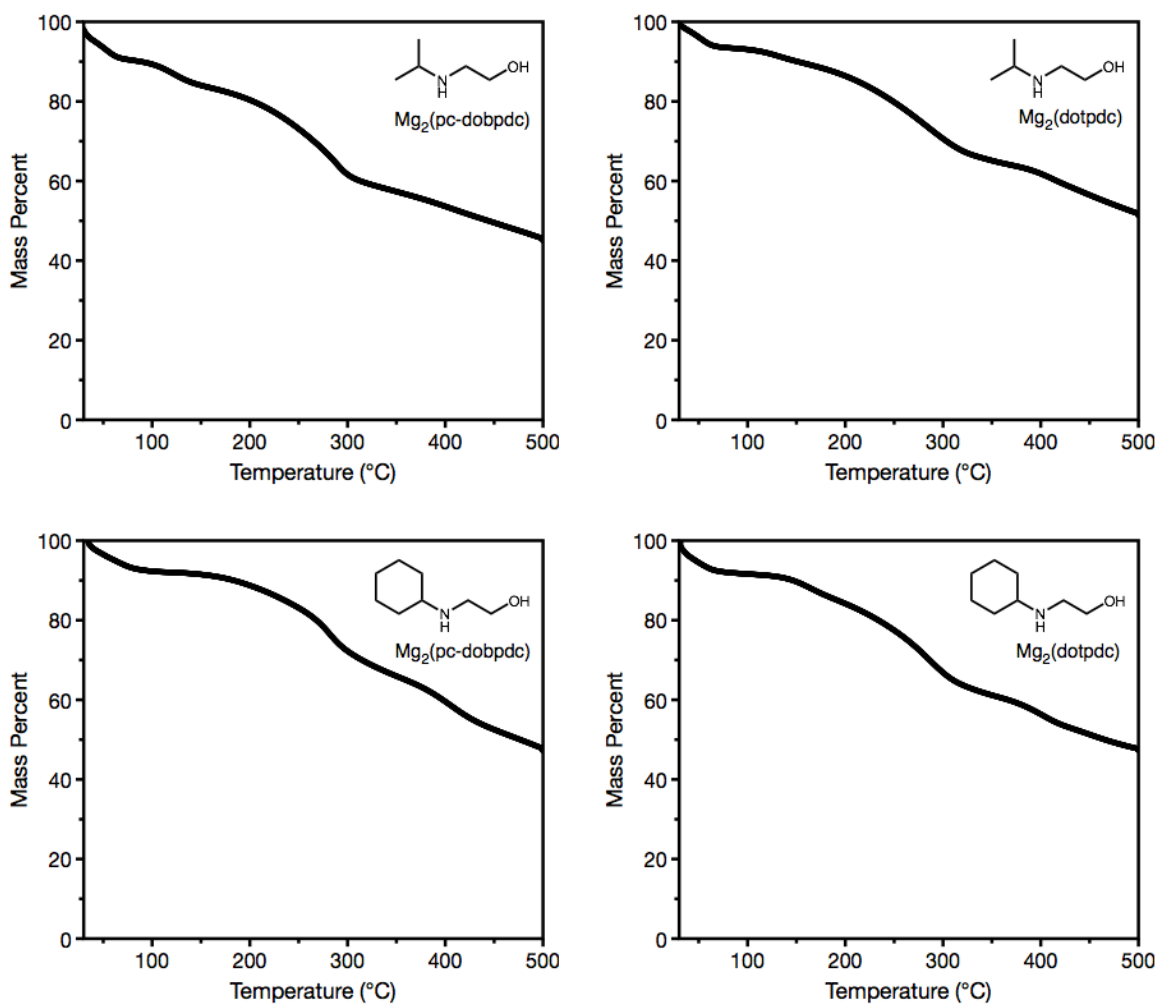
Figure S55. N_2 decomposition profiles of 3-O-m-OH–Mg_2(dobpdc) (top left), 3-O-m–Mn_2(dobpdc) (top right), 3-O-m–Co_2(dobpdc) (middle left), 3-O-m–Ni_2(dobpdc) (middle right), and 3-O-m–Zn_2(dobpdc) (bottom).
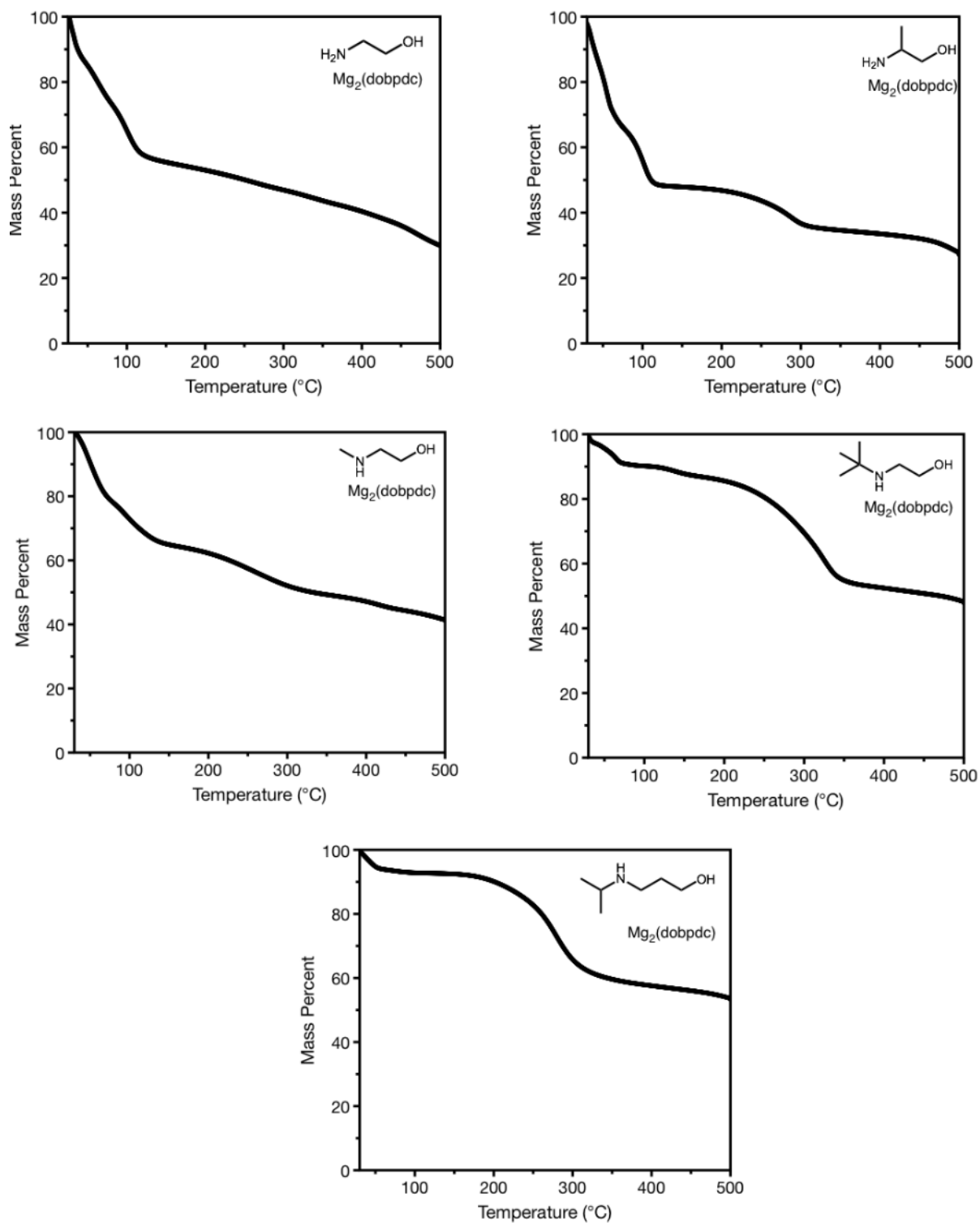
Figure S56. N$_2$ decomposition profiles of e-2-OH–Mg$_2$(pc-dobpdc) (top left), e-2-OH–Mg$_2$(dotpdc) (top right), nPr-2-OH–Mg$_2$(pc-dobpdc) (bottom left), and nPr-2-OH–Mg$_2$(dotpdc) (bottom right).

Figure S57. N_2 decomposition profiles of iPr-2-OH–Mg_2(pc-dobpdc) (top left), iPr-2-OH–Mg_2(dotpdc) (top right), cy-2-OH–Mg_2(pc-dobpdc) (bottom left), and cy-2-OH–Mg_2(dotpdc) (bottom right).

Figure S58. N$_2$ decomposition profiles of 2-OH–Mg$_2$(dobpdc) (top left), 2a-OH–Mg$_2$(dobpdc) (top right), m-2-OH–Mg$_2$(dobpdc) (middle left), tBu-2-OH–Mg$_2$(dobpdc) (middle right), and iPr-3-OH–Mg$_2$(dobpdc) (bottom).
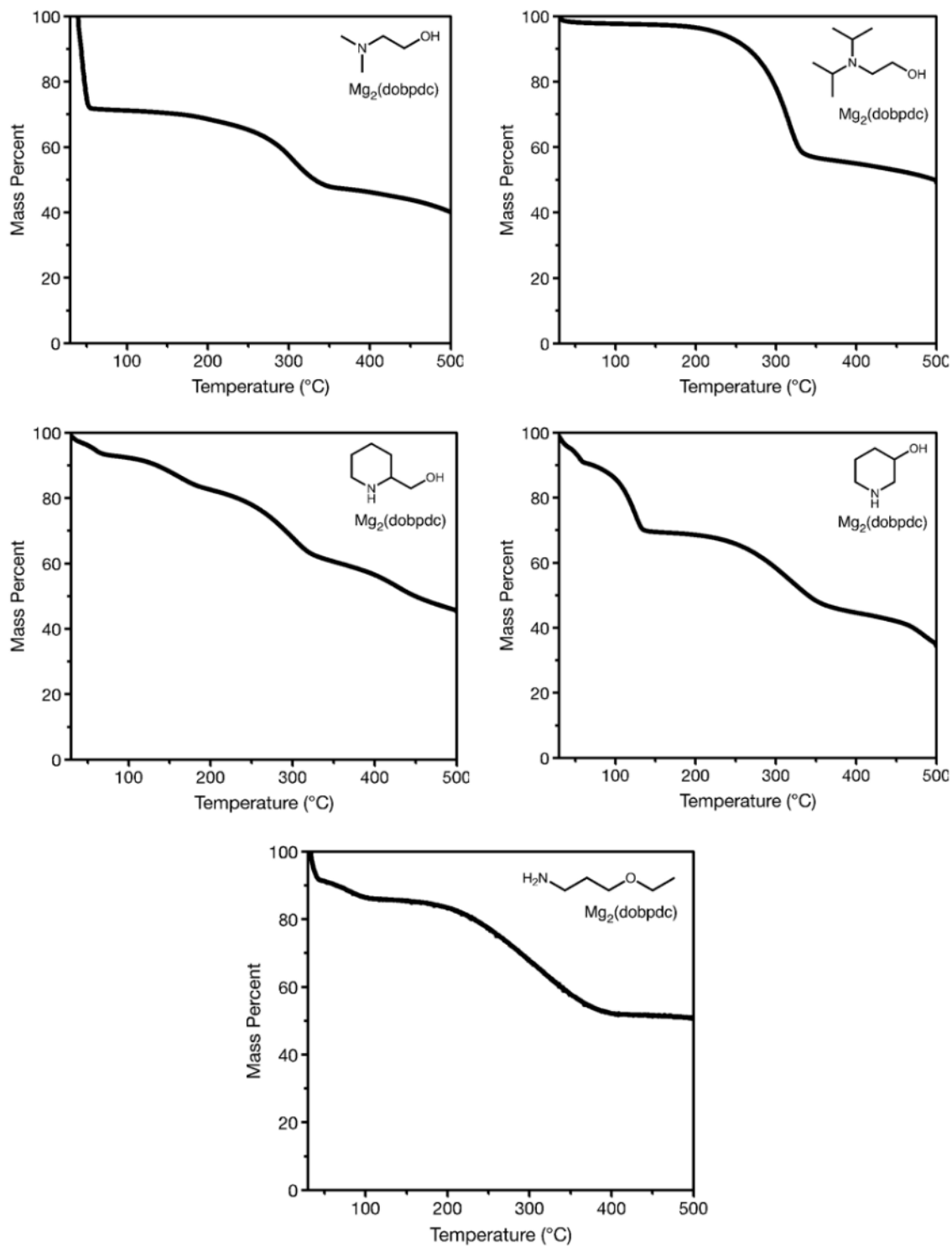
Figure S59. N_2 decomposition profiles of mm-2-OH–Mg_2(dobpdc) (top left), iPr,iPr-2-OH–Mg_2(dobpdc) (top right), pip-2-OH–Mg_2(dobpdc) (middle left), pip-2,OH–Mg_2(dobpdc) (middle right), and 3-O-e–Mg_2(dobpdc) (bottom).
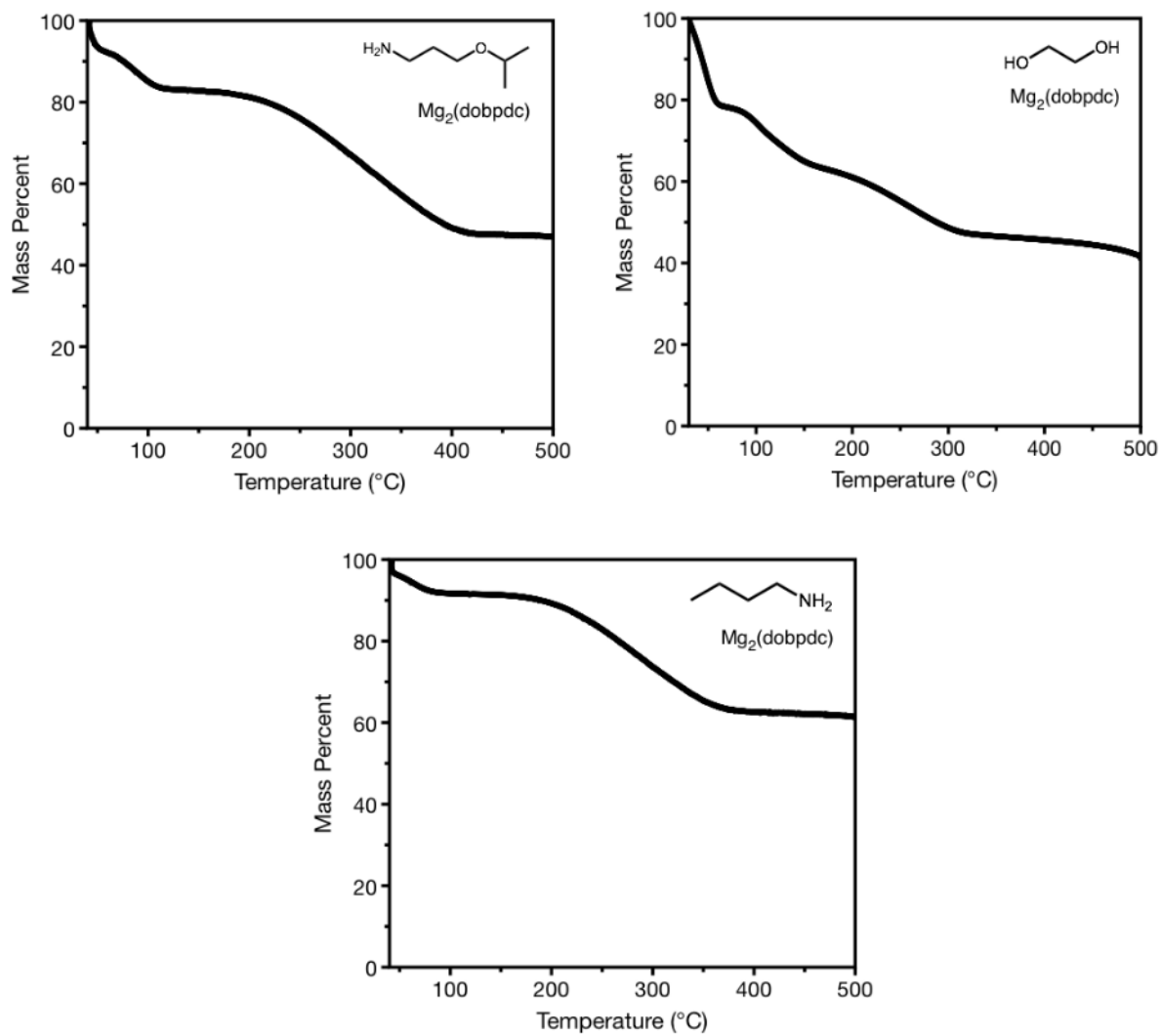
Figure S60. N$_2$ decomposition profiles of 3-O-iPr–Mg$_2$(dobpdc) (top left), OH-2-OH–Mg$_2$(dobpdc) (top right), and nBu–Mg$_2$(dobpdc) (bottom).
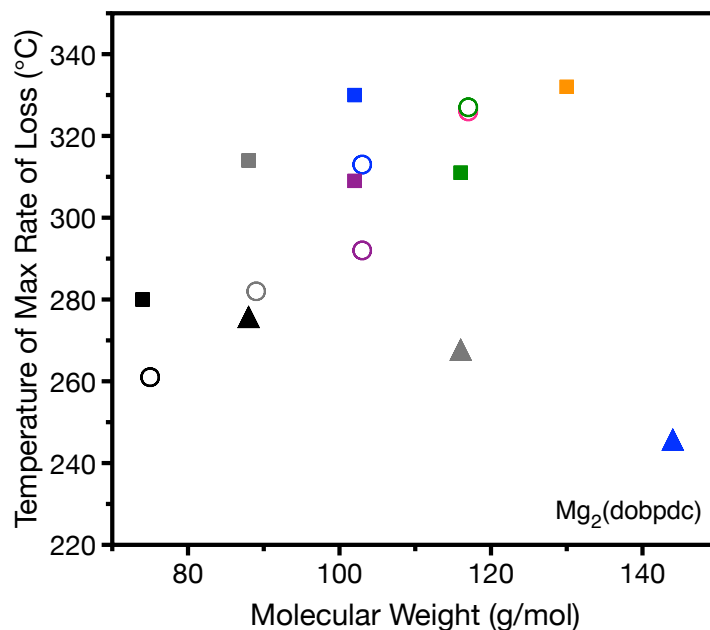
Figure S61. Temperature of the maximum rate of alcoholamine loss from the alcoholamine-appended framework against the molecular weight of the lost alcoholamine. The maximum rate of alcoholamine loss was determined from the derivative plots of the decomposition profiles. Based on previous results with diamines,[2] we expect that alcoholamines would exhibit *higher loss temperatures with larger N-substitutents* if bound to the framework through the alcohol, similar to the behavior of 1°,2° diamines (circles) which are bound through the primary amine. On the other hand, based on previous results with diamines[2] we would expect that alcoholamines would exhibit *lower loss temperatures with larger N-substitutents* if bound to the framework through the amine, similar to the behavior of 2°,2°diamines (triangles) which are bound through a secondary amine. From this figure, it is clear that alcoholamine-appended frameworks follow the same trend as 1°,2°-diamines, with higher loss temperatures observed with larger alkyl groups on the amine. This finding is indicative of binding to the framework through the alcohol and is consistent with DFT calculations for substituents larger than ethyl.
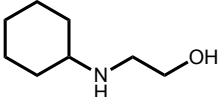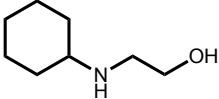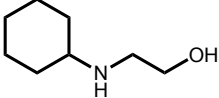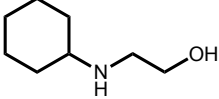
Color Legend:
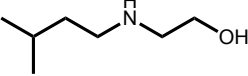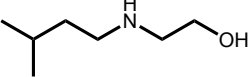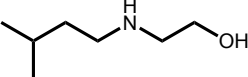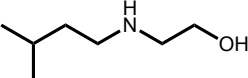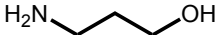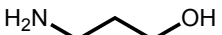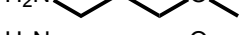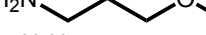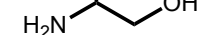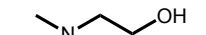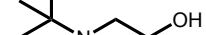
Functional Group	Representation	Functional Group	Representation
Methyl		n-Butyl	
Ethyl		Pentyl	
Propyl		t-Butyl	
Isopropyl			

62

10. Alcoholamine and alkoxyalkylamine loadings from post-synthetic digestion
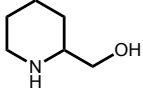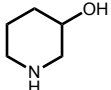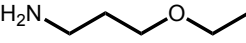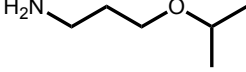
General procedure to determine alcoholamine loadings. Approximately 5 mg of alcoholamine-appended framework was suspended in 1 mL of DMSO-d_6. Two drops of 35% DCl in D_2O were added, and the vial was sealed. The vial was heated gently using a heat gun until the solid fully dissolved. The resulting solution was analyzed by ^{1}H NMR (300 MHz or 400 MHz) to determine the ratio of alcoholamine to ligand.

Table S2. Alcoholamine loadings and activation conditions for M$_2$(dobpdc) variants; 100% loading corresponds to one alcoholamine or alkoxyalkylamine per metal site, and loadings greater than 100% correspond to excess trapped within framework pores. For materials with initial loadings >100%, activation conditions were determined to be adequate if they resulted in loadings >95% and <100% after activation. Materials with initial loadings <100% were similarly determined to be adequate if they resulted in loadings >95% and <100% after activation or did not reduce after activation. Loadings for alcoholamine-appended Mn$_2$(dobpdc) could not be obtained, due to the paramagnetism of Mn^{2+}.
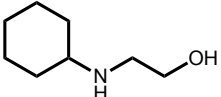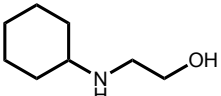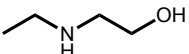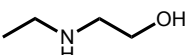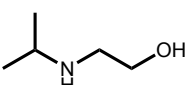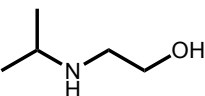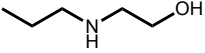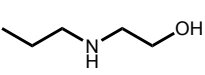
Structure	Shorthand	M^{2+}	Initial Loading	Activation T (ºC)
	e-2-OH	Mg	146%	130
	e-2-OH	Co	151%	100
	e-2-OH	Ni	117%	130
	e-2-OH	Zn	111%	80
	nPr-2-OH	Mg	127%	150
	nPr-2-OH	Co	128%	95
	nPr-2-OH	Ni	109%	150
	nPr-2-OH	Zn	87%	90
	iPr-2-OH	Mg	123%	150
	iPr-2-OH	Co	126%	130
	iPr-2-OH	Ni	75%	150
	iPr-2-OH	Zn	96%	90
	nBu-2-OH	Mg	116%	150
	nBu-2-OH	Co	96%	130
	nBu-2-OH	Ni	101%	110
	nBu-2-OH	Zn	95%	100

Structure	Name	Metal	Value	Temp
(cyclohexyl-NH-CH₂CH₂-OH)	Cy-2-OH	Mg	105%	150
(cyclohexyl-NH-CH₂CH₂-OH)	Cy-2-OH	Co	93%	150
(cyclohexyl-NH-CH₂CH₂-OH)	Cy-2-OH	Ni	93%	125
(cyclohexyl-NH-CH₂CH₂-OH)	Cy-2-OH	Zn	90%	90
(isopentyl-NH-CH₂CH₂-OH)	iPent-2-OH	Mg	110%	150
(isopentyl-NH-CH₂CH₂-OH)	iPent-2-OH	Co	71%	150
(isopentyl-NH-CH₂CH₂-OH)	iPent-2-OH	Ni	95%	110
(isopentyl-NH-CH₂CH₂-OH)	iPent-2-OH	Zn	77%	125
(H_2N-propyl-OH)	3-OH	Mg	80%	150
(H_2N-propyl-OH)	3-OH	Co	112%	100
(H_2N-propyl-OH)	3-OH	Ni	140%	150
(H_2N-propyl-O-m)	3-O-m	Mg	101%	130
(H_2N-propyl-O-m)	3-O-m	Co	140%	100
(H_2N-propyl-O-m)	3-O-m	Ni	125%	100
(H_2N-propyl-O-m)	3-O-m	Zn	125%	90
(H_2N-CH₂CH(OH))	2-OH	Mg	139%	150
(H_2N-CH(CH₂OH))	2a-OH	Mg	135%	125
(m-NH-CH₂CH₂-OH)	m-2-OH	Mg	167%	150
(tBu-NH-CH₂CH₂-OH)	tBu-2-OH	Mg	105%	130
(iPr-NH-propyl-OH)	iPr-3-OH	Mg	90%	150
(mm-N-CH₂CH₂-OH)	mm-2-OH	Mg	99%	130
(iPr,iPr-N-CH₂CH₂-OH)	iPr,iPr-2-OH	Mg	86%	150
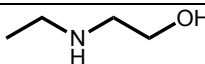
Structure	Shorthand	Framework	Initial Loading	Activation T (°C)
(structure: piperidine-2-methanol)	pip-2-OH	Mg	120%	80
(structure: piperidine-3-ol)	pip-2,OH	Mg	173%	150
(structure: 2-methoxyethylamine)	2-O-m	Mg	101%	100
(structure: 3-ethoxypropylamine)	3-O-e	Mg	111%	125
(structure: 3-isopropoxypropylamine)	3-O-iPr	Mg	101%	130
(structure: 3-amino-1,2-propanediol)	OH-2-OH	Mg	70%	70
(structure: n-butylamine)	nBu	Mg	158%	100

Table S3. Alcoholamine loadings and activation conditions for Mg$_2$(pc-dobpdc) and Mg$_2$(dotpdc). Activation conditions were determined adequate upon achieving >95% loading after activation, provided that the as-synthesized loading was previously >95%.

Structure	Shorthand	Framework	Initial Loading	Activation T (°C)
(structure: N-cyclohexyl ethanolamine)	cy-2-OH	Mg$_2$(dotpdc)	99%	100
(structure: N-cyclohexyl ethanolamine)	cy-2-OH	Mg$_2$(pc-dobpdc)	83%	150
(structure: N-ethyl ethanolamine)	e-2-OH	Mg$_2$(dotpdc)	90%	130
(structure: N-ethyl ethanolamine)	e-2-OH	Mg$_2$(pc-dobpdc)	117%	150
(structure: N-isopropyl ethanolamine)	iPr-2-OH	Mg$_2$(dotpdc)	167%	130
(structure: N-isopropyl ethanolamine)	iPr-2-OH	Mg$_2$(pc-dobpdc)	99%	150
(structure: N-n-propyl ethanolamine)	nPr-2-OH	Mg$_2$(dotpdc)	120%	130
(structure: N-n-propyl ethanolamine)	nPr-2-OH	Mg$_2$(pc-dobpdc)	105%	150

Table S4. Alcoholamine loading and activation temperature for e-2-OH–Mg$_2$(dobpdc) after 40 cycles. The high loading after repeated adsorption and desorption cycles indicates that this material is capable of surviving multiple sequential uses in a practical application.

Structure	Shorthand	Framework	Loading	Activation T (°C)
(structure: N-ethyl ethanolamine)	e-2-OH	Mg$_2$(dobpdc)	97%	130

11. Surface area measurements for alcoholamine-appended Mg₂(dobpdc)
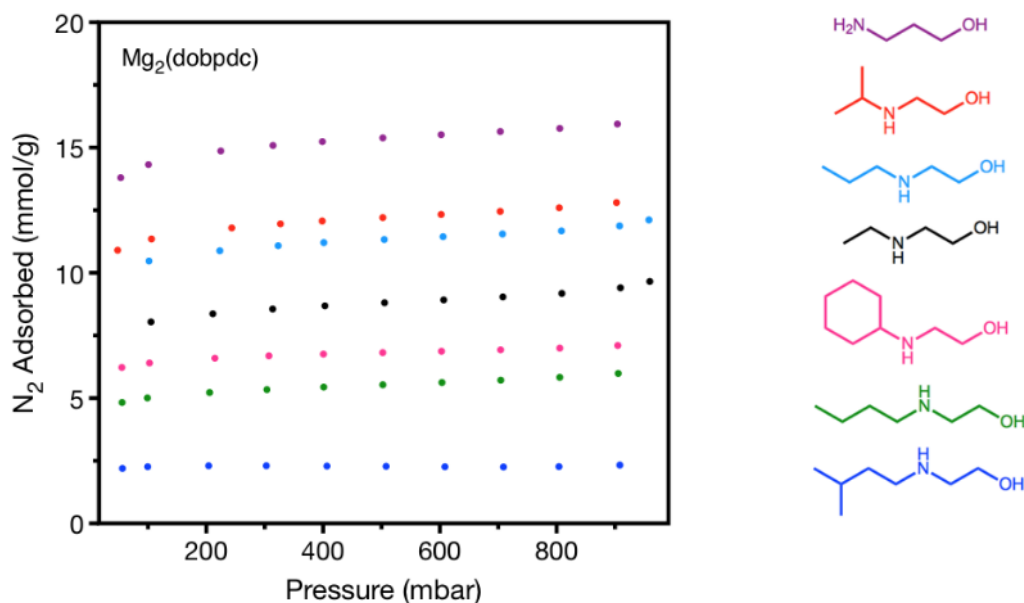
Figure S62. 77 K N_2 isotherms of activated alcoholamine-appended Mg₂(dobpdc). Note that the reproducibly lower-than-expected surface area of e-2-OH-Mg₂(dobpdc) may be due to the disordered nature of the alcoholamines in this framework at 77 K due to the dynamic exchange between the alcohol- and amine-bound structures, as observed at room temperature by solid state NMR.

Table S5. Langmuir surface areas for alcoholamine-appended Mg₂(dobpdc) calculated from the isotherms shown previously.

Structure	Shorthand	Langmuir Surface Area (m²/g)
	3-OH	1857
	iPr-2-OH	1426
	nPr-2-OH	1199
	e-2-OH	961
	nBu-2-OH	773
	cy-2-OH	695
	iPent-2-OH	325

12. Differential scanning calorimetry isobars for e-2-OH–Mg$_2$(dobpdc) and 3-O-m–Mg$_2$(dobpdc)
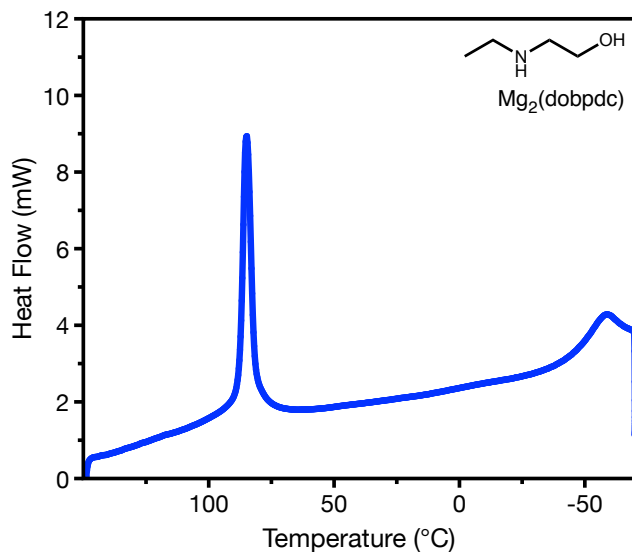
Figure S63. Pure CO$_2$ differential scanning calorimetry isobar of e-2-OH–Mg$_2$(dobpdc). A single exothermic event is seen at the same temperature (80 ºC) as the adsorption step at 1 bar, as measured by thermogravimetric analysis (Figure 2). A second, smaller exotherm is observed below −50 ºC, corresponding to the condensation of CO$_2$.
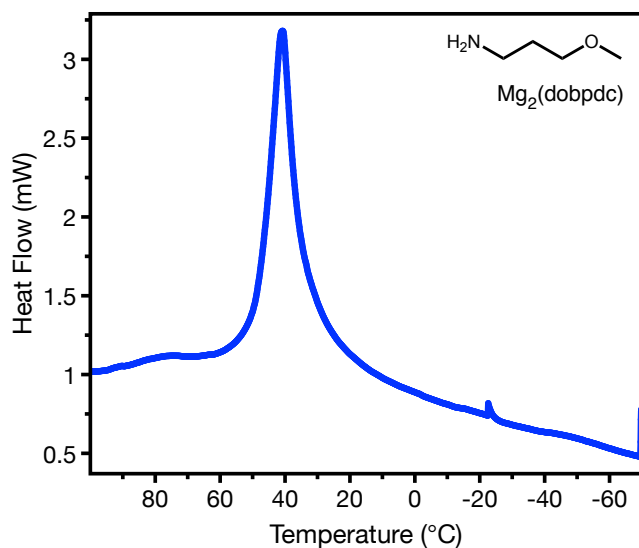
Figure S64. Pure CO$_2$ differential scanning calorimetry isobar of 3-O-m–Mg$_2$(dobpdc). A single exothermic event is seen at the same temperature (50 ºC) as the adsorption step at 1 bar, as measured by thermogravimetric analysis.

13. Powder x-ray diffraction patterns from the Advanced Photon Source

Powder X-ray diffraction data for e-2–Mg_2(dobpdc), e-2-OH–Mg_2(dobpdc), and nPr-2-OH–Mg_2(dobpdc) were collected on Beamline 17-BM-B at the Advanced Photon Source at Argonne National Laboratory. Approximately 3 mg of fully desolvated framework was loaded into a 1.0 mm borosilicate capillary inside a N_2-filled glovebox. Each capillary was then attached to a custom designed gas-dosing cell equipped with a gas valve and transferred to the goniometer head. All adsorbed N_2 was then removed by evacuating *in situ* using a turbomolecular pump. An Oxford Cryosystems Cryostream 800 was used to hold the temperature of the sample at 25 °C. Scattered intensity was measured by a PerkinElmer a-Si flat panel detector.

Diffraction data were collected for the evacuated material, after which approximately 1 bar of CO_2 gas was dosed using a custom-built gas dosing manifold. Each dose of gas was equilibrated on the sample for over half an hour, until no further change was observed in both the pressure above the sample and in the resulting diffraction patterns. The average wavelength of measurement was 0.45212 Å for e-2–Mg_2(dobpdc), and 0.4522 Å for e-2-OH–Mg_2(dobpdc) and nPr-2-OH–Mg_2(dobpdc). Precise unit cell parameters of all samples were obtained by Pawley refinement as implemented in TOPAS-Academic 4.1, and were found to be consistent with a trigonal lattice.[18]
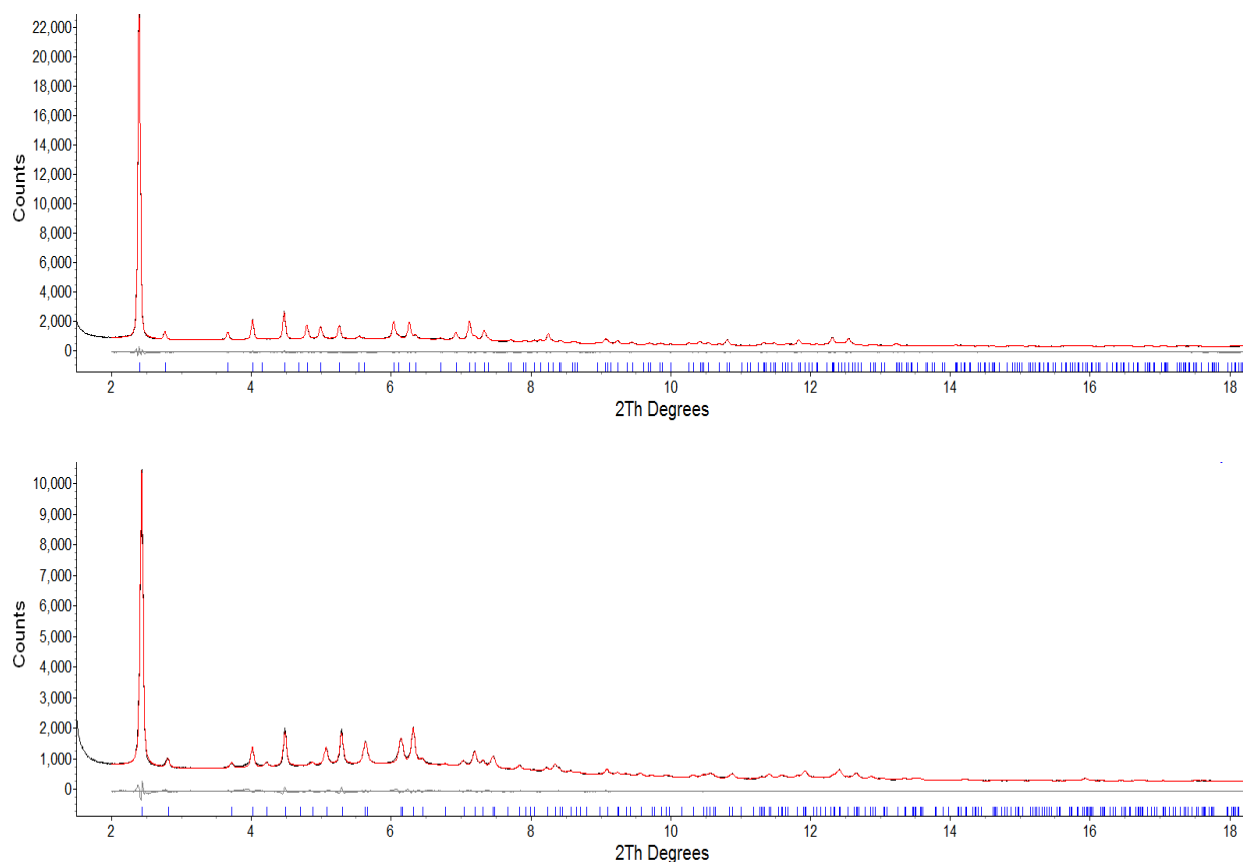
Figure S65. Le Bail Refinement, with errors, of activated (top) and CO_2-inserted (bottom) e-2-OH–Mg_2(dobpdc).
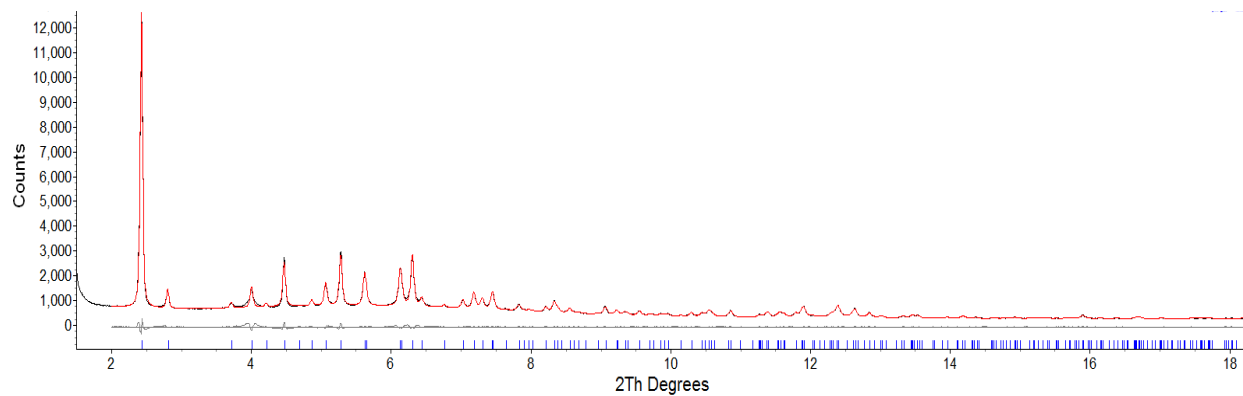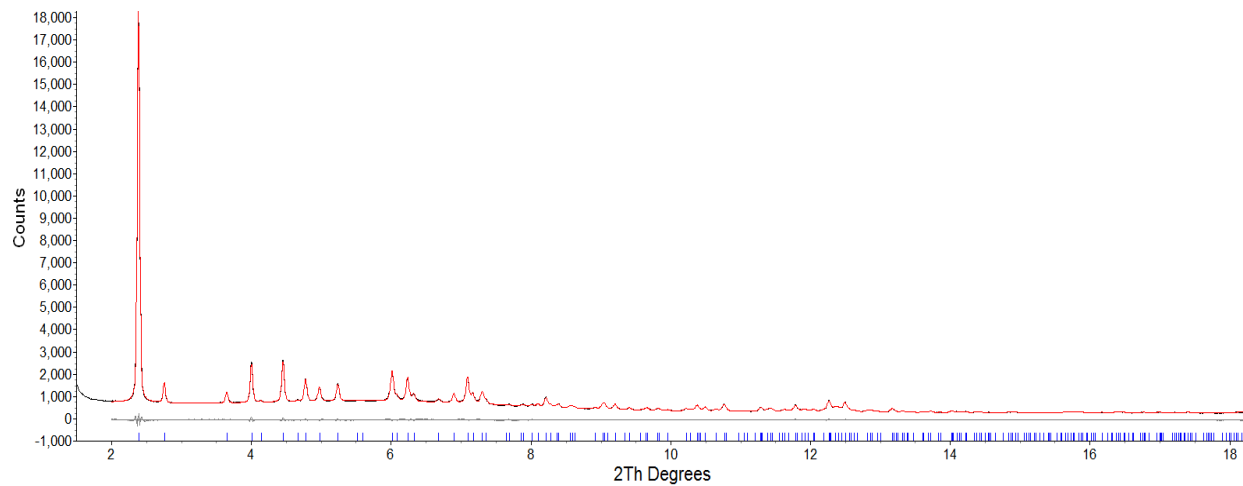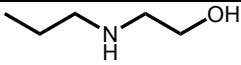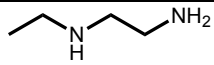
Figure S66. Le Bail Refinement, with errors, of activated (top) and CO_2-inserted (bottom) nPr-2-OH–Mg_2(dobpdc).
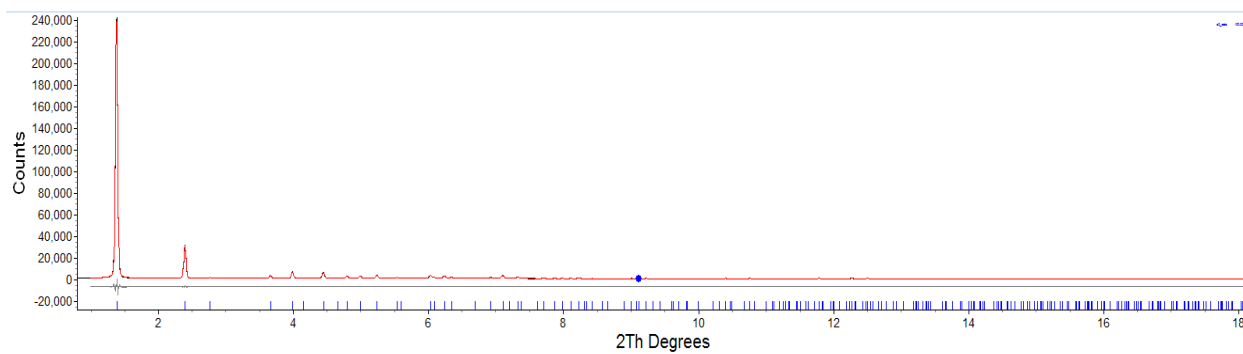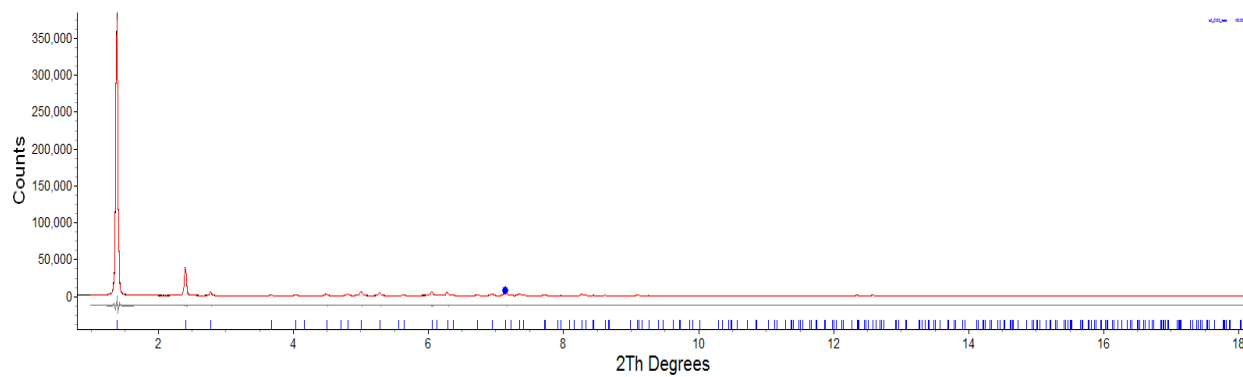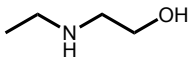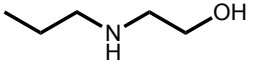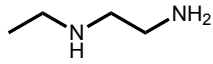
Figure S67. Le Bail Refinement, with errors, of activated (top) and CO_2-inserted (bottom) e-2–Mg_2(dobpdc).
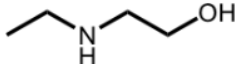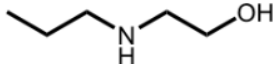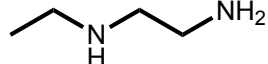
Table S6. Lattice parameters from Le Bail Refinement, with associated errors, of activated e-2-OH–Mg_2(dobpdc), nPr-2-OH–Mg_2(dobpdc), and e-2–Mg_2(dobpdc).

	e-2-OH–Mg_2(dobpdc)	nPr-2–OH Mg_2(dobpdc)	e-2–Mg_2(dobpdc)
Structure			
a	21.594(6)	21.682(7)	21.610(7)
c	6.862(2)	6.889(2)	6.920(2)
V	2771.2(1)	2804.6(7)	2798.9(2)
Space Group	$P3_221$	$P3_221$	$P3_221$

Table S7. Lattice parameters from Le Bail Refinement, with associated errors, of CO_2-inserted e-2-OH–Mg_2(dobpdc), nPr-2-OH–Mg_2(dobpdc), and e-2–Mg_2(dobpdc). When comparing to the previous table of activated parameters, note that a contraction is evident in e-2-OH–Mg_2(dobpdc) and nPr-2-OH–Mg_2(dobpdc), but not in e-2–Mg_2(dobpdc). This is indicative of a significant interaction in the *ab* plane.

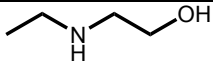|	CO_2–e-2-OH–Mg_2(dobpdc)	CO_2–nPr-2-OH Mg_2(dobpdc)	CO_2–e-2–Mg_2(dobpdc)
Structure			
a	21.255(1)	21.27(1)	21.552(5)
c	6.874(4)	6.898(3)	6.829(3)
V	2689.8(4)	2705.1(3)	2747.4(2)
Space Group	$P3_221$	$P3_221$	$P3_221$

Table S8. Lattice parameters differences for e-2-OH–Mg_2(dobpdc), nPr-2-OH–Mg_2(dobpdc), e-2–Mg_2(dobpdc).

	e-2-OH $Mg2$(dobpdc)	nPr-2-OH $Mg2$(dobpdc)	e-2 $Mg2$(dobpdc)
Structure			
a	−1.5%	−1.9%	−0.3%
c	+0.2%	+0.1%	−1.3%
V	−2.9%	−3.5%	−1.8%
Space Group	$P3_221$	$P3_221$	$P3_221$

14. Humid isobars for alcoholamine-appended Mg₂(dobpdc)
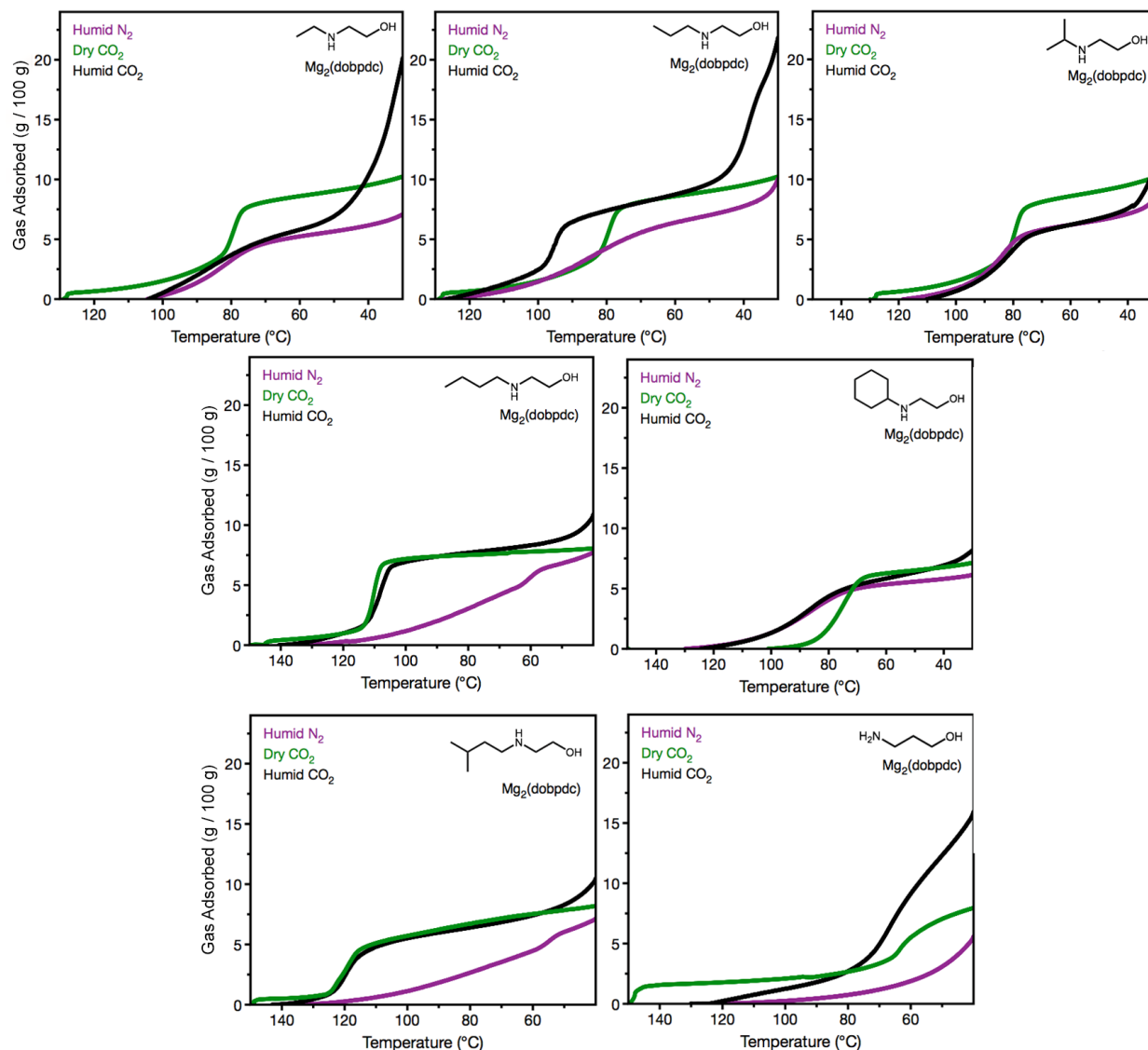
Figure S68. Comparison of humid N$_2$ (purple) and dry (green) and humid (black) CO$_2$ adsorption in e-2-OH–Mg$_2$(dobpdc) (top left), nPr-2-OH–Mg$_2$(dobpdc) (top middle), iPr-2-OH–Mg$_2$(dobpdc) (top right), nBu-2-OH–Mg$_2$(dobpdc) (middle left) cy-2-OH–Mg$_2$(dobpdc) (middle right), iPent-2-OH–Mg$_2$(dobpdc) (bottom left), and 3-OH–Mg$_2$(dobpdc) (bottom right). These results indicate that some of the alcoholamine-appended Mg$_2$(dobpdc) variants likely adsorb CO$_2$ in the presence of water, specifically those for which the purple and black curves do not overlap, including nPr-2-OH–Mg$_2$(dobpdc), nBu-2-OH–Mg$_2$(dobpdc), iPent-2-OH–Mg$_2$(dobpdc), and 3-OH–Mg$_2$(dobpdc).

15. Cycling results for CO₂ adsorption in e-2-OH–Mg₂(dobpdc)
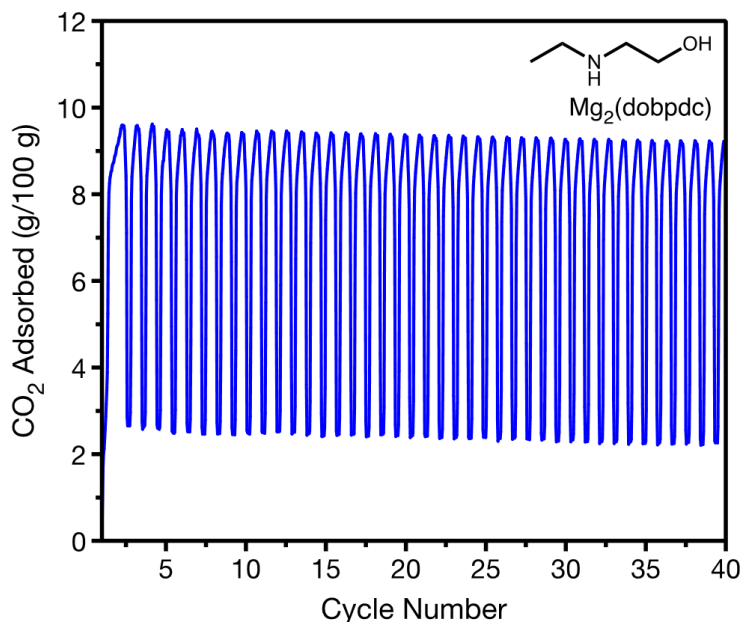
Figure S69. CO_2 adsorption/desorption cycling for e-2-OH–Mg₂(dobpdc). Adsorption: pure CO_2, 40 °C, 5 min (maxima). Desorption: pure CO_2, 90 °C, 5 min (minima). The baseline value of 0 g/100 g is defined to be the mass after activation at 130 °C under pure N_2 for 20 min, prior to the first cycle. The loading was found to be 97% after the cycling experiment. As the adsorption capacity did not change significantly, it is likely that no new adsorption products form during the cycling process.

16. Solid-state nuclear magnetic resonance spectroscopy

Activated samples were packed into 3.2 mm zirconia rotors inside a N_2-filled glove bag. Samples were then transferred to a home-built gas-dosing manifold, and were evacuated for 10 min. The manifold enables samples in rotors to be dosed with gases at controlled pressures. Samples were dosed with $^{13}CO_2$ (Sigma-Aldrich, 99 atom % ^{13}C, < 3 atom % ^{18}O) for 30 min and sealed inside the manifold. Gas-dosing pressures are indicated in the figures or captions, and gas-dosing was performed at room temperature (22(1) °C). NMR experiments were then performed at 16.4 T and with a magic angle spinning (MAS) rate of 15 kHz, except where otherwise indicated. ^{13}C and ^{15}N NMR spectra were obtained by cross-polarization from ^{1}H with a contact time of 1 ms, and continuous wave decoupling was used during signal acquisition. For two-dimensional (^{1}H, ^{13}C) experiments, a HETCOR experiment employing cross-polarization from ^{1}H to ^{13}C was used according to: $90°(^{1}H) - t_1 -$ cross-polarization $- t_2$, with continuous wave ^{1}H decoupling. In these HETCOR experiments, a relatively short contact time of 100 μs was used for cross-polarization, such that only the ^{1}H spins most proximate to the chemisorbed ^{13}C spin are observed. ^{1}H, ^{13}C, and ^{15}N, chemical shifts were referenced to 1.8 ppm (adamantane), 38.5 ppm (adamantane, tertiary carbon – left hand resonance), and 33.4 ppm (glycine),[4] respectively.
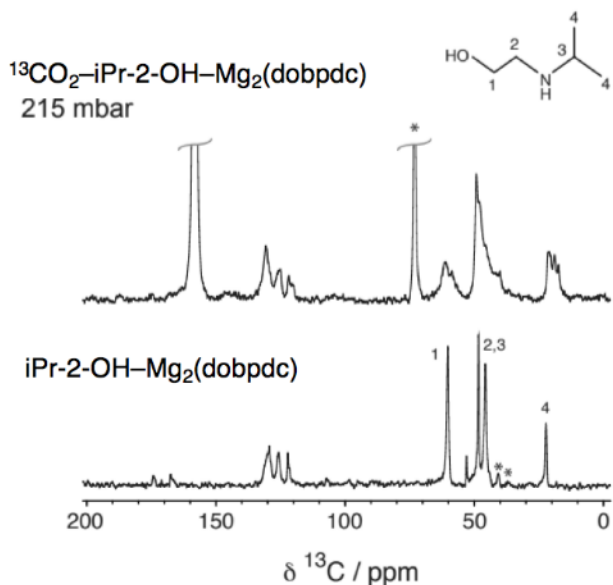
Figure S70. [13]C cross polarization (contact time 1 ms) NMR spectra of iPr-2-OH–Mg$_2$(dobpdc) dosed with [13]CO$_2$. Alkyl splittings are apparent, indicating a potentially similar mechanism of chemisorption as e-2-OH–Mg$_2$(dobpdc). The carbonyl carbon resonance is also apparent at a similar chemical shift compared to that of e-2-OH–Mg$_2$(dobpdc).
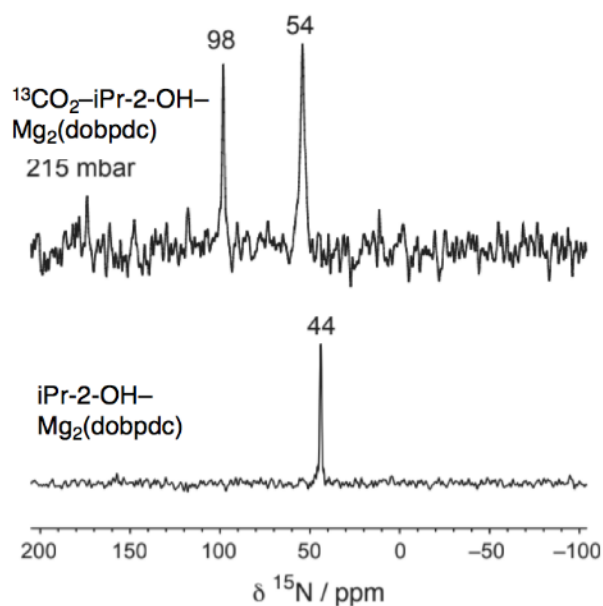
Figure S71. [15]N cross polarization (contact time 1 ms) NMR spectra of iPr-2-OH–Mg$_2$(dobpdc) dosed with [13]CO$_2$. Due to the similarity of chemical shifts as those of e-2-OH–Mg$_2$(dobpdc), the chemical shifts at 98 and 54 ppm are assigned to the inserted and free amine, respectively, according to a similar mechanism as that of e-2-OH–Mg$_2$(dobpdc).
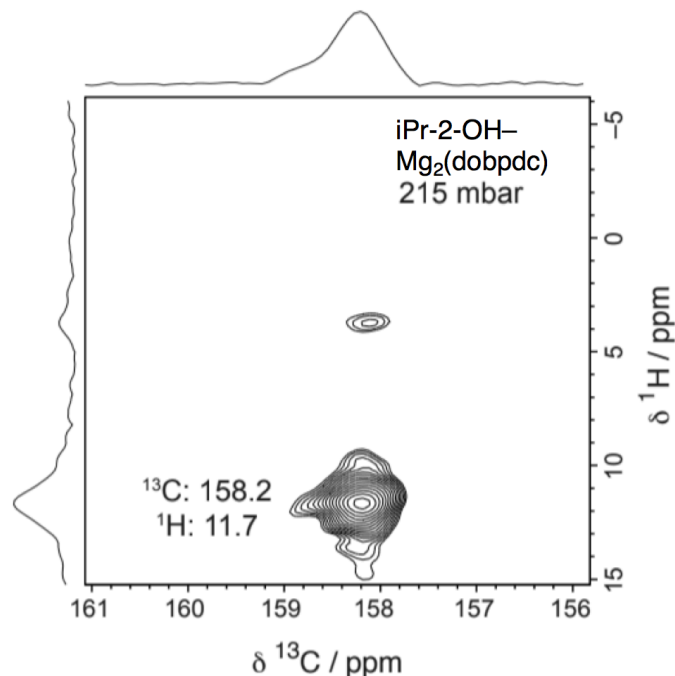
Figure S72. ^{13}C–^1H HETCOR (contact time 100 µs) NMR spectrum for $^{13}CO_2$-dosed iPr-2-OH–Mg_2(dobpdc). Similar to that of e-2-OH–Mg_2(dobpdc), a single dominant correlation is observed at a ^1H shift of 11.7 ppm and a ^{13}C shift of 158.2, assigned to a carbamic acid COOH group.

17. Density functional theory methods and results

Our first-principles density functional theory (DFT) calculations used a plane-wave basis and projector augmented-wave (PAW)[6,7] pseudopotentials as implemented in the Vienna ab-initio Simulation Package (VASP) code.[8-11] To include important effects of van der Waals (vdW) dispersive interactions on binding energies and mechanical properties, we performed structural relaxations with vdW dispersion-corrected functionals (vdW-DF2)[12] as implemented in VASP. For all calculations, we used (i) a Γ-point sampling of the Brillouin zone and (ii) a 600 eV plane-wave cutoff energy. In our PAW pseudopotentials, we explicitly treated two valence electrons for Mg ($3s^2$), six for O ($2s^22p^4$), five for N ($2s^22p^3$), four for C ($2s^22p^2$), and one for H ($1s^1$). All structural relaxations were performed with a Gaussian smearing of 0.05 eV.[13] The ions were relaxed until the Hellmann-Feynman forces were less than 0.02 eVÅ^{-1}.

To compute CO_2 binding energies, we optimized e-2-OH–Mg_2(dobpdc) prior to CO_2 adsorption ($E_{e2OH-MOF}$), interacting with CO_2 in the gas phase (E_{CO2}) within a 15×15×15 Å cubic supercell, and e-2-OH–Mg_2(dobpdc) with adsorbed CO_2 molecule ($E_{CO_2-e2OH-MOF}$) using vdW-corrected DFT. The binding energies (E_B) were obtained via the difference:

$$E_B = E_{CO_2-e2OH-MOF} - \left(E_{e2OH-MOF} + E_{CO_2}\right).$$

Here, we neglected zero-point and thermal vibrational corrections to the CO_2 binding energies, which is sufficient for this study as these values are typically on the order of a few kJ/mol.[23-27]

For NMR simulations, we performed structural relaxations with (i) a 1000 eV plane-wave cutoff energy, (ii) a 0.01 eVÅ^{-1} force criterion, (iii) a 1×1×3 k-point, (iv) a 10^{-7} eV self-consistency criterion, and (v) D3 vdW correction.[14,15] Using these criteria, we fully relaxed both the unit cell and all internal

coordinates. Given the number of structures considered here, we use PBE+D3 instead of vdW-DF2 for our shielding tensor calculations; PBE+D3 leads to very similar structural parameters and better chemical shifts (see Table S10) but is significantly more efficient than vdW-DF2 for computing shielding tensors. The structural differences are <1%. With these criteria, the isotropic chemical shielding tensors (σiso) converged to 0.1 ppm.

Since the isotropic chemical shift (δ_{iso}) is obtained from $\delta_{iso} = -(\sigma_{iso} - \sigma_{ref})$ where σ_{ref} is a reference value, we needed to determine a σ_{ref} value by comparing experimental δ_{iso} values to calculated σ_{iso} values. For ^{13}C, the y-intercept (σ_{ref}) of a plot of the experimental δ_{iso} versus the calculated σ_{iso} for activated dmpn-Zn_2(dobpdc) was 169.8 ppm, a value in good agreement with the previous NMR calculation.[12] For ^{15}N, the σ_{ref} was 225.0 ppm.

Table S9. O vs. N binding mode DFT-calculated energies for activated alcoholamine-appended Mg_2(dobpdc). It is evident that larger amine substituents exhibit greater preference for binding through oxygen.

Alcoholamine	$E_{O\text{-bound}}$ (eV)	$E_{N\text{-bound}}$ (eV)	$E_{O\text{-bound}} - E_{N\text{-bound}}$ (kJ/mol)
m-2-OH	−904.727	−903.800	−14.9
e-2-OH	−995.484	−995.500	1.5
_n_Pr-OH	−1086.908	−1086.650	−4.1
_i_Pr-2-OH	−1086.935	−1085.304	−26.2
_t_Bu-2-OH	−1178.485	−1176.394	−33.6

Table S10. Optimized structural parameters and chemical shifts of Mechanism A of CO_2 insertion in e-2-OH–Mg_2(dobpdc) for PBE+D3 and vdW-DF2 compared to the experiment.

Structural and Chemical Parameters (Å)	PBE+D3	vdW-DF2	Experiment
_a_	21.160	21.299	21.255
_c_	7.055	7.053	6.875
C=O	1.259	1.261	–
C–OH	1.334	1.359	–
C–N	1.352	1.356	
[13]C on C=O	158.5	160.8	158.5
[15]N on inserted N	102.4	109.6	90.0
[15]N on free N	38.7	46.2	41.0

18. 3-O-m–Mg₂(dobpdc) CO₂ adsorption NMR data

Table S11. Computed chemical shifts (ppm) associated with mechanism **A'**, CO_2 insertion in 3-O-m–Mg₂(dobpdc). Measurement uncertainties are indicated in parentheses.
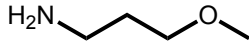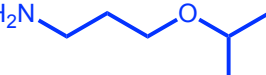
	Experiment	**Theory**
$\delta\ ^{13}\text{C (C=O)}$	163.6(1)	164.6
	2.3(1) (methyl ether)	3.3 (methyl ether)
$\delta\ ^1\text{H}$	4.6(1) (inserted N)	5.1 (inserted N)
	8.7(1) (ammonium)	8.8 (ammonium)

19. Surface area measurements of 3-O-m–Mg₂(dobpdc), 3-O-e–Mg₂(dobpdc), and 3-O-iPr–Mg₂(dobpdc)
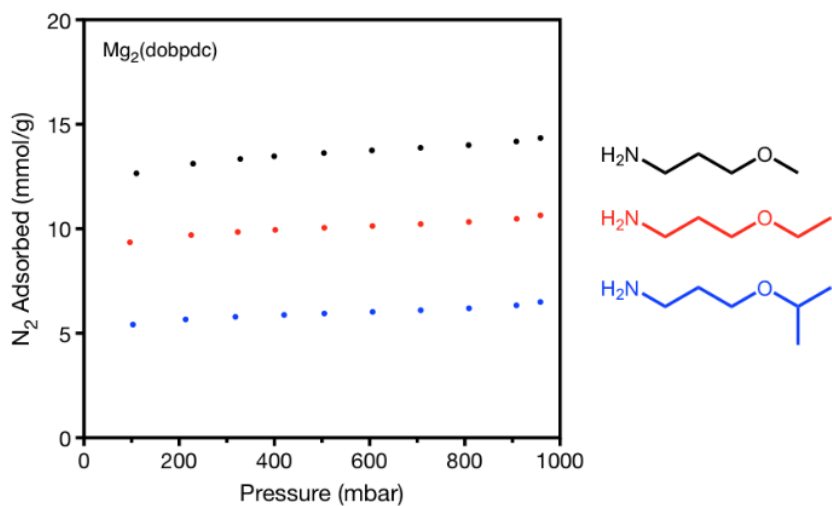
Figure S73. 77 K N_2 isotherms of 3-O-m–Mg_2(dobpdc) (black), 3-O-e–Mg_2(dobpdc) (red), and 3-O-iPr–Mg_2(dobpdc) (blue).

Table S12. Langmuir surface area values of 3-O-m–Mg_2(dobpdc) (black), 3-O-e–Mg_2(dobpdc) (red), and 3-O-iPr–Mg_2(dobpdc) (blue). Langmuir surface areas were calculated from the isotherms shown previously.

Structure	Shorthand	Langmuir Surface Area (m^2/g)
H_2N ⌇ O ⌇	3-O-m	1429
H_2N ⌇ O ⌇	3-O-e	1054
H_2N ⌇ O ⌇	3-O-iPr	649

20. CO_2 isotherm data for 3-O-m–Mg_2(dobpdc), 3-O-e–Mg_2(dobpdc), and 3-O-iPr-OH–Mg_2(dobpdc)
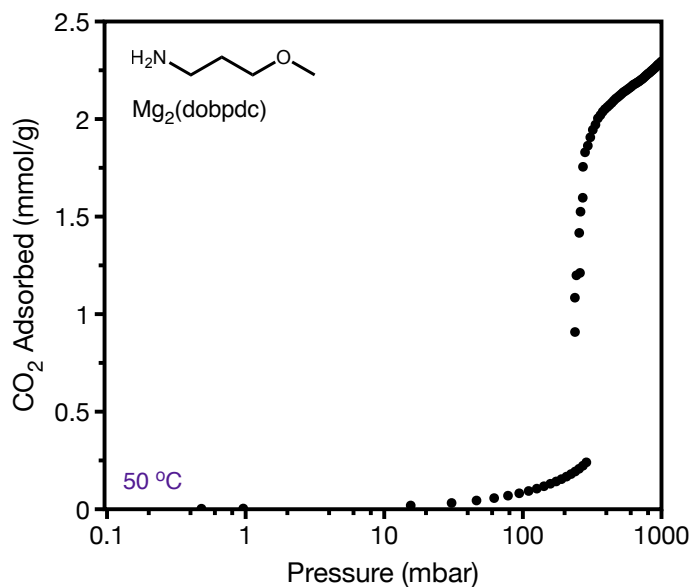
Figure S74. CO_2 adsorption isotherm (50 °C) for 3-O-m–Mg_2(dobpdc). The sample was activated under flowing N_2 at the previously described temperatures for 0.5 h, followed by activation under high vacuum (<10 µbar) at 110 °C for 4 h prior to start.
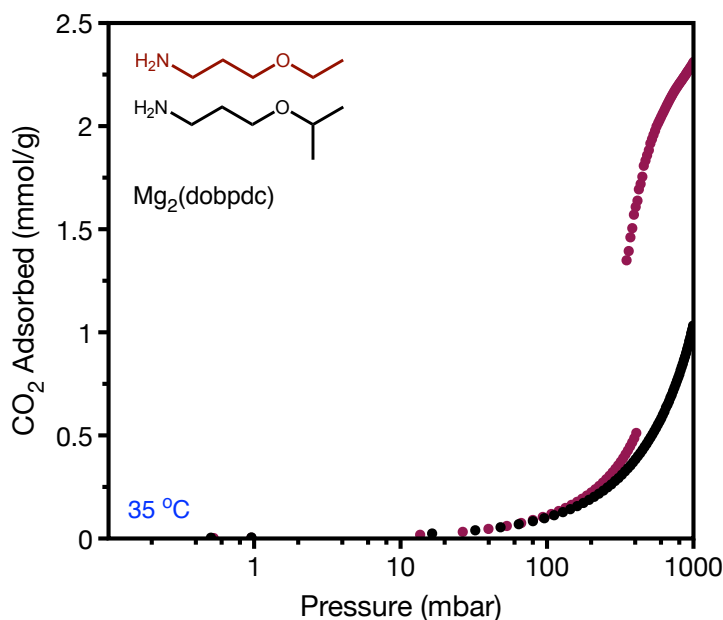
Figure S75. CO_2 adsorption isotherms (30 °C) for 3-O-e–Mg_2(dobpdc) and 3-O-iPr–Mg_2(dobpdc). The samples were activated under flowing N_2 at the previously described temperatures for 0.5 h, followed by activation under high vacuum (<10 µbar) at 110 °C for 4 h prior to start.

21. Variable temperature CO_2 adsorption data for e-2-OH–Mg_2(dobpdc)
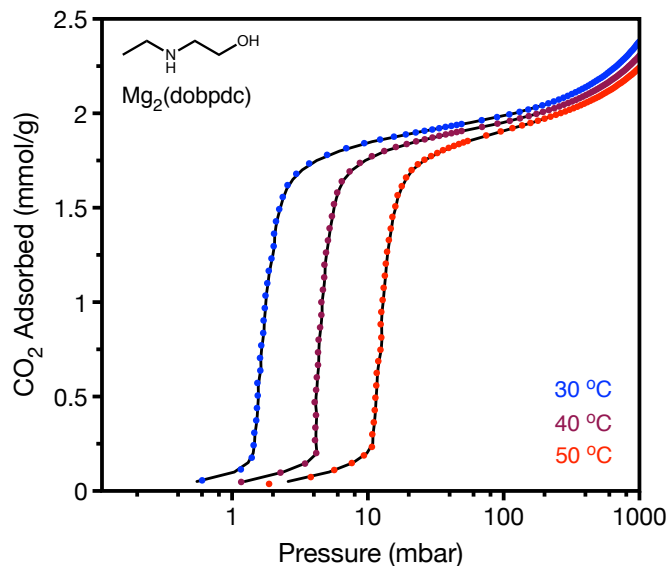
Figure S76. Pure CO_2 isotherms of e-2-OH–Mg_2(dobpdc) collected at 30, 40, and 50 °C. Fits (black lines) were determined by linear interpolation. The sample was activated under flowing N_2 at 150 °C for 0.5 h, followed by activation under high vacuum (<10 µbar) at 110 °C for 4 h. The sample was reactivated under high vacuum (<10 µbar) at 100 °C for 2–4 h between isotherms.
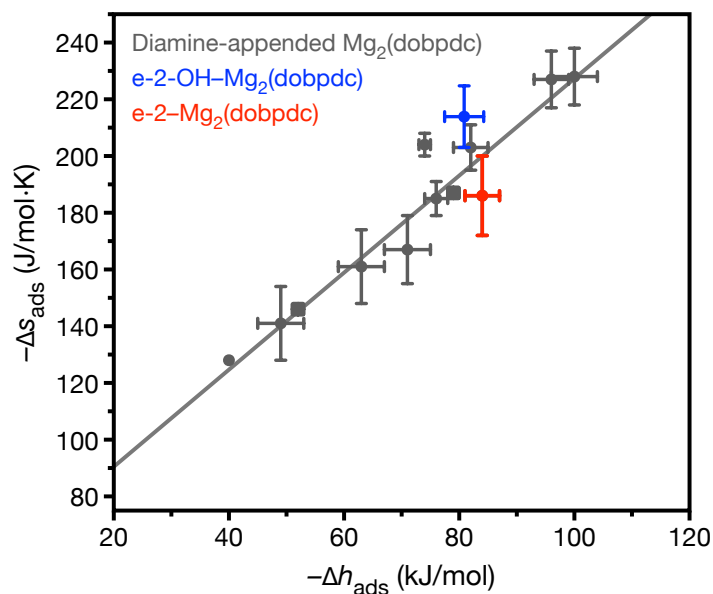
Figure S77. $-\Delta s_{ads}$ vs. $-\Delta h_{ads}$ thermodynamic plot diagramming values comparing various[2] diamine-appended Mg_2(dobpdc), e-2-OH–Mg_2(dobpdc) (blue), and e-2–Mg_2(dobpdc) (red). All $-\Delta h_{ads}$ and $-\Delta s_{ads}$ values are taken from Clausius-Clapeyron derived differential plots (see below) at a loading of 1 mmol/g.
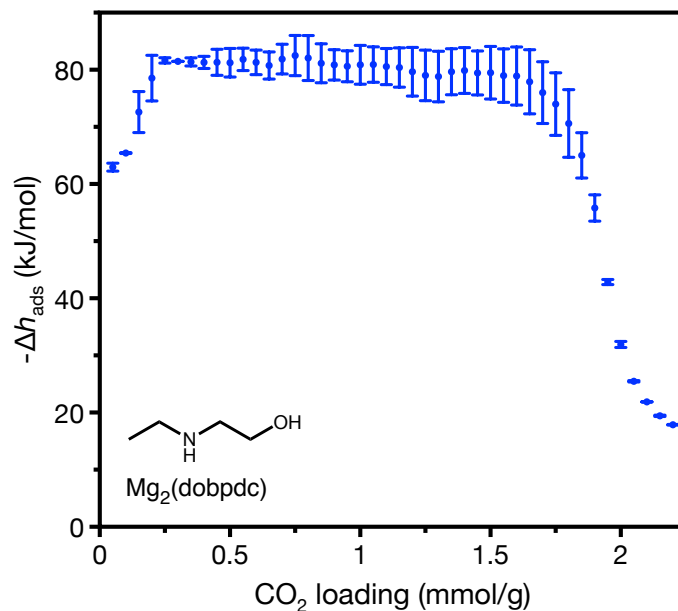
Figure S78. CO_2 differential heats of adsorption for e-2-OH–Mg_2(dobpdc), determined using the Clausius–Clapeyron equation and the fits shown in Figure S76. The value of $-\Delta h_{ads}$ for cooperative binding is 81 kJ/mol, as determined at a loading of 1 mmol/g.
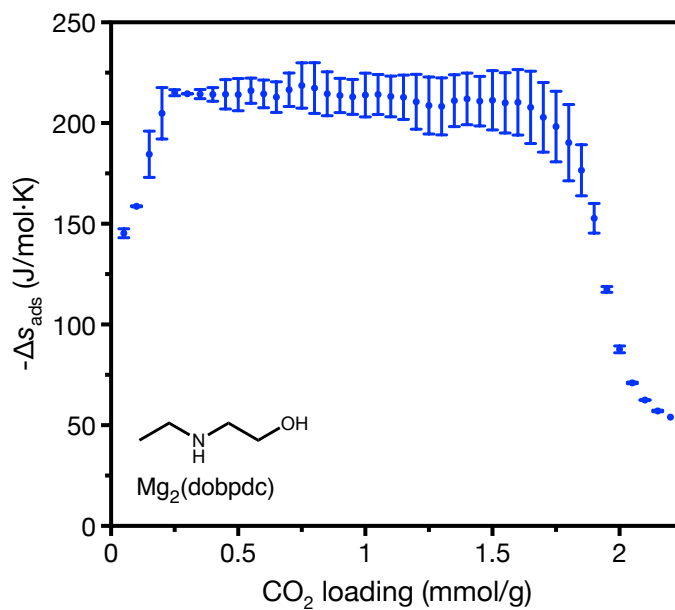
Figure S79. CO_2 differential entropies of adsorption for e-2-OH–Mg_2(dobpdc) determined from the y-intercepts of the linear fits of $\ln(p)$ vs $1/T$ at constant loadings using the fits shown in Figure S76. The value of $-\Delta s_{ads}$ for cooperative binding is 214 J/mol K, as determined from a loading of 1 mmol/g.

81

22. High pressure CO₂ adsorption data for e-2-OH–Mg₂(dobpdc)

Figure S80. High pressure CO_2 isotherms for e-2-OH–Mg₂(dobpdc). Closed circles indicate adsorption and open circles indicate desorption. The lack of step-shaped adsorption to 4 mmol/g (corresponding to 1 CO_2 per 1 alcoholamine) and the presence of physisorption-shaped behavior at higher pressures indicates that *ab* interactions cannot be overcome by increasing the driving force for adsorption.

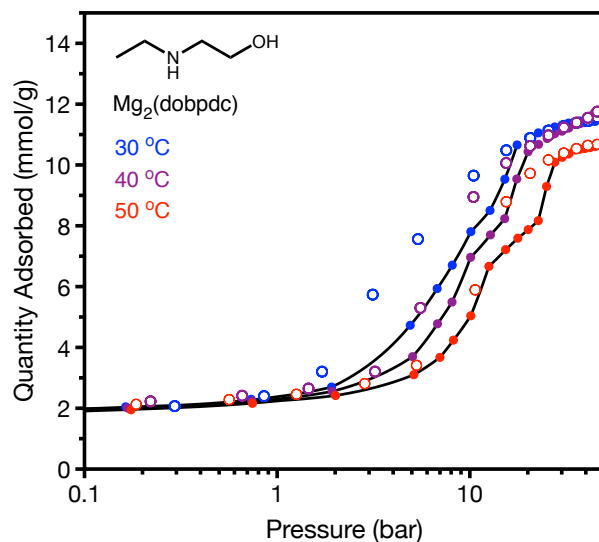**Figure S81.** High pressure CO_2 differential heats of adsorption for e-2-OH–Mg₂(dobpdc), determined using the Clausius–Clapeyron equation and the fits shown in Figure S80, as a function of the amount of CO_2 adsorbed per alcoholamine. The low adsorption enthalpy levels after 0.5 CO_2 adsorbed per alcoholamine are indicative of physisorption, not chemisorption.[2]
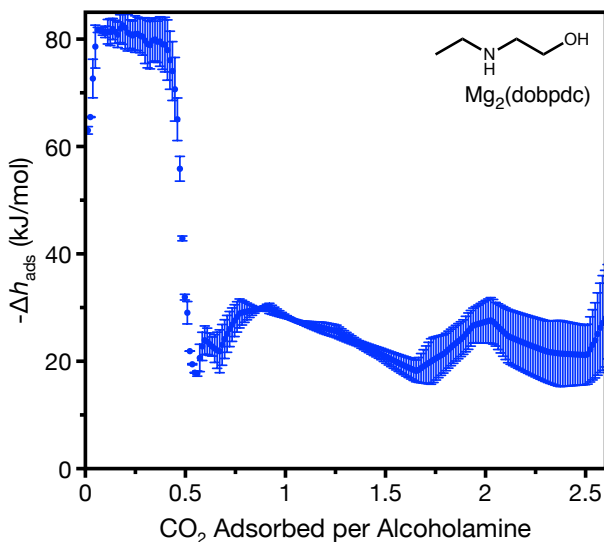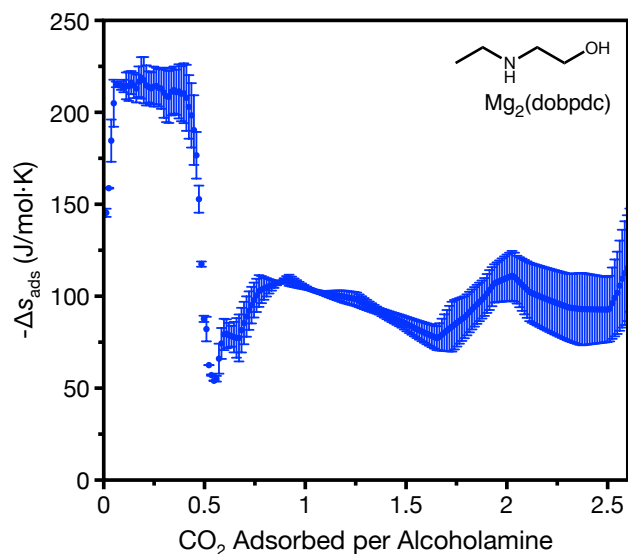
Figure S82. High pressure CO_2 differential entropies of adsorption for e-2-OH–Mg_2(dobpdc) determined from the *y*-intercepts of the linear fits of $\ln(p)$ vs $1/T$ at constant loadings using the fits shown in Figure S82. The low adsorption entropy levels after 0.5 CO_2 adsorbed per alcoholamine are indicative of physisorption, not chemisorption.[2]

23. Full isobar data for cooperative alcoholamine and alkoxyalkylamine-appended Mg₂(dobpdc) variants
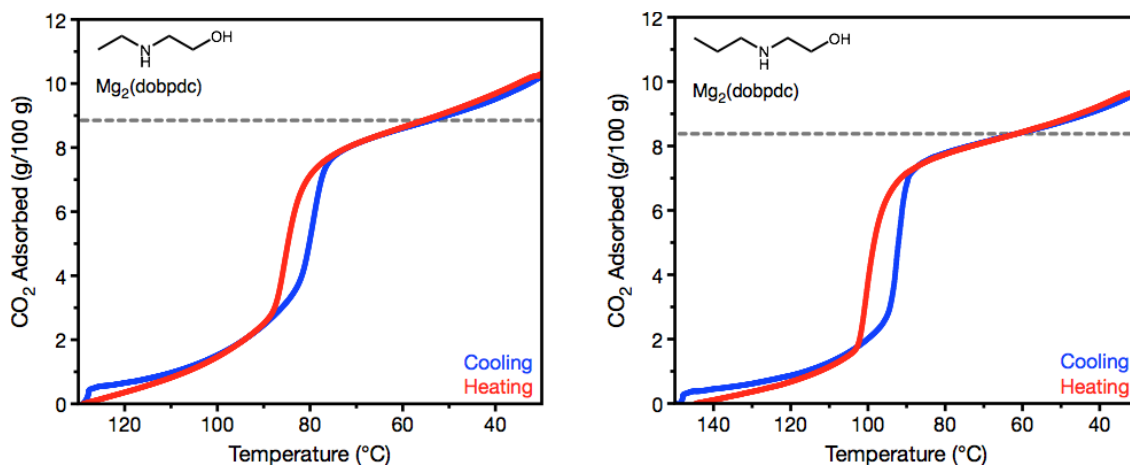
Figure S83. Pure CO_2 adsorption (blue) and desorption (red) isobars for e-2-OH–Mg_2(dobpdc) (left) and nPr-2-OH–Mg_2(dobpdc) (right). The dashed grey line indicates a theoretical loading of 1 CO_2 per 2 alcoholamines.
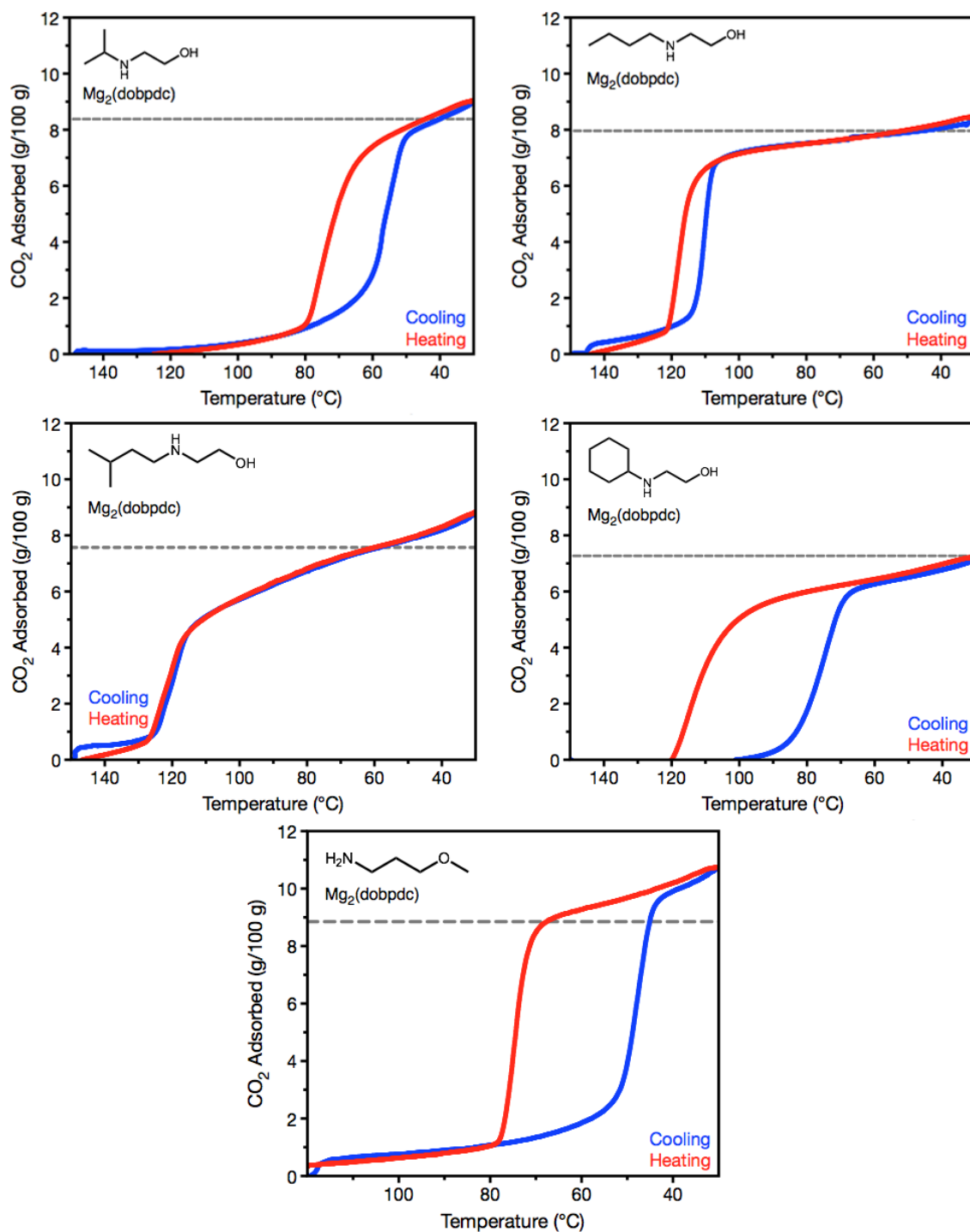
Figure S84. Pure CO_2 adsorption (blue) and desorption (red) isobars for iPr-2-OH–Mg_2(dobpdc) (top left), and nBu-2-OH–Mg_2(dobpdc) (top right), iPent-2-OH–Mg_2(dobpdc) (middle left), cy-2-OH–Mg_2(dobpdc) (middle right), and 3-O-m–Mg_2(dobpdc) (bottom). The dashed grey line indicates a theoretical loading of 1 CO_2 per 2 alcoholamines.

24. References

[1] T. M. McDonald, J. A. Mason, X. Kong, E. D. Bloch, D. Gygi, A. Dani, V. Crocellà, F. Giordanino, S. O. Odoh, W. S. Drisdell, B. Vlaisavljevich, A. L. Dzubak, R. Poloni, S. K. Schnell, N. Planas, K. Lee, T. Pascal, L. F. Wan, D. Prendergast, J. B. Neaton, B. Smit, J. B. Kortright, L. Gagliardi, S. Bordiga, J. A. Reimer, J. R. Long, *Nature* **2015**, *519*, 303.

[2] R. L. Siegelman, T. M. McDonald, M. I. C. Gonzalez, J. D. Martell, P. J. Milner, J. A. Mason, A. H. Berger, A. S. Bhown, J. R. Long, *J. Am. Chem. Soc*. **2017**, *139*, 10526.

[3] P. J. Milner, R. L. Siegelman, A. C. Forse, M. I. Gonzalez, T. Runčevski, J. D. Martell, J. A. Reimer, J. R. Long, *J. Am. Chem. Soc*. **2017**, *139*, 13541−13553.

[4] P. Bertani, J. Raya, B. Bechinger, *Solid State Nucl. Mag.* **2014**, 61−62, 15−18.

[5] J. P. Perdew, K. Burke, M. Ernzerhof, *Phys. Rev. Lett*. **1996**, *77*, 3865.

[6] P. E. Blochl, *Phys. Rev. B* **1994**, *50*, 17953.

[7] G. Kresse, D. Joubert, *Phys. Rev. B* **1999**, *59*, 1758.

[8] G. Kresse, J. Hafner, *Phys. Rev. B* **1993**, *47*, 558.

[9] G. Kresse, J. Furthmuller, *Phys. Rev. B* **1996**, *54*, 11169.

[10] G. Kresse, J. Furthmuller, *Comput. Mater. Sci.* **1996**, *6*, 15.

[11] G. Kresse, J. Hafner, *Phys. Rev. B* **1994**, *49*, 14251.

[12] K. Lee, E. D. Murray, L. Kong, B. I. Lundqvist, D. C. Langreth, *Phys. Rev. B* **2010**, *82*, 081101.

[13] C. Elsasser, M. Fahnle, C. T. Chan, K. M. Ho, *Phys. Rev. B* **1994**, *49*, 13975.

[14] S. Grimme, J. Antony, S. Ehrlich, H. J. Krieg, *J. Chem. Phys.* **2010**, *132*, 154104.

[15] S. Grimme, S. Ehrlich, L. J. Goerigk, *Comput. Chem.* **2011**, *32*, 1456.

[16] P. J. Milner, J. D. Martell, R. L. Siegelman, D. Gygi, S. C. Weston, J. R. Long, *Chem. Sci.* **2018**, *9*, 160.

[17] J. A. Mason, J. Oktawiec, M. K. Taylor, M. R. Hudson, J. Rodriguez, J. E. Bachman, M. I. Gonzalez, A. Cervellino, A. Guagliardi, C. M. Brown, P. L. Llewellyn, N. Masciocchi, J. R. Long, *Nature* **2015**, *527*, 357–361.

[18] A. A. Coelho, TOPAS-Academic, version 4.1 (Coelho Software, 2007).

[19] B. Lv, B. Guo, Z. Zhou, G. Jing, *Environ. Sci. Technol.* **2015**, 49 (17), 10728–10735.

[20] N. Planas, A. L. Dzubak, R. Poloni, L. Lin, A. McManus, T. M. McDonalds, J. B. Neaton, J. R. Long, B. Smit, L. Gagliardi, *J. Am. Chem. Soc*. **2013**, *135* (20), 7402–740.

[21] A. C. Forse, P. J. Milner, J. Lee, H. N. Redfearn, J. Oktawiec, R. L. Siegelman, J. D. Martell, B. Dinakar, L. B. Porter-Zasada, M. I. Gonzalez, J. B. Neaton, J. R. Long, J. A. Reimer. *J. Am. Chem. Soc*. **2018**, *140* (51), 18016–18031.

[22] J. A. Mason, M. Veenstra, J. R. Long. *Chem. Sci.* **2014**, *5* (1), 32–51.

[23] E. W. Lemmon, M. L. Huber, M. O. McLinden. *REFPROP: Reference Fluid Thermodynamic and Transport Properties, Version 9*; National Institute of Standards and Technology, 2010.

[24] K. Lee, J. D. Howe, L.-C. Lin, B. Smit, J. B. Neaton. *Chem. Mater.* **2015**, *27*, 668.

[25] B. Vlaisavlievich, S. O. Odoh, S. K. Schnell, A. L. Dzubak, K. Lee, N. Planas, J. B. Neaton, L. Gagliardi, B. Smit. *Chem. Sci.* **2015**, *6*, 5177.

[26] B. Vlaisavljevich, J. Huck, Z. Hulvey, K. Lee, J. A. Mason, J. B. Neaton, J. R. Long, C. M. Brown, D. Alfè, A. Michaelides, B. Smit. *J. Phys. Chem. A* **2017**, *121* (21), 4139.

[27] J.-H. Lee, R. L. Siegelman, L. Maserati, T. Rangel, B. A. Helms, J. R. Long, J. B. Neaton. *Chem. Sci.* **2018**, *2*, 5197.